FY19-FY21 Concentrating Solar Power Systems Analysis Final Report

Chad Augustine, Parthiv Kurup, Mark Mehos, and Ty Neises

National Renewable Energy Laboratory

NREL is a national laboratory of the U.S. Department of Energy
Office of Energy Efficiency & Renewable Energy
Operated by the Alliance for Sustainable Energy, LLC

This report is available at no cost from the National Renewable Energy Laboratory (NREL) at www.nrel.gov/publications.

Contract No. DE-AC36-08GO28308

Technical Report
NREL/TP-5700-82529
January 2023

FY19-FY21 Concentrating Solar Power Systems Analysis Final Report

Chad Augustine, Parthiv Kurup, Mark Mehos, and Ty Neises

National Renewable Energy Laboratory

Suggested Citation
Chad Augustine, Parthiv Kurup, Mark Mehos, and Ty Neises. 2023. *FY19-FY21 Concentrating Solar Power Systems Analysis Final Report*. Golden, CO: National Renewable Energy Laboratory. NREL/TP-5700-82529. https://www.nrel.gov/docs/fy23osti/82529.pdf.

NREL is a national laboratory of the U.S. Department of Energy
Office of Energy Efficiency & Renewable Energy
Operated by the Alliance for Sustainable Energy, LLC

This report is available at no cost from the National Renewable Energy Laboratory (NREL) at www.nrel.gov/publications.

Contract No. DE-AC36-08GO28308

Technical Report
NREL/TP-5700-82529
January 2023

National Renewable Energy Laboratory
15013 Denver West Parkway
Golden, CO 80401
303-275-3000 • www.nrel.gov

NOTICE

This work was authored by the National Renewable Energy Laboratory, operated by Alliance for Sustainable Energy, LLC, for the U.S. Department of Energy (DOE) under Contract No. DE-AC36-08GO28308. Funding provided by the U.S. Department of Energy Office of Energy Efficiency and Renewable Energy Solar Energy Technologies Office. The views expressed herein do not necessarily represent the views of the DOE or the U.S. Government.

Cover Photos by Dennis Schroeder: (clockwise, left to right) NREL 51934, NREL 45897, NREL 42160, NREL 45891, NREL 48097, NREL 46526.

Acknowledgments

The authors would like to thank the U.S. Department of Energy Office of Energy Efficiency and Renewable Energy Solar Energy Technologies Office for sponsoring this work and for providing guidance and feedback. We also would like to thank Andru Prescod of the U.S. Department of Energy and Craig Turchi of the National Renewable Energy Laboratory for reviewing the work prior to publishing.

List of Acronyms

ATB	Annual Technology Baseline
BOM	bill of materials
CAPEX	capital expenditure
CAD	computer aided design
CSP	concentrating solar power
DFA	Design for Assembly
DFM	Design for Manufacture
DFMA	Design for Manufacturing and Assembly
DLR	German Aerospace Center
DNI	direct normal irradiance
DOE	U.S. Department of Energy
EPC	engineering procurement contractor
HOPP	
HTF	heat transfer fluid
IPH	industrial process heat
ITC	Investment Tax Credit
KSA	Kingdom of Saudi Arabia
LCOE	levelized cost of electricity
LMTD	log mean temperature difference
MSPT	molten salt power tower
MT	mid-term
NT	near-term
NPV	net present value
NREL	National Renewable Energy Laboratory
PCM	phase change material
PHX	primary heat exchanger
PPA	power purchase agreement
PTC	parabolic trough collector
PV	photovoltaic
ROP	Ring of Power
SD	Solar Dynamics
SCA	solar collector assembly
SCE	solar collector element
sbp	Schlaich Bergermann und Partner
SunBeam-MT	SunBeam Mid-Term
SunBeam-NT	SunBeam Near-Term
SAM	System Advisor Model
sCO_2	supercritical carbon dioxide
SETO	Solar Energy Technologies Office
SolarTAC	Solar Technology Acceleration Center
TCS	transient component simulation
TES	thermal energy storage
UI	user interface

Table of Contents

List of Figures

List of Tables

Background

This technical report summarizes work done by NREL over a 3-year period for the Concentrating Solar Power (CSP) Systems Analysis project for fiscal years 2019-2021 (FY19-FY21) in support of the U.S. Department of Energy (DOE) Solar Energies Technology Office (SETO). The goal of the CSP Systems Analysis project is to provide timely and accurate CSP cost data to DOE and to project the performance and cost of emerging CSP technologies to inform research directions and industry investment. The CSP Systems Analysis project estimates the current market cost of CSP subsystems and technologies for use by SETO's CSP subprogram and within NREL analysis tools. The project produces modeling tools to evaluate the performance of CSP systems, subsystems, and components. CSP technology costs are estimated and tracked using these tools as well as via analysis of literature and industry sources. The CSP modeling tools and NREL analysis results are used by researchers; government, financial, and industry analysts; and other CSP stakeholders. CSP stakeholders use the tools and analysis to assess the status of CSP technology, track progress toward technology goals, and guide future research.

One of the primary tools used by CSP Systems Analysis is NREL's System Advisor Model (SAM). SAM is a performance and financial model designed to facilitate decision-making for renewable energy industry professionals. The tool includes simulation models for photovoltaic (PV), wind, geothermal, CSP, and other power systems. Within the CSP portfolio are models for power tower, parabolic trough, and linear Fresnel CSP systems. These latter models account for the cost and performance of CSP systems, and they include financial models and dispatch optimization tools for evaluating economic metrics of CSP projects, such as levelized cost of electricity (LCOE) and net present value (NPV).

The CSP Systems Analysis project addresses upgrades to SAM related to CSP, including the development of new modules within SAM to expand the types of CSP systems that can be simulated. The project also explores new tools for evaluating CSP subsystem performance or optimizing CSP system layouts, such as SolarPILOT™ and SolTrace. NREL provides software tools free of charge via NREL's website, and many of these tools, like SAM and SolarPILOT, are available as open-source code. The CSP Systems Analysis project uses these tools to assess the cost of CSP systems. The project also does detailed analysis of CSP systems and its components. NREL engages the national and international CSP community through this project as well.

The work performed by NREL for the CSP Systems Analysis project for FY19-FY21 consisted of four tasks – the objective of each task is presented in the next section. The tasks span a range of topics and are not explicitly related to each other. As such, each task is discussed in its own chapter. The purpose of this report is to document the project scope and results. Most of the work described here is also published elsewhere. More details about the individual tasks performed as part of the project can be found in the publications cited for each task.

Project Objectives and Key Results

The primary goals of the CSP System Analysis project are to provide timely and accurate cost data to DOE to assess the current state of CSP technologies and to predict the performance and cost for pre-commercial and emerging technologies that may impact the industry. Four tasks were completed over a three-year period of performance. The specific objectives and key results for each of these tasks is listed below.

Task 1: CSP Cost Tracking

Objectives:

- Perform bottom-up analysis of commercial and next-generation parabolic trough collectors (PTCs) and heliostats
- Track CSP subsystem and component costs
- Update CSP default cost inputs in SAM.

Key Results:

- We completed bottom-up installed cost estimates of parabolic trough and heliostat designs using design for manufacturing and analysis software. Each study included a commercial design already deployed and an advanced design for future projects.
- Parabolic trough installed costs
    - Commercial design: sbp Ultimate Trough = $152/m^2$
    - Advanced design: Solar Dynamics Sun-Beam MT = $120/m^2$
- Heliostat installed costs
    - Commercial design: sbp Stellio = $127/m2
    - Advanced design: Solar Dynamics SunRing = 96 $/m^2$
- We updated some default costs in SAM CSP modules based on the bottom-up studies
    - Default heliostat costs were updated from the previous value of $140/m^2$ to $127/m^2$
    - Default parabolic trough costs stayed unchanged at $150/m^2$

Task 2: Enhancements to SAM and Other CSP Modeling Tools

Objectives:

- Develop a cavity receiver option for SAM's molten salt power tower (MSPT) model and extend the model library to include additional heat transfer fluids
- Convert the dispatch optimization code in SAM's MSPT model for use in other models that include thermal energy storage (TES).

Key Results:

- We incorporated a working cavity receiver model into SolarPILOT and SAM (version 2021.12.02). The receiver model incorporates an algorithm for view factors between two N-sided polygons that avoids the need for ray tracing and speeds up calculation times. The ability to mesh the cavity surface was added, but we found that meshing the surfaces significantly increases the computational burden of the problem. Meshing increases the simulation times from seconds to minutes. However, meshing all the surfaces results in around a 1% difference. Because of this, only the unmeshed option was offered through the SAM interface.

- We integrated the MSPT dispatch optimization algorithm was with the CSP parabolic trough model. This included adding the dispatch optimization parameters to the user interface and generally making the look and feel consistent with the molten salt tower and IPH models. The dispatch optimization algorithm looks ahead at price signals and plans the charging and discharging of TES tanks to maximize revenue. Compared to the prior heuristic model, the dispatch optimization code was found to reduce CSP costs by >10% for many solar multiple/TES duration combinations. Using the dispatch optimization code to maximize revenue resulted in a 10% reduction in LCOE versus the standard (heuristic) dispatch model for many (but not all) combinations of solar multiple/hours of TES modelled.

Task 3: International Engagement

Objectives:

- Support NREL's Mark Mehos' continuing role as the operating agent for Solar Power and Chemical Energy Systems (SolarPACES) Task I. SolarPACES is the leading international network of researchers focused on utilizing thermal solar energy for power generation, industrial heat, and chemical production technologies. The active international sector provides valuable markets for U.S. CSP developers and knowledge that can be applied to systems in the United States.

Key Results:

- In addition to participating in SolarPACES executive committee meetings and organizing events at SolarPACES conferences, we completed the merger of the OpenCSP international projects dataset maintained by IASS-Potsdam and located on the csp.guru platform with the SolarPACES projects database. The updated database lists CSP projects by country, project name, technology (power plant) type, and status. The update includes newly operating plants in Chile and China. It also includes additional fields in such as jobs (construction, operational) and financial data (normalized LCOE, specific plant costs, renumeration value, etc.).

Task 4: Supercritical CO_2 Power Cycle Modeling

Objectives:

- Analyze the techno-economic feasibility of latent-heat storage integration with an MSPT and the sCO_2 cycle
- Assess sCO_2 cycle analysis and improve off-design performance based on industry feedback
- Publish sCO_2 recompression cycle off-design model and results, request feedback from other national laboratory researchers doing related work and compile the feedback for DOE.

Key Results:

- We configured SAM's MSPT model to approximate a system employing cascaded latent-heat storage using up to four phase change materials for storage temperatures of 450-650°C. We simulated the latent-heat storage case and compared it to the baseline case employing two-tank sensible-heat storage. We found that the latent-heat storage case had lower annual energy generation because it requires a greater temperature difference between the turbine inlet and the receiver outlet than a direct storage system. This requires latent-heat thermal energy storage costs to be lower than the base case sensible-heat storage on a $/kWhth basis to achieve the same LCOE. We calculated the latent-heat storage cost necessary to achieve a

break-even LCOE with the baseline two-tank storage system LCOE for four different sCO_2 power cycle configurations and compared them to latent-heat storage cost estimates. Although we found that the estimated cost of latent-heat storage is lower than the break-even cost of storage calculated, we feel more detailed cost models are needed to verify this result. Future work should also include the impact of off-design operation the sCO_2 power cycle with latent-heat TES.

- Based on industry feedback, we identified several areas for improvement in our off-design sCO_2 model:
    - Modify air-cooler design to not allow for significant over-design operation.
    - Modify cycle control model to not constrain the normalized net power output to be equal to the normalized inlet HTF mass flow rate.
    - Enable cycle model to optimize compressor shaft speed.
    - The off-design heat exchanger model used incompressible fluid assumptions to estimate off-design conductance. The model should be updated to account for compressible fluids.
- To address this feedback, we developed a new cycle off-design convergence and control strategy that removes the mentioned cycle constraints and instead chooses free parameters that maximize objectives while satisfying component and system constraints and limiting the air-cooler fan power to its design value. We also we added the conductance ratio method to our heat exchanger model to estimate the off-design conductance of a compressible fluid. Studies with the new off-design model show:
    - How power and efficiency vary with ambient temperature and HTF mass flow rate while demonstrating that the air-cooler fan power constraint is met,
    - How power and efficiency vary with ambient temperature and HTF mass flow rate,
    - That compressor shaft speed control improves cycle performance by both allowing the cycle to operate at a more favorable thermodynamic condition and allowing the compressors to operate closer to their design flow coefficient, and
    - That shaft speed control can decrease the difference in efficiency between cold-day and hot-day designs.
- We also compared the sCO_2 recompression cycle off-design solutions using different compressor models. We compared the compressor performance map developed by Barber-Nichols Inc. for a roughly 50-kW_e radial compressor currently used in the model to model data provided by Hanwha Power Systems Americas for one of their radial compressor designs. We found no meaningful difference in cycle efficiency or power output between recompression cycles using different compressor models. This gives us confidence, for the purposes of steady-state off-design cycle modeling, that the Barber-Nichols compressor map gives reasonable results. We expect that for our modeling assumptions, the cycle model results will remain similar if the main compressor model has a similar normalized ideal head coefficient and normalized isentropic efficiency responses over a ±10% range of normalized flow coefficient.

The objectives, methodology, results, discussions, and additional insights from each of these completed tasks is described in detail in the sections below.

Task 1: CSP Cost Tracking

Task 1 consisted of three subtasks. In Year 1, we performed a detailed bottom-up analysis of the cost of manufacturing and installing a commercial and an advanced (or pre-commercial) PTC. In Year 2, we did a similar detailed bottom-up analysis for heliostats. In Year 3, we updated the default CSP costs in SAM via an industrial survey. Each of these subtasks is discussed below.

A key tool used in both the parabolic trough and heliostat bottom-up analyses was Design for Manufacturing and Assembly (DFMA), a suite of software tools from Boothroyd Dewhurst. This tool was used in a previous NREL CSP trough analysis which helped determine the installed costs of state-of-the-art and near-commercial parabolic troughs (Kurup and Turchi 2015a).

NREL has utilized DFMA for CSP and several other manufacturing cost analyses for technologies such as geothermal, small hydropower, hydrogen refueling stations, and PV (Akar et al. 2018; Kurup et al. 2018; Mayyas and Mann 2019; Van Geet et al. 2018). The DFMA software package is used industrywide and has two parts: Design for Manufacture (DFM) and Design for Assembly (DFA). For the work in this report, version 3.1.1.173 of the DFM software and version 10.2.2.257 of the DFA software were used (Boothroyd Dewhurst Inc. 2019). The DFMA tool has detailed databases and allows users to calculate a primary manufacturing cost for each component and then the assembly cost to incorporate subcomponents and components within the overall product/assembly. DFM was used for most of the components within the bill of materials (BOM) to model the trough costs assuming commercial manufacturing volumes needed for a large solar field. As such, the materials, manufacturing processes (e.g., stock processes), key dimensions, and machining steps were estimated. Every component that could be directly manufactured in a commercial-scale manufacturing and fabrication shop was modeled. Specialized components, such as receiver tubes and mirror panels, are beyond the DFMA capabilities, and therefore their costs were based on quoted costs.

DFM allows users to produce a detailed "should-cost" number that is based on what a component should cost from the manufacturer; this cost is based on materials, process steps, machine setup time, and tooling, if needed. Tooling investment is calculated for special processes, such as stamping, and considers tool wear and life based on the life volume of the parts needed for the BOM. For this trough analysis, we used U.S. labor rates for the machining processes. We then used DFA to assemble (e.g., weld and rivet) the components together into subassemblies. DFMA was used for the collector frame structure and manufacturing estimates for the pylons. A key feature of the DFMA tool is the built-in ability to change the life volume of the manufactured parts, which enables comparison of the effects of small-scale production versus commercial-scale production.

Parabolic Trough Bottom-Up Analysis

A detailed bottom-up trough analysis for state-of-the-art and near-commercial PTCs was released in 2015 (Kurup and Turchi 2015a). That detailed bottom-up analysis utilized prior knowledge and experience.

We performed a detailed bottom-up analysis of the manufacturing cost of parabolic troughs. Prior to the final selection of two PTC designs, we approached approximately four other CSP

developers. With access to the design and data being key, we worked closely with the developers to finalize the selection of two suitable designs.

We studied the two designs—a commercial design to reflect current costs and an advanced design to demonstrate future cost reduction potential. The commercial design was the Ultimate Trough design from Schlaich Bergermann und Partner (sbp), and the advanced design was the SunBeam-Midterm (MT) design from Solar Dynamics (SD). Table 1 shows the main design parameters for the two steel-based collectors. For the DFMA analysis, the solar field size was a land area of approximately 1 square mile. This is a solar field size needed for an approximately 90-MW_e plant with 6 hours of TES. This analysis and the results were presented at the 2020 SolarPACES annual conference (Kurup, Glynn, and Akar 2020), and are summarized below.

Table 1. Commercial and Advanced Parabolic Troughs Examined in This Study

Property	**Ultimate Trough** (Klaus-Jürgen Riffelmann, Graf, and Nava 2011)	**SunBeam-MT**
Manufacturer	Schlaich Bergermann und Partner (Germany)	Solar Dynamics (United States)
Reflector type	4-mm glass	4-mm glass
Solar collector assembly (SCA) length (m)	247	200
Solar collector elements (SCEs) per SCA (standard)	10	8
Receivers per SCA	5	6
Aperture width (m)	7.51	8.20
SCE length (m)	24.5	24.8
SCA aperture area (m^2)	1,715	1,576
Frame design	Torque box	Space frame
Primary frame material	Steel	Steel
Total number of SCAs	468	510
Solar field total aperture area (m^2)	802,620	803,760

The Ultimate Trough is a large-aperture trough with a similar aperture width (7.5 m) as the SunBeam trough (8.2 m). Figure 1 (left) shows the SD SunBeam near-term (NT) prototype at the Solar Technology Acceleration Center (SolarTAC). Figure 1 right shows the Ultimate Trough test loop at Harper Lake in California. Note, the NREL analysis was undertaken on the SunBeam-MT as this is the design that is likely to be deployed for large solar fields.

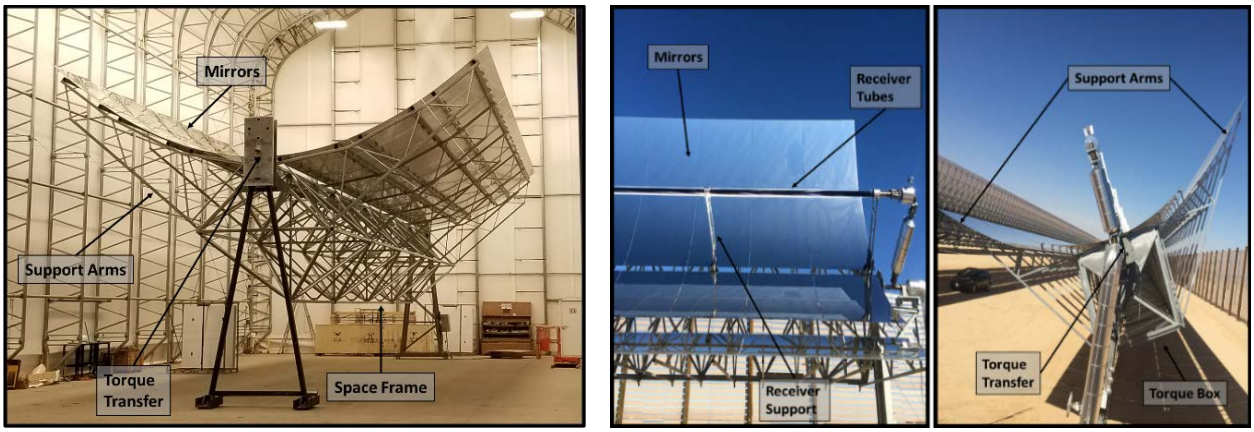

Figure 1. Left: Full-scale SunBeam near-term (NT) prototype at the SolarTAC facility in Colorado. Right: Full-scale integrated Ultimate Trough in California.

Left: Photo from Solar Dynamics. Right: Photo from Schlaich Bergermann und Partner.

Figure 2 shows the sbp Ultimate Trough installed solar field on the Saudi Arabian coast. The Ultimate Trough solar field is part of the Duba Green Integrated Solar Combined Cycle Power Plant, where the solar field provides a heat input of up to 50 MW_e (or about 120 MW thermal, MW_{th}) to the natural gas combined cycle of 565 MW_e (K.-J. Riffelmann et al. 2019; sbp 2017). The Duba Green Power Plant is the first Ultimate Trough commercial realization in the Kingdom of Saudi Arabia (KSA). At this plant, 124 solar SCAs are installed for a field aperture area of approximately 170,000 m^2, with a loop length of 800 m. The Ultimate Trough design was modified for the Saudi Arabian environment (e.g., increased galvanization for the steel structures to mitigate corrosion due to proximity to seawater). Although the solar field is much smaller than 1 square mile, the overall design is considered commercially deployed.

Figure 2. Ultimate Trough installed solar field in the KSA with a 170,000-m^2 total aperture area.

Photo from Schlaich Bergermann und Partner (K.-J. Riffelmann et al. 2019).

In 2015, NREL modeled the Ultimate Trough at larger scale (Kurup and Turchi 2015b). We updated the parts and production methods in the DFM, DFA, and estimated construction analysis from this prior work to reflect current costs and the manufacturing volume needed for a 1-square-mile solar field suited for approximately a 90-MW_e plant with six hours of TES and a total aperture area of approximately 800,000 m^2.

The prior estimated manufactured and installed cost (in 2015 dollars) for the Ultimate Trough was $178/m^2, which included an assembly facility of $11 million (M) amortized over the required production volume (Kurup and Turchi 2015a). This did not account for a 5% site labor cost on the manufactured and purchased components, which would have increased the installed cost to $187/m^2. The current analysis shows a decrease of 15% in the installed cost compared to the prior analysis ($152/m^2 compared to $178/m^2). The primary decrease is in the receiver tube costs, which decreased by approximately $12/m^2. Secondarily, manufacturing process adjustments within the DFMA models have reduced the cost of some manufactured steel parts by approximately $7/m^2. In the 2020 model, U.S. steel prices were utilized. It is important to highlight that the shipping costs have therefore been changed from international in the 2015 model to domestic (i.e., within the United States) for the 2020 model. This change in the shipping calculation also contributes to the decrease in cost. For the Ultimate Trough update, revised mirror and receiver tube values were used (i.e., as in the SunBeam-MT analysis). This is because it is expected that if the Ultimate Trough design were built today, the cost savings from today's mirrors and receiver tubes would benefit a new commercial plant.

From the analysis presented in the SolarPACES paper, the installed cost estimate for the commercial Ultimate Trough was found to be $152/m^2 for 468 SCAs. Figure 3 (left) shows the breakdown of the Ultimate Trough installed cost for 468 SCAs, which have a total field aperture area of 802,620 m^2. As seen in Figure 3 (left), key contributors to the Ultimate Trough installed cost are the cantilever arms (21%), torque box (20%), and mirror panels (16%). Figure 3 (right) shows that the total purchased parts make up ~33% of the installed cost, whereas the manufacturing components make up approximately 53%. The Ultimate Trough has cost reduction potential, e.g., through an increased aperture width of 10 m and the use of molten salt (Kurup, Glynn, and Akar 2020).

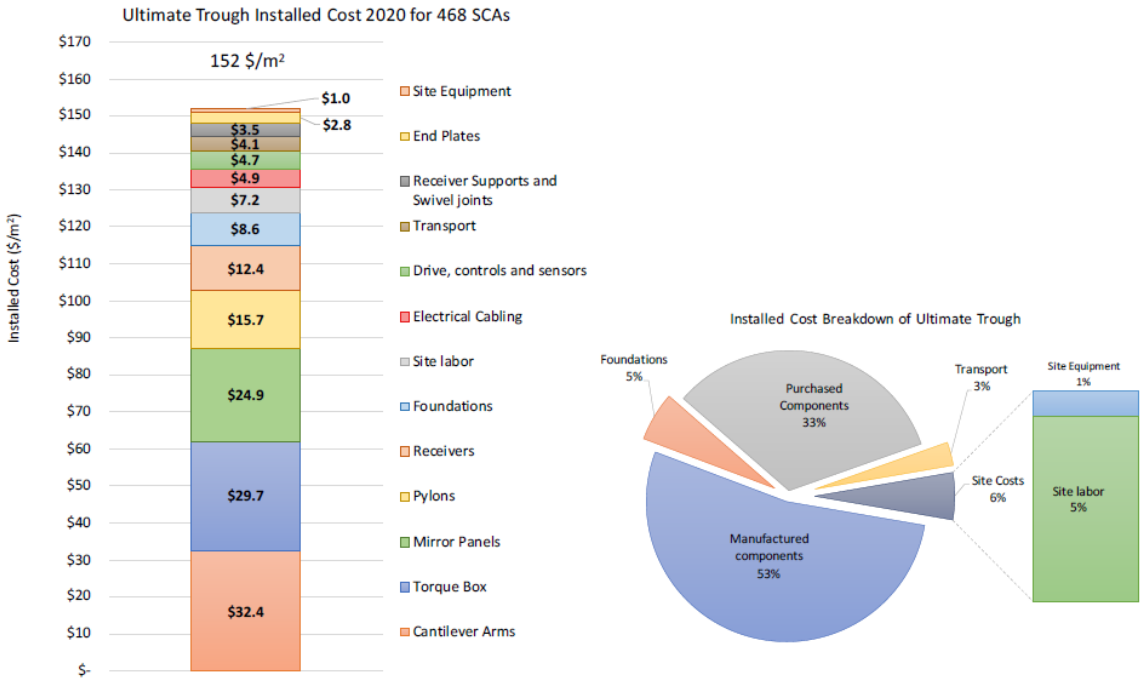

Figure 3. Bottom-up installed cost breakdown for the sbp Ultimate Trough.

This cost estimate is within ±10% of sbp's estimate for the Ultimate Trough installation in Duba.[1] Key German Aerospace Center (DLR) work is also highlighting the Ultimate Trough as a commercial trough in their recent analysis, which looks at the Ultimate Trough potential installed costs today and in 2030 (Dersch et al. 2020). In the DLR work, which looked at how the potential costs of the Ultimate Trough solar field could change based on a price index (where Morocco was 100 and the United States was 114 (Dersch et al. 2020)), the U.S. installed cost for the Ultimate Trough was found to be roughly $145/m^2 (Kurup, Glynn, and Akar 2020; Dersch et al. 2020). This is within just 5% of the conservative NREL estimate of 152/m^2, highlighting that the independent methods and analysis of NREL and DLR provide results that can triangulate the potential costs of installed solar fields and lead to research paths for further reductions.

In future deployments, both the SunBeam-MT and the Ultimate Trough are expected to utilize molten salt, which is likely to reduce costs further, as the overall solar field size can be reduced. For example, analysis has found that when molten salt is used for the Ultimate Trough in place of Therminol VP-1, for two 100 MW_e plants with similar amounts of storage, the LCOE decreases by approximately 20% (Ruegamer et al. 2014). This cost reduction is driven by the increase in operating solar field temperature (e.g., from 393°C to 550°C) and the resulting increase in steam turbine operating conditions, the reduced solar field needed for the molten salt field versus a synthetic oil field, and the increase in energy density for thermal energy storage using molten salt case which decreases its relative cost.

The Ultimate Trough is a highly developed and progressed steel tubular design that is suited for high local content. It has been designed to use standard receivers (4.06 m) and longer tubes (4.88 m). The Ultimate Trough has been designed for very large solar fields, e.g., 1 million m^2. Like the SD design, fully robotic assembly and welding are expected for large enough Ultimate Trough fields.

The NREL Ultimate Trough reference is ~800,000 m^2, compared to 170,000 m^2 for the Duba Green Power Plant. Discussions with sbp indicate that the Duba solar field may not reach the estimated cost of $152/m^2 due to wind loads, corrosion prevention requirements, and its smaller scale. Work from DLR, where the Ultimate Trough is used as today's reference system, found that the solar field cost in 2018 dollars could be approximately $127/m^2 in Morocco, albeit for a larger solar field (Dersch et al. 2019). This solar field, like the NREL analysis, includes the collector structure, pylons and foundations, mirrors, receivers, and drives and electricals, but not the site preparation, heat transfer fluid (HTF) in the solar field, and the HTF system. With a price index of 100 for Morocco and a price index of 114 for the United States (Dersch et al. 2019), the U.S. installed cost for the Ultimate Trough could be roughly $145/m^2. This aligns well with both the NREL estimate for the United States of $152/m^2 and the DLR estimate of $145/m^2 using the labor multiplier method.

Improvements to the Ultimate Trough (e.g., molten salt and next-generation 10-m aperture) are not incorporated here, but could reduce cost further (Dersch et al. 2019). The use of molten salt

[1] sbp did not have direct access to the Duba site data kept by the engineering procurement contractor (EPC). As such, sbp does not have significant cost breakdowns of the Duba solar field. However, sbp agreed to review the work to provide comment on the NREL DFMA validation efforts.

in the solar field leads to a reduced solar field size and higher steam turbine efficiencies due to the increased operating temperature of the field compared to oil-HTF (e.g., 550°C compared to 393°C). It also reduces thermal energy storage costs by increasing the temperature difference in the storage tanks increases stored energy density and decreases storage tank size requirements. For example, DLR analysis found that if a 100-MW_e Ultimate Trough solar field was situated at Daggett, California, and switched from VP-1 to molten salt as the HTF, a 20% LCOE reduction was possible (Ruegamer et al. 2014).

NREL collaborated with solar collector developer Solar Dynamics (SD) LLC to analyze the cost of their pre-commercial SunBeam-MT parabolic trough design. SD's SunBeam-MT large-aperture trough has an aperture width of 8.2 m and a net aperture area of 195 m^2 per SCE. Its development was based on the Advanced Trough With Lower-Cost System-Architecture Design (ATLAS)[2] collector, which was supported by contracts from DOE (DOE 2014).

The SunBeam-NT is similar in most respects to previous state-of-the-art large-aperture steel space frame troughs, such as the Abengoa SpaceTube (8.2 x 16 m per SCE) (Marcotte and Manning 2014). It retains similar aperture width and mirror shape, similar steel component and fastener types, and a similar assembly strategy. The SunBeam-NT uses a more efficient frame layout, which enables approximately 30% lower mass content through the reduced number of parts and fasteners per square meter of aperture, and a 50% longer concentrator length (8.2 x 20 m per SCE). The SunBeam-MT version is based on the same space frame truss as the NT, but it is 25 m long to further reduce pylon and foundation counts, and it employs a new, innovative mirror support structure design and mirror attachment, which eliminates the need for adjustable mirror attachment brackets and costly on-site bracket alignments. Both NT and MT variants use industry-standard 4-mm glass mirror technology that is common in other parabolic trough designs, such as the EuroTrough and the Ultimate Trough.

The key subsystems for the SunBeam-MT are the receiver tubes, receiver supports, mirror panels, riveted arm assemblies, space frame, torque transfer plates, drives and controls, foundations, drive pylon, and regular pylons. The analysis for the SunBeam-MT includes estimated field assembly and construction activities. These estimates are based on detailed work undertaken for DOE on the ATLAS trough, where the construction, tooling investments, and solar field assembly activities were estimated for a similar sized ATLAS trough solar field (O'Rourke and Farr 2015). Figure 4 shows the SCE for the SunBeam-NT at SolarTAC.

[2] https://www.energy.gov/eere/solar/project-profile-abengoa-solar-llc-atlas

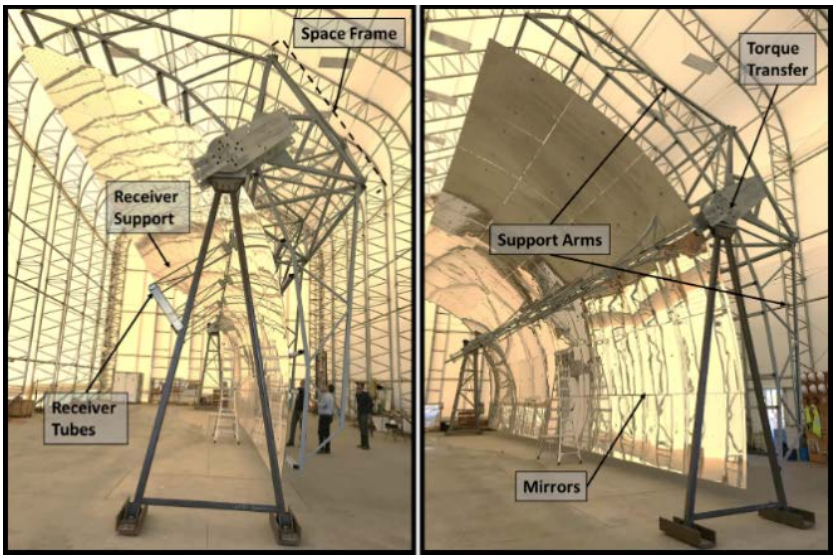

Figure 4. Full-scale SunBeam near-term (NT) prototype at the SolarTAC facility in Colorado.

Photo by Sertac Akar, NREL

We completed the DFM modeling for each component at the volumes needed for the 1-square-mile solar field. For each subcomponent, a variety of manufacturing techniques, including sheet metal stamping and forming, hydraulic tube crimping, and computer numerical control machining, are available. For each subcomponent, we chose the manufacturing technique that met the design requirements and minimized manufacturing costs for the quantity manufactured or the lifetime volume. As an example, the SunBeam MT End Truss subsystem includes 13 subcomponents. Figure 5 shows the cost vs. life volume sensitivity of the 13 specific subcomponents within the End Truss. The results show that the manufacturing volume is enough to achieve the minimum manufacturing cost using the selected method of manufacturing. In the case of the End Truss, laser tube cutting was utilized. We found that for the large volumes of parts required for this scale of solar field, the minimum manufacturing cost is achievable in most cases.

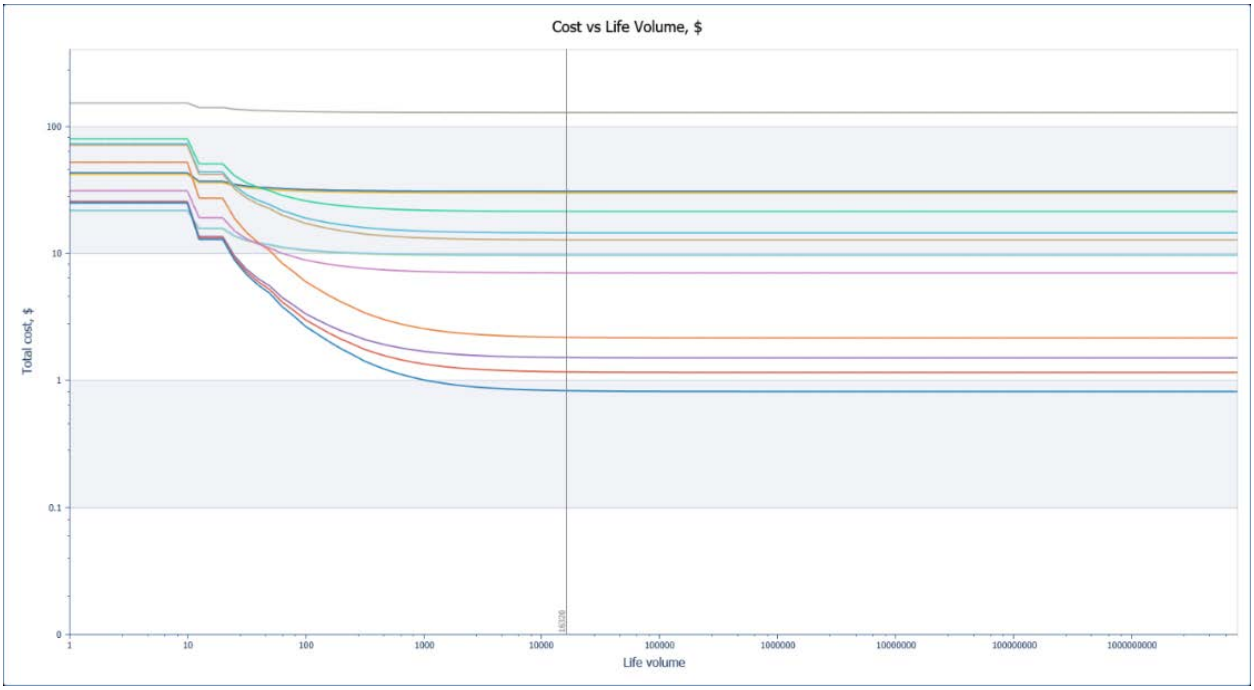

Figure 5. Sensitivity analysis for cost vs. lifetime manufacturing volume of all 13 components in an End Truss subsystem.

To complete the DFA cost analysis, we collected the required welding and self-pierced riveting operation details from SD. The assembly operations include welding and/or riveting, reorientation of subassemblies, and having subassemblies ready for shipment to the site. SD also provided vendor quotations for the purchased components that will complete the SCAs at the appropriate quantities. These include the control systems, drive hydraulics, interconnects, electrical cabling, receiver tubes, and mirrors.

Figure 6 (left) shows the breakdown of the SunBeam-MT installed cost for 510 SCAs. The installed costs as a proportion of the total installed cost (including purchased parts) are shown in Figure 6 (right). The bottom-up analysis, as highlighted in the SolarPACES paper (Kurup, Glynn, and Akar 2020), led to an installed solar field cost estimate for the SunBeam-MT of approximately $\$120/m^2$. For an advanced or near-term future design, if realized, this is 20% less than the SAM 2020.11.29[3] installed cost parameter of $\$150/m^2$ for the solar field. This amount includes a manufacturing investment to purchase tooling for specific space frame components. The $860,000 manufacturing investment is included for subsystems such as the tooling required for the stamping machine for the plates and the specifically shaped dies needed for the steel extrusions (e.g., the struts in the space frame). When the manufacturing tooling investment is amortized over 510 SCAs, it adds less than $\$1.1/m^2$ to the manufactured cost. SD has reviewed this work and found it to be accurate and within ±10% of their own project estimates, e.g., in bids they are making for projects of similar size.

[3] https://sam.nrel.gov/download.html

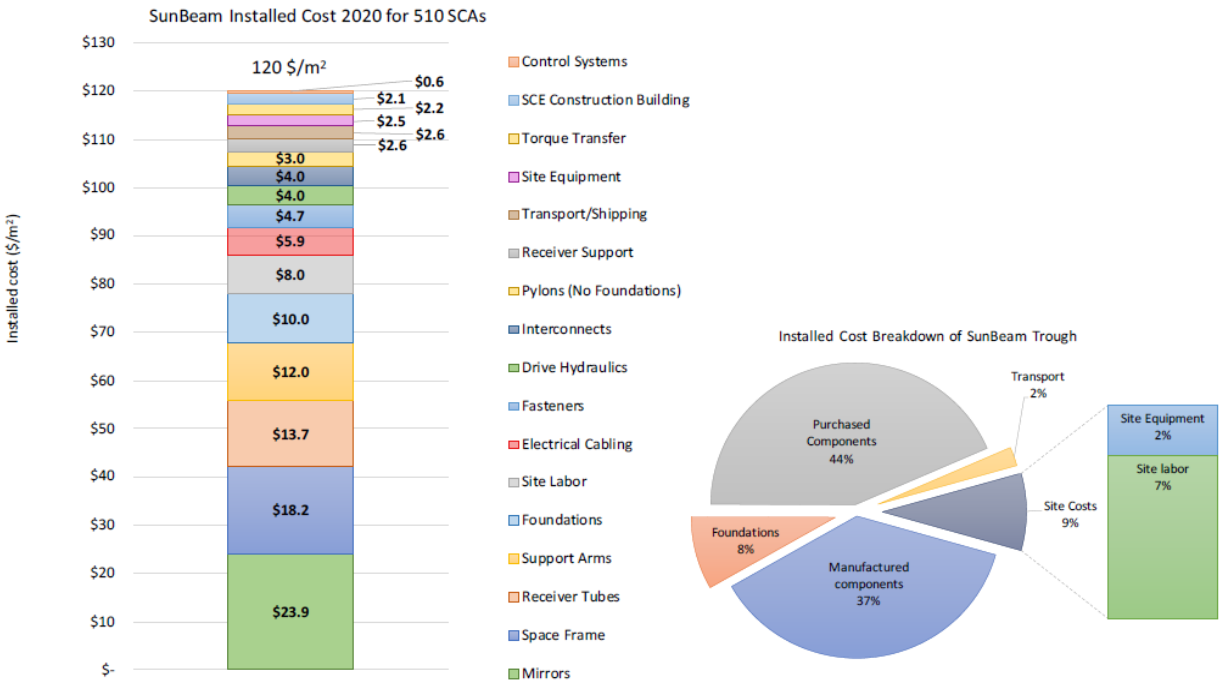

Figure 6. Bottom-up installed cost breakdown for the SD SunBeam-MT trough.

As seen in Figure 6 (left), the biggest contributors to the installed cost are the mirrors (20%), the space frame (15%), and the receiver tubes (11%). Figure 6 (right) highlights that the total purchased parts are ~44% of the breakdown. This indicates that the SD design is being developed from the perspective of buying standard products, which, as large supply chains are established, could be a significant cost driver. The use of fully automated robotic assembly for the SunBeam-MT (outside of the current analysis) could save up to 10% in assembly labor costs if all assembly processes for the space frame, arms, and receiver supports are switched to robotic riveting. This could then lead a further 3% savings in the total installed cost of the SunBeam-MT system (Kurup, Glynn, and Akar 2020).

NREL initially estimated the solar field construction and in-field assembly costs from detailed estimates for the Abengoa ATLAS trough (O'Rourke and Farr 2015). NREL estimated the field assembly, factory, and tooling costs to be $12.63/m^2 (Kurup, Glynn, and Akar 2021a). For an estimate specific to the SunBeam-MT, NREL contracted an external construction expert to help estimate the field construction and assembly costs for the parabolic troughs being studied. The contractor performed detailed construction analysis of the SunBeam-MT at the scale NREL analyzed, i.e., ~800,000 m^2. Note that this adds to the initial construction analysis, e.g., specific numbers of workers, on-site assembly facility analysis, and further details on the specific machines needed for the construction activities. The SunBeam-MT has yet to be installed at scale, and therefore the construction cost estimates have some uncertainty associated with them, which the external contractor helped reduce further. NREL received a final summary report, which detailed the construction activities, equipment involved, and an overall estimate for the solar field construction installed cost from the external contractor. The report does not take specific ground conditions into account for specific sites. The external contractor estimated the field assembly, factory, and tooling cost for the representative SunBeam-MT solar field to be

$12.23/m^2, compared to NREL's previously published estimate of $12.63/m^2 (Kurup, Glynn, and Akar 2021a). While the initial estimate from NREL was close to the final value from the external contractor, the summary report, which is internal to DOE and NREL, provided additional valuable insights from its level of detail and insight into the on-site construction process.

The main output from the detailed bottom-up parabolic trough analysis was the accepted SolarPACES 2020 paper "Manufacturing Cost Analysis of Advanced Parabolic Trough Collector" (Kurup, Glynn, and Akar 2021b). The poster was also presented at SolarPACES 2020 online. The major results include the estimation of the commercial and advanced trough installed costs of $152/m^2 and $120/m^2, respectively (both in 2020 dollars).

This detailed analysis helps form the basis for understanding parabolic trough developments in the market as the scale of solar fields and aperture widths increases. Through collaboration with U.S. and foreign companies, this type of work adds to the global understanding of today's estimated cost, reduction opportunities, and potential future pathways. In the future, this type of analysis can be fed back into new releases of the Annual Technology Baseline (ATB) to help track and develop projections for CSP trough costs and LCOE for today's most deployed CSP technology. The detailed analysis further confirms SAM cost values. For instance, at present, the installed solar field cost in SAM is $150/m^2, very close to the $152/m^2 found in this work.

This research also highlights the need for an increased focus on molten salt troughs. Overcoming challenges associated with molten salt use in a network of pipes and in the solar field (e.g., freeze protection and line tracing) would allow for the use of molten salt, which in turn would allow for parabolic trough fields and TES systems to be reduced in size and steam turbine operating temperatures to be increased. These effects would reduce the LCOE of molten salt parabolic trough plants if associated risks of salt-in-the-field are overcome. DLR, the University of Evora, and other industrial partners are already testing molten salt troughs in demonstration loops (List Solar 2021) to help de-risk the technology and support its commercial development.

Heliostat Bottom-Up Analysis

NREL performed a bottom-up analysis of the manufacturing costs of heliostats of two designs—a commercial design to reflect current costs (commercial design), and an advanced design to demonstrate future cost reductions (advanced design). Full details can be found in the recently published report (Kurup et al. 2022). This section summarizes the bottom-up work undertaken in Years 2 and 3 of this effort. Prior to the final selection of the two heliostat designs, approximately five other heliostat developers were approached. With access to the design and data being key, NREL worked closely with the developers to finalize the selection of two suitable designs.

NREL analyzed the Stellio heliostat design from sbp for the commercial design and the SunRing heliostat design from SD for the advanced design. The modeled heliostat field area was ~1.1 million square meters (Mm^2) in total solar field aperture area. This modeled ~1.1 Mm^2 solar field is suited for an 80-MW_e CSP power tower plant with 12–16 hours of TES based on SAM analysis. See Table 2 for details on each design.

Table 2. Commercial and Advanced Heliostats Examined in This Study

Property	Stellio	SunRing
Developer	sbp (Germany)	Solar Dynamics (United States)
Reflector type	4-mm glass	4-mm glass
Individual heliostat aperture (m^2)	48.5	26.7
Heliostats per field (based on 1.1 Mm^2 field)	22,239	40,000
Design geometry	Pentagonal	Rectangular
Design drive type	Linear actuators	Linear actuator, DC gearmotor
Primary frame material	Steel	Steel

The Stellio heliostat design was developed by DLR, sbp, and others through a German-Spanish consortium. The consortium commercialized the Stellio heliostat (Kraemer 2019), and it is now deployed at the Chinese 50-MW Hami site (Keck et al. 2019), which includes 13 hours of molten salt storage (Kraemer 2019). Figure 7 shows the installed pentagonal Stellio heliostats.

Figure 7. Installed Stellio heliostats with flat glass panels.

Photo from Schlaich Bergermann und Partner

As shown in Figure 8, the Stellio heliostat is composed of subassemblies that include the foundation, cantilever arms, a central hub, mirrors (Inner Facet, Facet-1, and Facet-2), purlins, the pylon base, the pylon head, a linear actuator, and the control system. With NREL access to the sbp Stellio heliostat design, including CAD drawings and pylon information, we prepared the BOM and used DFM analysis to estimate the cost of manufacturing each subcomponent. sbp also shared price estimates for outsourced parts (mirrors, electrical cabling, drive hydraulics, control systems, fasteners, linear actuators, pads, cardan, and connection parts).

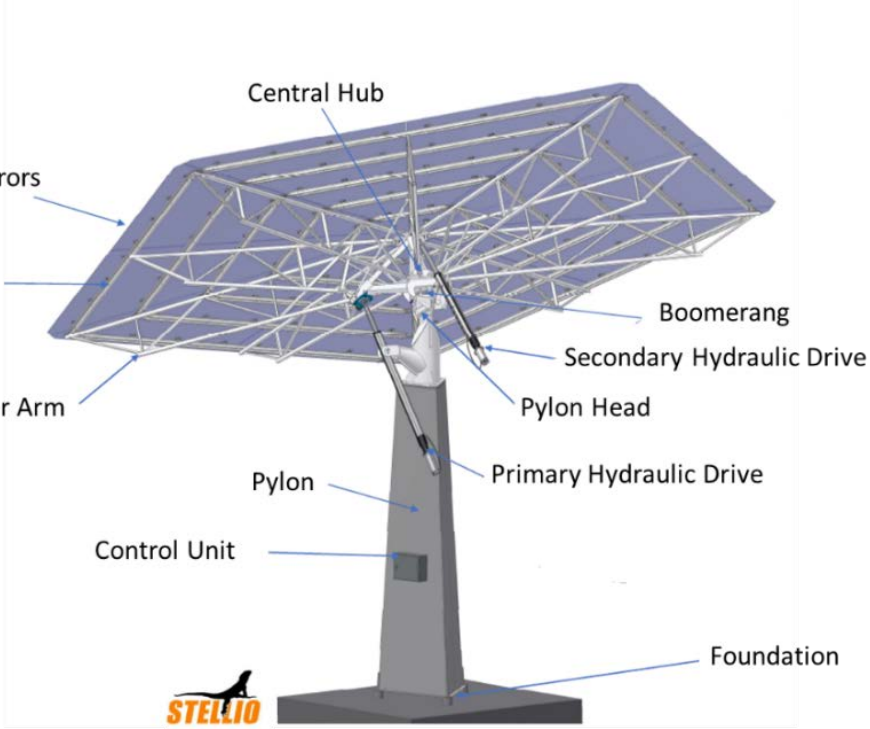

Figure 8. Schematic showing the main components of the sbp Stellio heliostat.

Image from Schlaich Bergermann und Partner

Next, we undertook DFA analysis for the subassembly work and developed estimates for the construction activities (solar field assembly and installation). The capital costs for the assembly building adjacent to the solar field site, the assembly lines, the overhead cranes, and the rest of the equipment (such as trolleys and heliostat transportation platforms) are based on the months available for the solar field execution. We assumed that one assembly line for the Stellio would be constructed, with an estimated capital expenditure (CAPEX) of $7.5M. This was the estimate used in the NREL analysis (Kurup et al. 2022). Discussions with sbp have highlighted that the execution time can be reduced by approximately 6 months by adding another assembly line, while the CAPEX for two assembly lines is less than double the CAPEX for a single assembly line.

Figure 9 (left) illustrates the cost breakdown of the Stellio heliostat design. From our analysis, the current total installed cost estimate is ~$127/m^2 for 22,239 heliostats, which includes an on-site adjacent assembly facility cost of ~$7.5M. This is for a solar field of size 1,078,592 m^2. Each heliostat has a reflective area of ~48.5 m^2. The major cost contributors are the base assembly (15.7%) and mirrors (13.4%). Purchased parts are the largest contributor to the total installed cost (44%). As seen in Figure 9 (right), the manufactured parts and their fabrication into subassemblies that are shipped to the field represent 31% of the installed cost and are the second largest cost contributor.

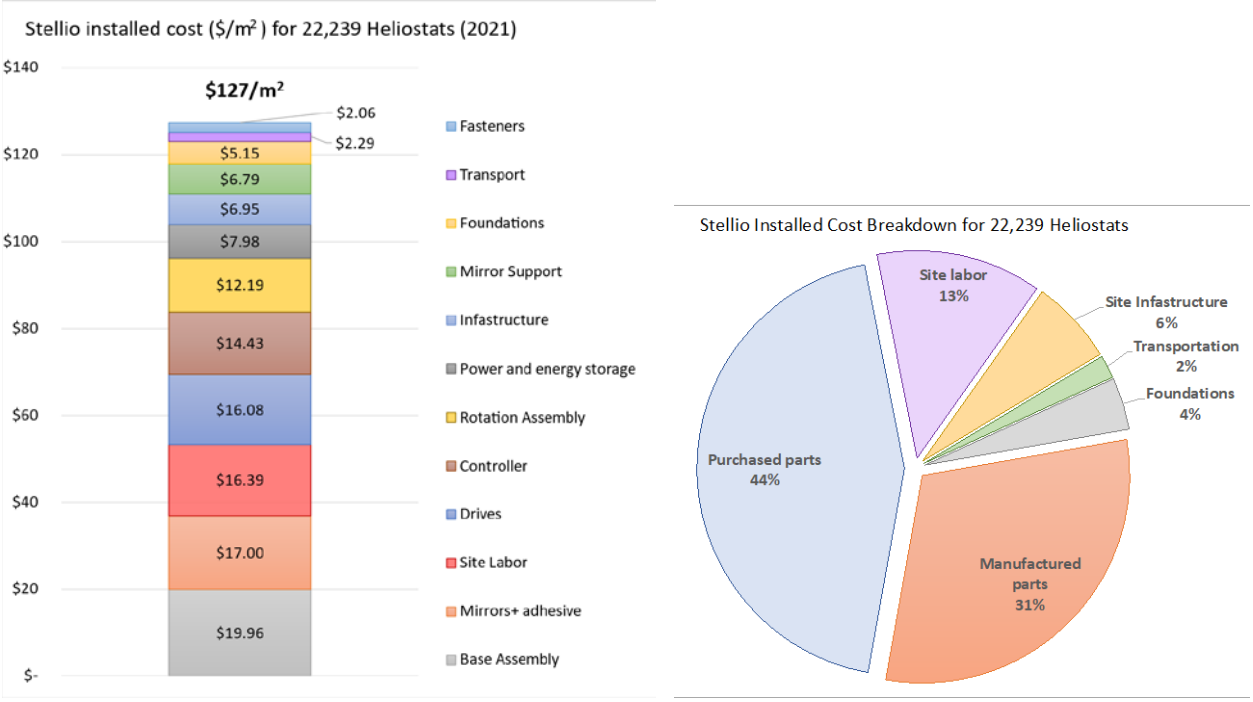

Figure 9. Stellio estimated installed cost (left) and breakdown by category (right).

NREL also worked with SD to estimate the cost of their pre-commercial SunRing heliostat design using bottom-up analysis. Figure 10 shows the SD SunRing prototype at the SolarTAC facility outside of Denver, Colorado. SD's SunRing heliostat is an advanced and developing heliostat design that is an evolution of the Ring of Power (ROP) concept developed by Abengoa. It uses six 1.4-m x 3.21-m mirror facets in a canted configuration. Drives facilitate rotation of the heliostat about its base (azimuth) and alter the angle of the mirrors relative to the base (elevation).

Figure 10. SunRing prototype at the SolarTAC facility.

Photo from Solar Dynamics

The SunRing heliostat is composed of the subassemblies depicted in Figure 11, such as the structures and azimuth track. Ground anchors and mounts bolt to the geared azimuth ring. The base assembly has wheeled hubs that ride on the circular tube of the azimuth ring, and its rotation about the ring is controlled by a roller pinion that engages the azimuth gear. The lower structure forms the triangulated frame between the base assembly and the mirror support structure. The mirror support structure consists of two tubes with a series of brackets welded to them. The brackets allow for bolting of the mirror ribs to the mirror support structure and create the mounting points for the pivot to the lower support structure and the linear actuator that controls the elevation angle of the mirrors. The mirrors are adhered to the mirror ribs. Adjacent to the mirrors is a small PV panel that is used to provide power to the heliostat controls and drives.

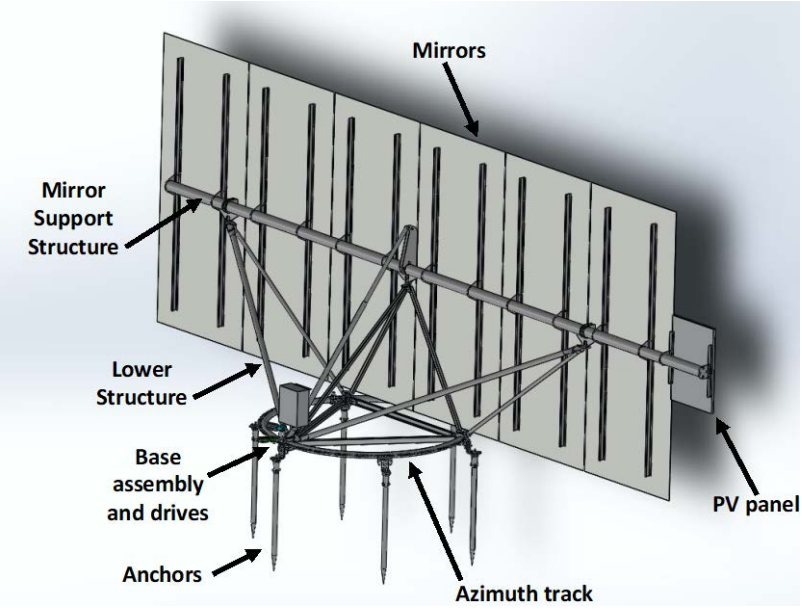

Figure 11. Rendering of SunRing heliostat shown from behind mirrors.

CAD model drawing from Solar Dynamics. Image by Stephen Glynn, NREL.

For each subassembly, we assessed engineering drawings and CAD models provided by SD. The drawings and models allowed for precise input of the dimensions, tolerances, and material specifications into DFM and DFA. The subassemblies were broken down into individual components for cost modeling within DFM. Subsequently, the components were assembled into their respective subassemblies within DFA. Most of the parts are made of low-carbon structural steel and are galvanized after being made into subassemblies. Many of the parts were designed with high-volume manufacturing in mind, allowing for the utilization of stamping processes. The components and subassemblies were modeled at the appropriate volumes to assemble 40,000 heliostats. The purchased component costs were from vendor estimates and quotes provided to NREL, and were based on the scale of the field installation. The mirrors, fasteners, bushings, rollers, axles, battery, PV panel, drives, and controllers were all purchased components.

Figure 12 illustrates the cost breakdown of the SunRing heliostat design. From our analysis, the current total installed cost estimate is ~$96/m^2 for 40,000 heliostats, which includes an on-site assembly facility of ~$880k. The solar field area is approximately 1,078,592 m^2. Each heliostat has a reflective area of ~27 m^2. The major cost contributors are the linear actuator drives

(16.6%), the mirrors (16%), the steel base assembly (11.2%), the foundations (9.3%), and the fasteners (8.7%). Figure 12 (right) shows that purchased parts account for ~54% of the total heliostat cost. Manufactured components are only 27% of the total cost. The SunRing represents the installed cost potential of an advanced heliostat design that has yet to be demonstrated at scale.

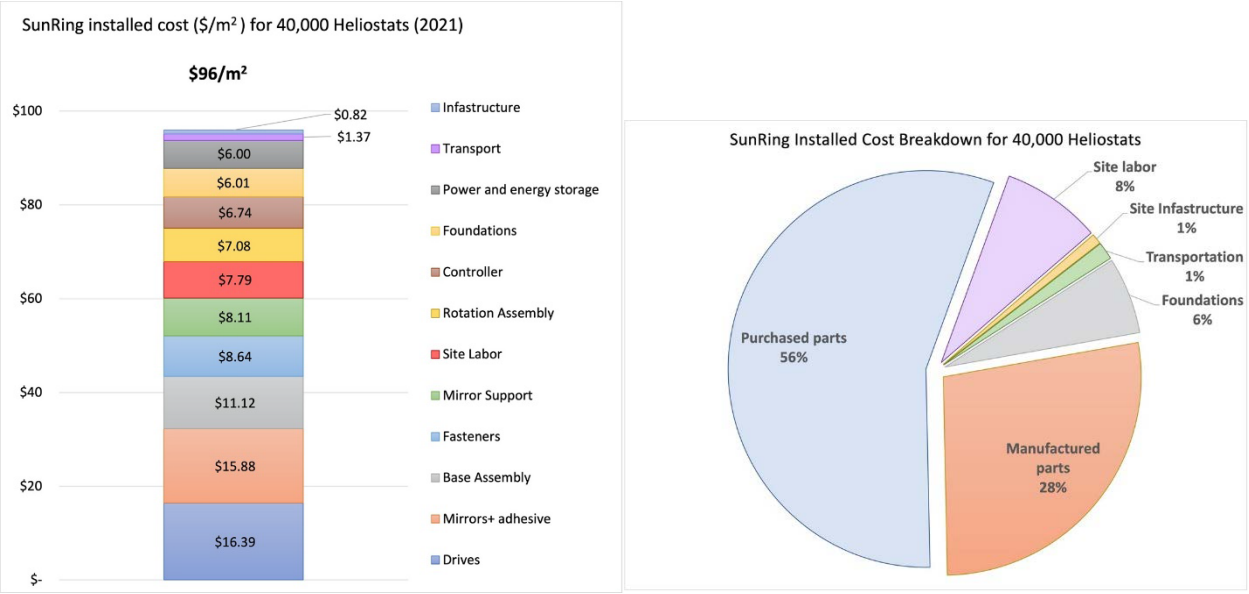

Figure 12. SunRing estimated installed cost breakdown (left) and breakdown by category (right).

Working together with sbp and SD, we determined key insights into heliostats. It is important to note that the innovative pentagon-shaped Stellio was developed in a consortium with research (DLR), industry (Ingemetal and Masermic), and the developer (sbp). The Stellio was taken from the lab to commercially ready in 5 years (Kraemer 2019). DLR has been involved in significant performance testing. Discussions with sbp highlight the learnings from the installation of the heliostats at the Hami field, and these learnings are being utilized in the next fields. For example, the use of driven piles for the pylon instead of concrete foundations led to an approximately 20% reduction in the field installation cost. This technique is now going to be deployed at the Redstone heliostat field in South Africa. The NREL analysis already includes the foundation changes as part of the improvements that could be implemented in the United States. DLR analysis has estimated that the potential Stellio installed cost in 2025 could be $103/m^2 in 2016 dollars (Dieckmann et al. 2017). Key developments for the Stellio through 2025 include: a reduction in the site preparation costs, e.g., through driven piles or earth screws, by nearly 50% ($11/m^2 to $5.5/m^2); improved maintenance programs and closed loop control, which could reduce drive costs by 25% ($45/m^2 to $33.8/m^2); and a reduction in structure costs, which can be reduced by approximately 25% via reduction in materials and increased automation and assembly procedures (Dieckmann et al. 2017). With growth in the commercial heliostat market due to increased power tower deployment, there is potential for an estimated 35% cost reduction through product standardization and improved canting procedures (Dieckmann et al. 2017).

The SD SunRing is also an innovative design, and it has a future installed cost goal of $50/m^2 (Kattke 2019). Based on Abengoa's ROP, the SunRing concept is designed for simple assembly

and foundation installation, e.g., through screws or ground anchors. It is likely that the ground conditions will determine the use of specific ground penetration mechanisms. The NREL analysis was conducted with six helical piles for the foundation. The use of large, flat mirrored apertures eases the manufacturing and assembly tolerances for the heliostat facets. A key design choice is that the majority of the manufactured parts do not require additional machining steps, allowing for precision stamping to be utilized for high-volume manufacturing. This is a good way of reducing further manufacturing and processing steps. Another design choice is the utilization of off-the-shelf stepper motors and linear actuators to simplify the tracking and design and reduce cost. Similar to the parabolic trough analysis with SD, detailed estimates of the heliostat field assembly stations, equipment, and labor were calculated with support from an external contractor to accurately estimate installation costs, because the SunRing has yet to be deployed. The SunRing has been through various testing modes, such as wind tunnel, structural, and optical testing (Kattke 2019).

This section reproduces the LCOE impacts for the cost of the solar fields found in (Kurup et al. 2022). To understand the impact of the heliostat installed cost on the overall power tower plant cost and therefore on LCOE, we created a SAM simulation with three scenarios: default heliostat (today's current cost in SAM), commercial heliostat (sbp), and advanced heliostat (SunRing). To allow for comparison, the default scenario uses the pre-built heliostat (144.4 m^2 per individual heliostat in Table 3). The same SAM default values for heliostat performance were used for all three scenarios; the simulations do not use the optical performance of the commercial and advanced heliostat designs. The three scenarios were created using very similar SAM field conditions, but the installed cost is reflective of the commercial and advanced costs determined in the bottom-up analysis. As seen in Table 3, the total CAPEX amounts for the installed heliostat fields are approximately $151.0 M for the current default and $137.0 M and $106.8 M for the commercial and advanced cases, respectively. The commercial and advanced heliostat fields could reduce the overall solar field cost relative to the current default by 9.3% and 31.5%, respectively, as shown in Table 3.

Table 3. Default, Commercial, and Advanced Heliostat CAPEX Scenarios

Solar Field Category	Default Heliostat	Commercial Heliostat Cost	Advanced Heliostat Cost
Site improvements ($/m²)	16	16	16
Individual heliostat aperture area (m²)	144.4	48.5	27.0
Number of heliostats	7,470	22,237	39,944
Solar field size (m²)	1,078,480	1,078,495	1,078,488
Solar field installed cost ($/m²)	140	127	96
Total installed heliostat field cost ($)	$151.0 M	$137.0 M	$103.5 M
Potential decrease in overall solar field CAPEX (%)	0%	-9.3%	-31.5%

Table 4 highlights the other key cost categories (e.g., HTF and TES costs, power plant and balance of plant costs) and financial parameters used for the techno-economic analysis in the SAM cases. For the techno-economic analysis and SAM scenarios, Tucson, Arizona (Location 1)

Table 4. Default, Commercial, and Advanced Cost Cases in SAM and the Impact on LCOE

SAM System Cost Category	Default Heliostat Cost	Commercial Heliostat Cost	Advanced Heliostat Cost
Location			
Location 1	Tucson, AZ	Tucson, AZ	Tucson, AZ
Annual generation (GWh) at Location 1	396.844	396.844	396.844
Location 2	Daggett, CA	Daggett, CA	Daggett, CA
Annual generation (GWh) at Location 2	409.423	409.423	409.423
Heliostat Field			
Solar field installed cost ($/m^2)	140	127	96
Total installed heliostat cost ($)	$151.0 M	$137.0 M	$103.5 M
Tower and Receiver			
Tower ($)	20.9 M	20.9 M	20.9 M
Receiver ($)	60.9 M	60.9 M	60.9 M
Thermal Energy Storage			
TES cost ($/kWh$_{th}$)	22.0	22.0	22.0
TES total cost ($)	34.1 M	34.1 M	34.2 M
Power Cycle			
Gross power block (MW$_e$)	80	80	80
Power cycle cost ($/kW$_e$)	1,040	1,040	1,040
Balance of plant cost ($/kW$_e$)	290	290	290
Other Cost Categories for Locations 1 and 2			
Contingency on direct CAPEX (7% default)	$27.3 M	$26.3 M	$24.0 M
Indirect – EPC and owner costs ($)	$54.3 M	$52.3 M	$47.7 M
Indirect – total land cost ($)	$9.5 M	$9.5 M	$9.5 M
O&M fixed cost by capacity ($/kW$_e$-yr)	66	66	66
Total Installed Costs for Locations 1 and 2 ($)	$498.2 M	$480.7 M	$367.0 M
Finance Assumptions			
Analysis period (years)	25	25	25
SAM LCOE real for Tucson, AZ (¢/kWh) – without Investment Tax Credit (ITC)	11.83	11.47	10.61
SAM LCOE real for Tucson, AZ (¢/kWh) – ITC at 26% (DOE EERE 2021; SEIA 2021)	**9.44**	**9.16**	**8.50**
SAM LCOE real for Daggett, CA (¢¢/kWh) – without ITC	11.48	11.13	10.29
SAM LCOE real for Daggett, CA (¢/kWh) – ITC at 26% (DOE EERE 2021; SEIA 2021)	**9.16**	**8.89**	**8.25**

and Daggett, California (Location 2) are used to highlight the impact of location and direct normal irradiance (DNI). The labor values for the detailed manufacturing analysis are for Arizona. For the SAM analysis and scenarios, we assume that the installed solar field cost in California will be the same as in Arizona. This is not accurate, because labor rates in California are higher than those in Arizona. As highlighted, Arizona labor rates have been used for the manufacturing cost and construction analysis. The analysis in Table 4 includes Location 2 (Daggett, California), as Daggett has excellent DNI and weather conditions and so is used to highlight the impact of excellent DNI and the costs for a CSP plant in the various scenarios.

Table 4 shows the results of the SAM cases with the default, commercial, and advanced costs, assuming that both the remainder of the CSP plant and the financial assumptions stay the same. The default financials in SAM 2020.11.29 were used. As of 2021, the Investment Tax Credit (ITC), which is a key financial incentive for large solar projects, has been extended for commercial solar projects starting construction up to December 31, 2023 (DOE EERE 2021). The analysis included the 26% ITC benefit, assuming the CSP projects modeled in Table 4 start construction in 2021 or 2022 (SEIA 2021). After 2023, the ITC is currently expected to decrease to 10% (SEIA 2021). As seen in Table 4, the ITC at 26% benefit has a significant impact on the LCOE. For example, in Tucson, Arizona, in the default cost case, the LCOE drops by 20.2% with the ITC applied. We assumed that any CSP project starting construction in 2021 and 2022 would use the full ITC.

As shown in Table 4, the change in potential installed cost for the heliostat field of approximately 1.1 Mm^2 has a significant impact on the LCOE. At Location 1 (Tucson, Arizona), with the ITC applied, the reduction in heliostat field costs—from $\$140/m^2$ to $127/m^2$ and $96/m^2$ for the commercial and advanced cases, respectively—could lead to a reduction in LCOE of 3% and 10%, respectively. For Location 2 (Daggett, California), which has slightly higher DNI than Tucson, Arizona, changing the costs from the default $\$140/m^2$ for the heliostats to $\$127/m^2$ and $\$96/m^2$ results in almost the same LCOE reductions as Arizona.

The main output from the detailed bottom-up heliostat analysis is the published report "Cost Update: Commercial and Advanced Heliostat Collectors" (Kurup et al. 2022). The major results include the estimation of the commercial and advanced heliostat installed costs of $\$127/m^2$ and $\$96/m^2$, respectively, in 2020 dollars.

This detailed analysis has several potential uses and impacts. These include direct use in the 2022 ATB, where the $\$127/m^2$ installed heliostat field cost (found through the detailed analysis and confirmed with the industrial survey) was used to create the base cost or the starting point (NREL 2022). The detailed bottom-up heliostat analysis also fed into the DOE-funded Heliostat Consortium (HelioCon) report titled "Initial Heliostat Supply Chain Report" (Kurup, Akar, and Augustine 2022). Through the collaboration with industry, this type of key work adds to the global understanding of today's estimated cost, reduction opportunities, and potential future pathways to cost targets such as $\$50/m^2$ (DOE SETO 2021). This type of detailed analysis could be part of future reviews and road maps (Coventry and Pye 2014; Kolb et al. 2007).

CSP Cost Tracking

NREL's System Advisor Model (SAM) is a performance and financial model designed to facilitate decision-making for people involved in the renewable energy industry. SAM makes

performance predictions and cost of energy estimates for grid-connected power projects based on installation and operating costs and system design parameters that are specified as inputs to the model. Cost of energy predictions require the user to input capital and operating costs for the technology in question, and default values are provided with every SAM release. The default values are updated periodically based on published cost data in the literature and industry surveys of component costs. This task updates SAM CSP default cost values.

In previous years, NREL has solicited information on CSP costs and performance from CSP industry members using a questionnaire (Turchi and Boyd 2019). The survey questions cover the cost inputs for major components in the SAM CSP power tower, parabolic trough, and linear Fresnel systems. The questions ask the respondent to characterize the current value and give additional comments, and the survey also asks further questions about what the respondents were assuming when they gave their answer.

We attempted to solicit information from CSP industry members on cost inputs for SAM but did not have much success. Despite working with collaborators in Europe to increase the scope of our outreach, the response from industry was underwhelming. Out of 98 people contacted, only eight responded. There were seven individuals who responded to questions on the parabolic trough, eight for power towers, and one for linear Fresnel. Further, several respondents did not reply to a significant number of the questions. Although a couple of the questions had six or seven responses, most had only two to four responses. Also, although most responses were close to the default values already in SAM, one respondent's answers differed significantly from the rest and skewed the results. Due to these issues, we decided not to incorporate the responses from CSP industry into the updates for SAM CSP default cost values.

We did update the SAM CSP default values for the power tower heliostat field cost based on the bottom-up cost analyses described in the sections above. The CSP power tower "heliostat field cost" default value in SAM was updated from \$140/m^2 to \$127/m^2 (Kurup et al. 2022). The CSP parabolic trough "solar field" default value of \$150/m^2 was deemed close enough to the bottom-up analysis value of \$152/m^2 (Kurup, Glynn, and Akar 2020, 2021) to remain unchanged. The default values recommended for the CSP parabolic trough and power tower inputs in SAM 2021.12.21, along with the resulting LCOE, are shown in Table 5 and Table 6, respectively.

Table 5. Recommended Default Values for the 2021 SAM Parabolic Trough Model

SAM Cost Category	Default Value	Unit
Site Improvements	25	\$/m^2
Heliostat Field Cost	150	\$/m^2
HTF System	60	\$/m^2
Storage	62	\$/kWh_{th}
Power Cycle Cost	910	\$/kW_e
Balance of Plant Cost	90	\$/kW_e
Operation and Maintenance – Fixed Cost by Capacity	66	\$/kW-yr
Operation and Maintenance – Variable Cost by Generation	4	\$/MWh
LCOE (real)	**112**	**\$/MWh**

Table 6. Recommended Default Values for the 2021 SAM MSPT

SAM Cost Category	Current Default	Unit
Site Preparation	16	$/m^2
Heliostat Field	127	$/m^2
Power Cycle Cost	1,040	$/kW$_e$
Balance of Plant Cost	290	$/kW$_e$
TES Cost	22	$/kWh$_{th}$
Receiver Cost	85,191,944	$
Tower Cost	25,319,158	$
Operation and Maintenance – Fixed Cost by Capacity	66	$/kW-yr
Operation and Maintenance – Variable Cost by Generation	3.5	$/MWh
LCOE (real)	**84**	**$/MWh**

Task 2: Enhancements to SAM and Other CSP Modeling Tools

Task 2 consisted of two subtasks aimed at improving CSP models in SAM. The first subtask was a two-year effort to develop a cavity receiver model for use in SAM. The second subtask converted the dispatch optimization code in SAM's MSPT model for use in other models that include TES—the "Parabolic Trough – Physical" and "Parabolic Trough – Heat" models.

Cavity Receiver Model

The objective of this project was to develop code modifications for SolarPILOT and SolTrace that could be used to model incident solar flux on the surfaces of a cavity receiver. These modeling tools were then integrated with SAM's MSPT technology model to enable an annual simulation of the baseline cavity receiver model. SunShot's 90% annual average receiver efficiency target is a challenging metric for receivers that are planned to operate at 700°C and above. Some system designs, particularly with gas-phase HTFs and in smaller tower configurations, are exploring cavity receiver designs to realize improvements in optical and thermal efficiency. SAM previously did not include cavity receivers as an option, which limited NREL and DOE's ability to evaluate the potential benefits of these smaller-tower designs.

This project was done in partnership with the University of Wisconsin–Madison (UW–Madison) to formulate and develop the cavity receiver model. This work leverages previous cavity receiver research and modeling completed by UW–Madison's Solar Energy Laboratory (UWSEL).

We started by developing the methodology and models to calculate the incident flux on the surfaces of the baseline cavity receiver model. The cavity receiver geometry was based on the PS10 Solar Plant receiver design in Seville, Spain. The cavity consists of four panels oriented in a half octagon. The receiver panels are 12 m x 5.36 m with a 135° interior angle between each panel, as seen in Figure 13. The opening of the cavity receiver is 12 m x 14 m.

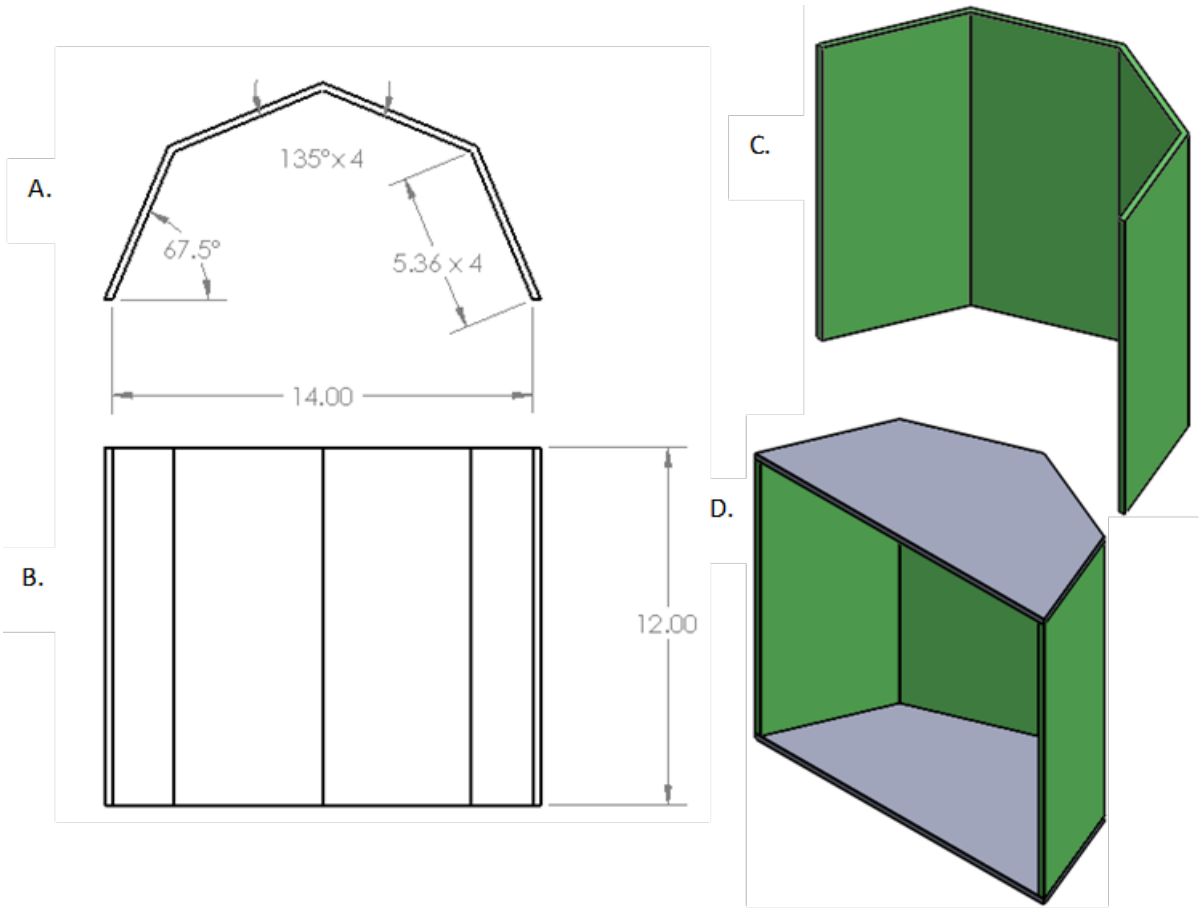

Figure 13. Cavity receiver dimensions. (A) Top view. (B) Front view. (C) Isometric view. (D) Isometric view with passive panels.

Next, we generated a MATLAB script to automate the creation of the baseline type cavity receiver given the required geometric parameter inputs. The geometric parameters that can be varied are receiver opening height, receiver opening width, number of panels, receiver span angle, upper lip height, and lower lip height. The code also generates an image of the cavity so that a visual check can be performed to ensure the cavity has been generated correctly.

Initial modeling assumed that the cavity active absorber surfaces were rectangular and could be discretized with a regular rectangular-element mesh according to the horizontal and vertical position on each surface. Passive surfaces—in particular the cavity ceiling and floor—are not easily discretized using a regular mesh, so instead, they were meshed using a mix of rectangular and irregular quadrilateral elements. The technique used to generate this mesh was found to be disadvantageous, both in terms of the relatively small number of elements and the surface geometries that can be accommodated.

Originally, quadrilateral elements were selected for the passive surface mesh to facilitate view factor calculations. Even with this approach, a Monte Carlo ray trace algorithm was ultimately used to calculate view factors between elements, and the process for characterizing the full receiver mesh was time-consuming. We revisited the quadrilateral mesh assumption and sought to determine whether an alternate approach using triangular elements could be employed.

Triangular elements are commonly used in finite-element modeling and meshing tools, and they can more easily accommodate a broad range of surface geometries.

We identified a relatively unheralded publication by Narayanaswamy (2015) that derives an analytic expression to calculate the view factor between two arbitrarily oriented polygonal surfaces. Historically, algorithms for calculating analytical view factors have been limited to particular simple surfaces (e.g., rectangles, triangles, circles) in special cases of orientation (perpendicular, adjacent, parallel, etc.), and each view factor calculation utilizes a different algorithm or lookup table. Therefore, a general algorithm for view factor between n-polygonal surfaces in arbitrary orientation represents a significant improvement over the state of the art, and it allows for analytical calculation of an object meshed with triangular elements. By way of comparison with the Monte Carlo approach with irregular quadrilateral elements, this promises to be orders of magnitude faster for a system with a comparable (or even greater) number of elements. In effect, the optical and radiative exchange model solves more quickly and more accurately now that these changes have been implemented.

We contacted the original author of the paper to obtain the relevant source code and tested it in MATLAB. It showed exact agreement with most known analytical view factors, and in fact identified errors in a small set of lookup-table-based view factors. The algorithm was adapted for use in the Engineering Equation Solver (EES) software and replaced many of the planar geometry view factor calculation models. Furthermore, we developed a triangular mesh algorithm based on publicly available procedures and tested the code in MATLAB (see Figure 14 for a sample cavity floor mesh).

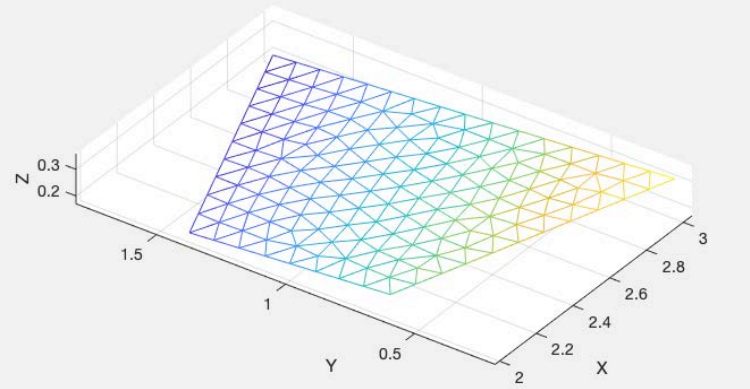

Figure 14. Sample mesh of the cavity floor using triangular elements.

The receiver thermal model considers the interaction between the fluid heat transfer and the tube inner wall, the conductivity to the tube outer wall, and the energy balance among (i) heat transferred from the outer wall to the working fluid, (ii) net flux, (iii) radiative thermal losses, and (iv) convective losses to ambient air. Surfaces are categorized as either *passive* or *active*, depending on whether they are comprised of tubes that absorb and transfer heat to a fluid. Passive surfaces are assumed to be fire brick or another high-temperature-resistant material that does not contain HTF. Examples of passive surfaces are the floor and ceiling panels and the front lip. Active surfaces typically have different optical properties from passive ones, and this affects the surface temperatures, radiative exchange, and overall thermal profile within the cavity. All surfaces participate in thermal losses to the environment either via convection or radiation, and

this behavior is directly modeled in our work using methods previously reported. We assume convective loss follows the Siebers and Kraabel model (Siebers and Kraabel 1984), and we neglect cavity tilt effects due to the high uncertainty inherent in the correlation.

We made several final changes to the MATLAB cavity thermal model to improve flexibility and accuracy. One outstanding issue was the routing of the fluid flow path across the panels. We implemented an approach that allows the user to specify the number of panels, number of "windings" in a flow path, whether the flow originates at the center of the cavity, and whether the flow enters at the top or bottom of the panel. With respect to fluid routing, the element size and number of tubes per fluid route are automatically determined based on the panel width and user-specified number of pipe windings. The user has control over the resolution of the discretization via a parameter specifying the number of elements per fluid pipe width (the default value is 1). The routing itself has several customization options—examples are shown in Figure 15—although this new procedure requires an even number of receiver panels because there are two symmetrical flow paths. The pipe wall conductivity is now a temperature dependent function that allows for the three material options: two steel alloys and an Inconel alloy. We also added temperature dependency for the HTF properties, assuming 60% $NaNO_3$-40% KNO_3 solar salt. This cavity performance model also is documented in a conference paper (Kerkhoff and Wagner 2021).

Next, we converted the improved cavity thermo-fluid model from MATLAB to SAM's C++ modeling framework. The conversion was a nontrivial task. Because the thermo-fluid model captures interactions between several discretized surfaces, MATLAB's built-in matrix routines and dense syntax are convenient for initial model development. Although C++ crucially offers a free platform, faster solution speeds, and integration with SAM's code base, adding all the matrix operations and receiver performance code to C++ was a tedious project. After some trial and error, we decided to implement the open-source C++ library Eigen to help with the code. Although Eigen does not provide a one-to-one conversion for MATLAB, it gives us validated code for matrix operations and, importantly, linear algebra. Validation between the platforms shows excellent agreement, indicating that the conversion accurately captures the functionality of the MATLAB code.

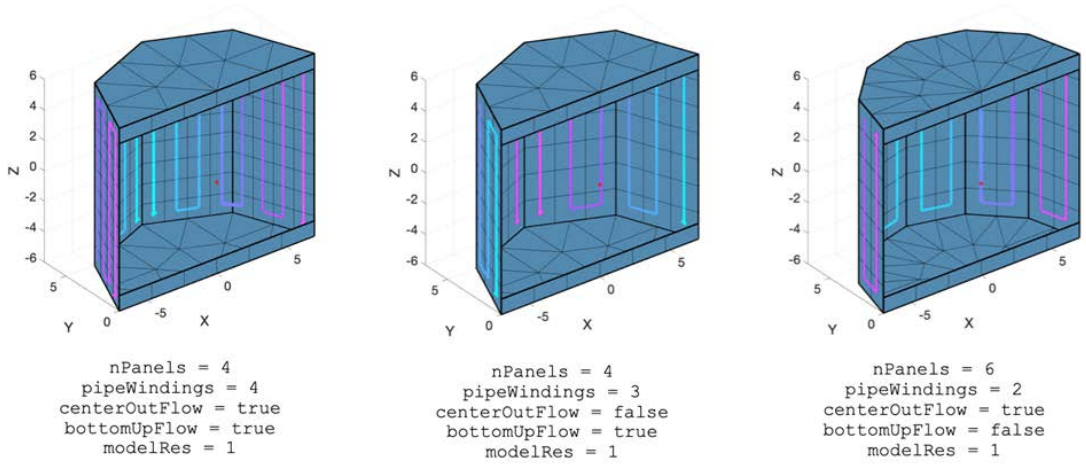

Figure 15. Fluid routing parameter impact.

The next task was the implementation of cavity flux modeling in SolarPILOT, which is an intermediate step on the path to full implementation in SAM. Cavity flux modeling requires consideration of the following steps:

1. The heliostat field layout must be established for a cavity receiver. As a template, we took the existing layout algorithm for flat-plate receivers, which are representative of the aperture geometry for cavity receivers.

2. Heliostat aimpoints must be determined. The aiming strategy seeks to minimize peak flux while maximizing total power delivered to the receiver. In practice, this means choosing aimpoints that encourage a relatively uniform distribution of flux (with greater flux in regions on the receiver where internal fluid temperature is lowest) while minimizing spillage loss.

3. After establishing flux aimpoints, the density of flux and performance of each heliostat must be simulated.

4. Results must be tabulated, plotted, and reported in the interface.

Figure 16 shows the result of a layout for a cavity receiver with an aperture of height 10 m and width 12 m, a power rating of 80 MW_{th}, and a tower height of 90 m. The overall layout approach mimics that of a flat plate, and the user can determine in SolarPILOT whether a downward tilt is present in the receiver. SAM currently enforces a vertically aligned aperture.

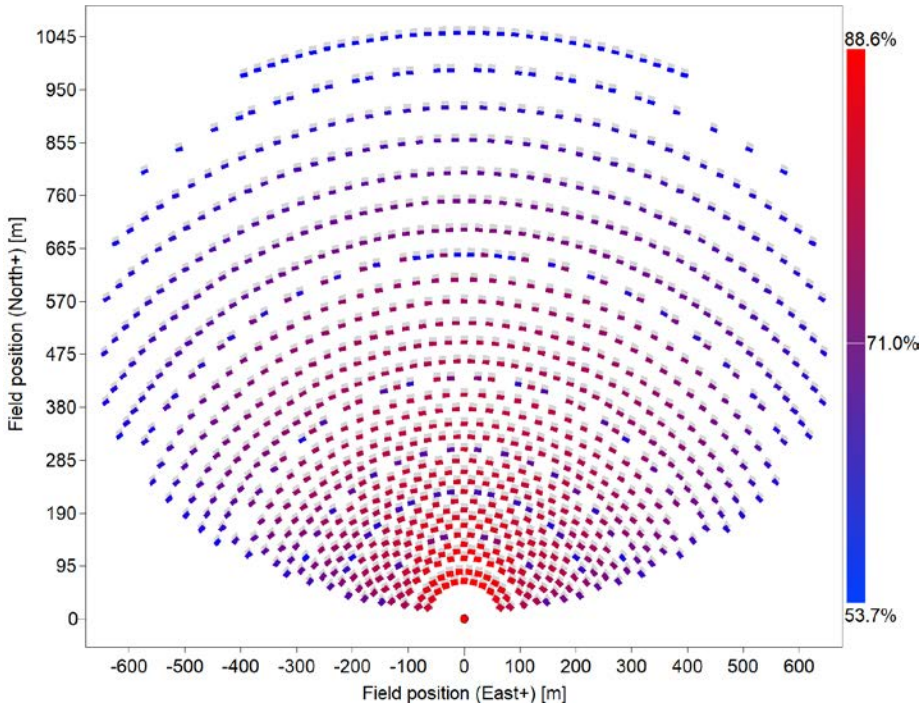

Figure 16. Cavity receiver field layout.

The aiming strategy uses the "image size aiming" to distribute flux over a virtual plane at the aperture, then "casts" the aimpoints back onto the absorber panels behind the aperture when determining the flux on the receiver. Figure 17 shows a SolarPILOT flux map for the cavity surfaces stitched together over the circumferential position. This plot demonstrates the ability of SolarPILOT to aim heliostats and calculate flux as a function of solar position. We reviewed flux maps at various solar positions and found that the maps sometimes had suboptimal flux distribution between two panels or within a single panel. To mitigate this, we average the entire flux onto a single flux value per panel in SAM. This is consistent with the external receiver approach and is adequate for first-order simulations in SAM. We attribute this suboptimal behavior to our aiming strategy, which is based on the flux profile at the aperture. The challenge of cavity receivers is that the flux should be evenly distributed on the panels at all relevant sun positions while simultaneously passing through the aperture. In turn, this requires a more elaborate aiming strategy and likely modifications to the field layout algorithm. We hope to improve cavity field aiming and layout methodologies in FY22.

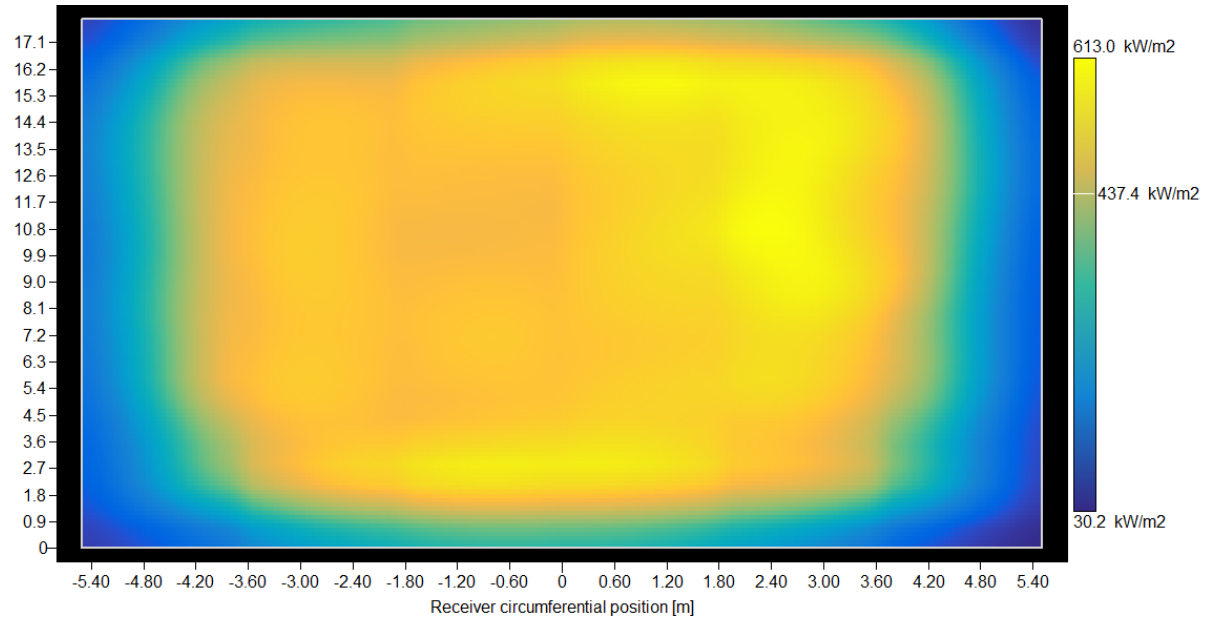

Figure 17. Flux aiming results that demonstrate the effect of multiple panels and completion of plotting capabilities.

We added the cavity receiver as a receiver option in the MSPT technology model, in addition to the existing external receiver. To give users the option to choose between the external and cavity options, we created a drop-down on the Tower and Receiver page and moved receiver-type-specific parameters to these individual pages. For example, both the external and cavity drop-down pages have unique inputs for receiver height, while the external receiver has an input for receiver diameter and the cavity has inputs for receiver width and span. Figure 18 shows the new drop-down pages.

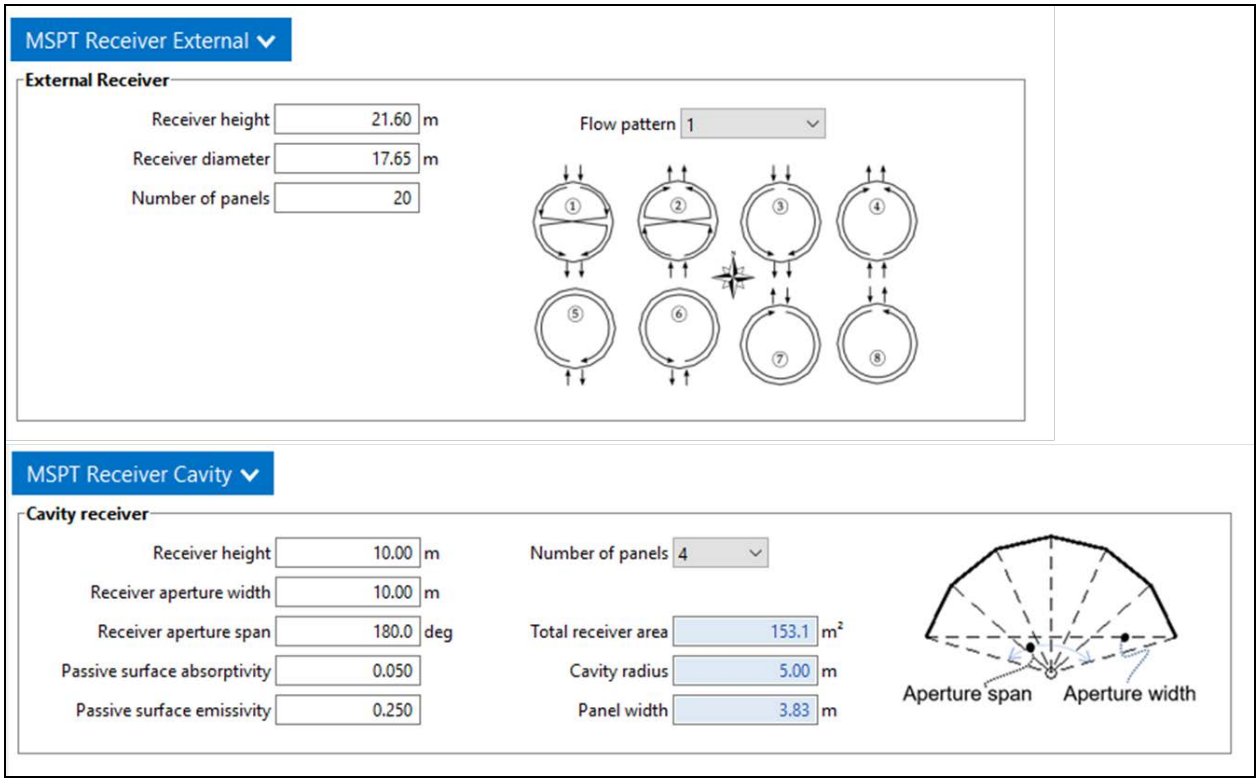

Figure 18. New external (top) and cavity (bottom) drop-down pages on the Tower and Receiver page.

Next, we connected the user interface to SolarPILOT's API to enable macros for the cavity receiver that (i) lay out the field for a fixed tower/receiver geometry and (ii) optimize the tower/receiver geometry and lay out the field. We also connected the underlying power tower simulation code to the same functionality so that users can elect to lay out the field or optimize the tower at the beginning of the annual simulation. Note that these capabilities already existed for the external receiver. Figure 19 shows the north field layout that the SolarPILOT optimization macro generates after changing to a cavity receiver. The macro does not require the user to modify the existing surround field, but it is sensitive to the tower height, receiver height, and receiver width guess values when the user makes a significant change to the receiver thermal rating.

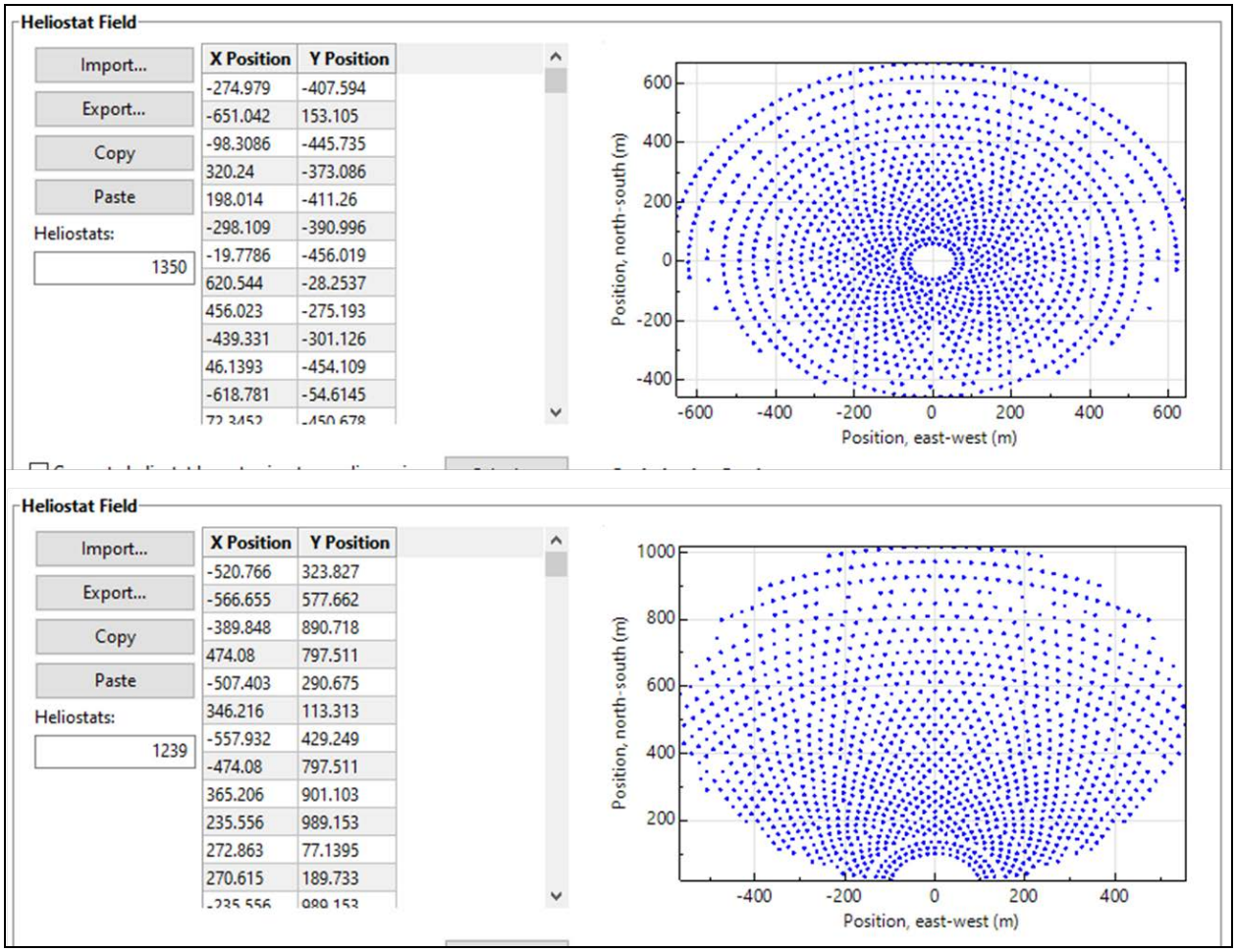

Figure 19. Comparison of external receiver field layout (top) and field generated by the SolarPILOT optimization macro after changing to a cavity receiver (bottom).

The model with all surfaces meshed was compared to the original MATLAB model for accuracy. The annual simulation of the test case for the cavity receiver (105 MW_{th} receiver, 6 panels, 2.4 solar multiple, 10 hrs TES) resulted in realistic calculated annual energy (91,105 MWh) and LCOE (10 ¢/kWh). Table 7 shows annual simulation results from modifying the cavity receiver and model parameters. We found that meshing the surfaces significantly increases the computational burden of the problem, because the model must calculate radiative exchange (both solar and thermal) between every combination of nodes in the receiver. The table shows that meshing all the surfaces results in around a 1% difference but incurs a significant simulation speed penalty. It also shows that when the receiver span is 1 degree (essentially a flat plate receiver), the performance decreases by around 2%. This is logical, because the absorber surfaces will have higher heat losses without the cavity floor and ceiling to shield them from the surroundings. The results also show that switching to more realistic passive surface properties has only a small influence on the performance. Given this trade-off, we are providing only the unmeshed option through the SAM user interface, while maintaining the meshed capability in the SSC code for advanced analyses and future code development (e.g., different cavity shapes).

Table 7. Cavity Receiver Annual Simulation Parametric Results

Cavity Receiver Parameters	% Difference	Simulation Duration
Default (no mesh, 6 panel, 180° span)	0% (default)	10 seconds
240° span	0.26%	10 seconds
90° span	-1.23%	10 seconds
1° span	-2.05%	10 seconds
All meshed	1.16%	>10 minutes
Receiver meshed	1.08%	270 seconds
Receiver meshed, 8 panel	1.20%	880 seconds
8 panel	0.52%	11 seconds
Solar spectrum reflectivity = 0.3 **Thermal spectrum emissivity = 0.5**	-0.20%	10 seconds

Dispatch Optimization in SAM

The value of all solar-thermal technologies depends critically on the ability to store energy and dispatch that energy when it is most valuable to the recipient application, be it grid electricity or industrial process heat. Understanding the temporal value of energy dispatch is challenging and makes it difficult for stakeholders to understand the true potential of CSP and solar process heat technologies. SAM's MSPT model includes a dispatch optimization algorithm that allows users to maximize revenue from the plant operations over the course of an annual simulation, given knowledge of hourly pricing signals. This task enabled dispatch optimization for the Parabolic Trough – Physical model.

Prior to development of the MSPT dispatch model, all CSP technology system models converged energy, mass, and plant control by coupling plant component models (e.g., solar field, power cycle) in a generalized successive substitution solver (our in-house solver is called TCS, a loose acronym denoting the *transient component simulation* purpose of the tool). Although this type of solver is relatively easy to configure and is an appropriate solver for some systems, it created challenges for CSP systems with TES. The primary issue is that the plant control occurs during iteration on the plant solution. Consequently, if the solution's preferred plant operating mode exceeds an operating constraint (e.g., sending all receiver HTF to TES with cycle off will overcharge TES), the solver struggles to correctly adapt the control strategy and converge the system. This problem is exacerbated by dispatch optimization, which may request that the cycle remain off when TES and solar field energy exists. Thus, for the MSPT dispatch model, we developed decoupled plant control and model convergence methods. The plant control method provides a hierarchy of preferred operating modes as a function of dispatch signal and component availability estimates. Then, for a selected operating mode, the convergence model runs. If convergence succeeds and component and system constraints are met, the timestep is complete. If convergence fails or constraints are exceeded, the plant controller chooses another operating mode and the process repeats. The new controller requires more rigid performance method definitions from component classes and expects clearly defined startup procedures, so the conversion of component models to the new solver is important and nontrivial. Conversion of the MSPT model to this framework showed a significant improvement in numerical convergence and the ability to more precisely control plant operations with a dispatch signal.

At the start of this task, only the MSPT and simplified Parabolic Trough – Heat models were in this new solver framework. The latter employs optional direct TES and a simple heat sink rather than a power cycle. As part of this task, the trough model in the new framework was fitted to the new two-tank TES model and the new Rankine power cycle model as the first step to offering this most common trough plant configuration as part of the new solver framework. Fitting of the model entailed creating a new compute module, merging component model parameters, updating module registry and makefiles, generalizing heat-sink-specific code in the trough model, melding equivalent input and output parameters, and implementing other miscellaneous edits to the code.

The new trough component model, which includes a significant amount of code from the older TCS model, contained several bugs brought over from the TCS model. These bugs were discovered after the creation of the new model and have since been fixed in the TCS model. Additionally, we needed to convert recently added features to the TCS model for detailed customization and analysis of balance of plants components and flow topology, including:

- Custom pipe sizing
- Steady-state model runs for design sizing
- Advanced, customizable interconnects
- Field recirculation through the cold storage tank
- Storage tanks serially connected between the field and power block in a direct storage configuration
- More accurate header pipe sizing algorithm.

Migrating these bug fixes and features to the new model and controller was not trivial, due to subtle changes in the calculations, flow control, and nomenclature from the TCS model along with the addition of sub-timestep operations. Updates were also made to the industrial process heat (IPH) model interface and user interface (UI) to make this model compatible with these new (power generating) trough model additions.

Dispatch optimization was fully integrated with the new trough model, including homogenizing the UI. This included adding the dispatch optimization parameters, adding other parameters for the new trough model, removing parameters for legacy submodels (i.e., fossil backup), and generally making the look and feel consistent with the molten salt tower and IPH models. Various minor bugs were found and fixed during this process, and improvements were made to the solver in order for it to converge on a few edge cases (e.g., almost full TES while the power cycle is operating at its maximum). For this project, we modified the controller to allow different TES tank configurations and operations and to make trough control amenable to the (tower) dispatch optimization interconnections.

The new controller is complex, and there is a corresponding higher potential number of unintended side effects associated with modifying it, so we created automated unit tests to catch unintended side effects during code development. These specific tests were needed to quality check the aforementioned trough model feature additions and to debug the storage tank draining, respectively. These tests provide a framework and example for other CSP technology components and models, and we are gradually adding tests.

Integration of the parabolic trough model with the new controller and the dispatch optimization routines was completed and verified. The new implementation of the parabolic trough model paired with the new controller provides estimates in good agreement with those from the old implementation and old controller. When dispatch optimization is not employed and when the model is run with the default inputs, the annual energy is within 1.2% and the power purchase agreement (PPA) price is within 0.08 ¢/kWh.

As mentioned above, the new controller more accurately balances the heat transfer fluid mass flow and energy transfer among the receiver field, TES, and power cycle subcomponents. This is enabled by its ability to subdivide the nominal timestep to execute discrete events, like startup and full charging or discharging of storage, in the exact amount of time needed or available. The old controller did not have this ability and therefore sometimes had to effectively execute multiple shorter events in parallel over the course of a full timestep. The approximated behavior at these times did not perfectly conserve mass and energy.

As an example of the errors that could arise with the old controller, this past year, an industry partner brought to our attention an extreme case while working on a project. The energy between the field and power cycle were no longer balancing after thermal storage became full, as shown by the red area in the left panel of Figure 20. At about 14:30, the produced field thermal power should have matched the power cycle input thermal power, as the thermal storage was full and there was nowhere else the produced power could go. The field thermal power dropped but remained too high. The new controller, whose behavior is shown in the right figure, does not have this issue.

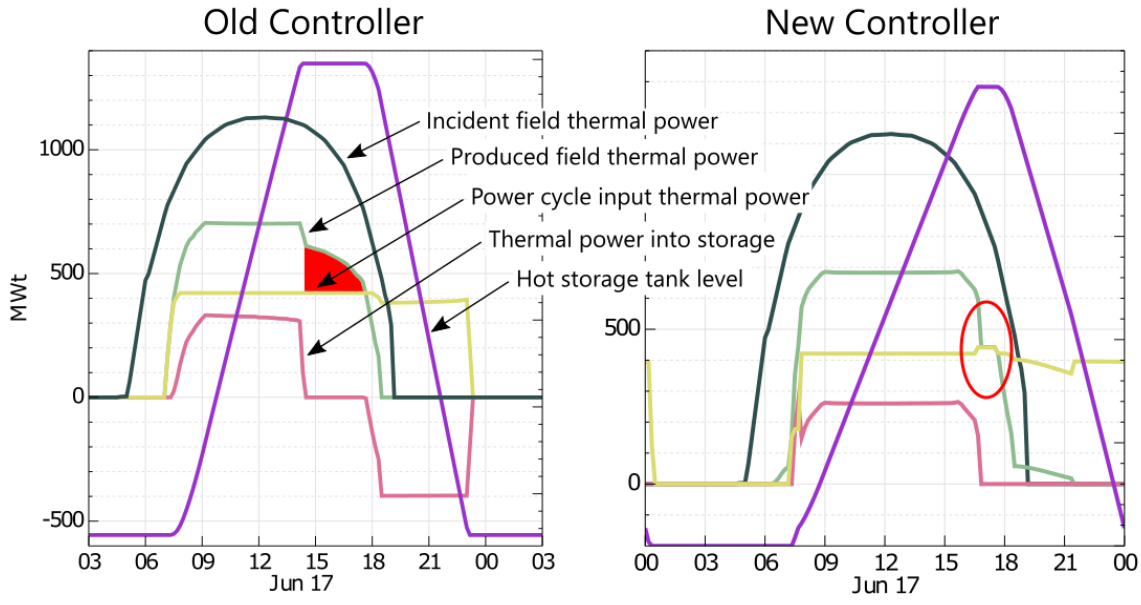

Figure 20. Behavior of the old controller (left) versus the new controller (right). The old controller did not conserve the power, with the trough field thermal power being overpredicted once thermal storage was filled. This issue is not seen with the new controller.

The trough model can now optimally discharge its storage based on a user-defined pricing signal and the forecasted weather. (The forecasted weather in SAM is currently a perfect forecast taken from the next 1–2 days in the weather file.) The same market scenarios and subsequent pricing signals as those used to test the MSPT dispatch optimization code were used for testing the trough model, with the scenarios presented in Figure 21.

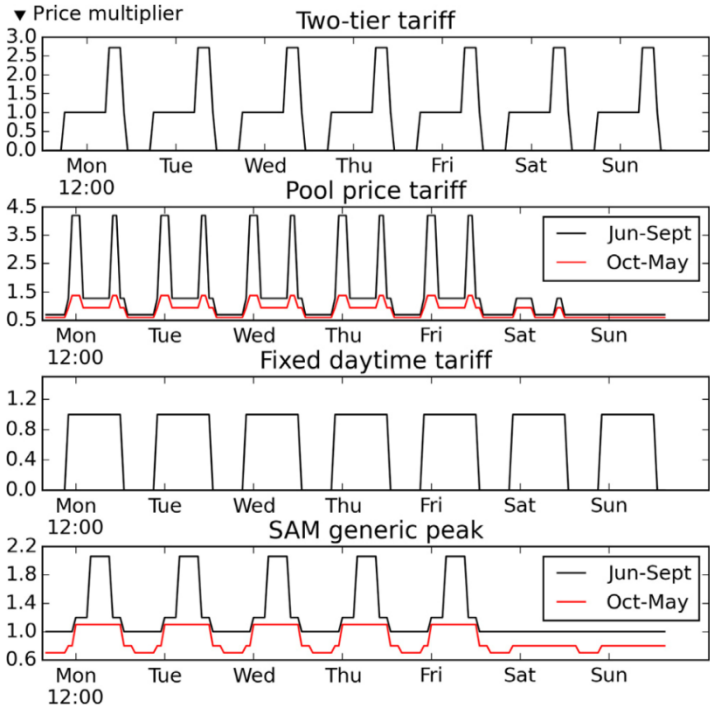

Figure 21. The market pricing scenarios used to test the trough dispatch optimization.

Presented by Guédez et al. (2015) and reproduced by Wagner et al. (2017)

Dispatch optimization reduced the PPA price in all cases for solar multiples between 0.8 and 3 and for hours of TES between 1 and 18 hours. For resulting PPA prices less than 10 ¢/kWh, dispatch optimization reduced the price by as much as 10.3%, with greater reductions seen at less economical prices. Comparing the PPA prices at their minimums resulted in price reductions of 1%–7%. This approached the project milestone goal, stated as a 10% reduction in LCOE versus the standard dispatch model. These minimum price comparisons are shown in Table 8, along with the respective solar multiples and hours of TES at the optimal solutions. NREL research in 2021 to integrate the Parabolic Trough – Physical model with the Hybrid Optimization and Performance Platform (HOPP) framework[4] leveraged this dispatch model and improved methods that the dispatch model uses to estimate trough performance. The resulting model should further improve the comparison between the heuristic and dispatch models.

[4] https://github.com/NREL/HOPP/tree/WB_CSP_dispatch_design

Table 8. Comparison of the Minimum PPA Prices Between the SAM Heuristic (H) and Optimized (O) Dispatch

Market Scenario	Solar Multiple		Hours TES		PPA Price	
	H	O	H	O	H	O
Two-tier	2.4	2	4	4	10.06	9.56
Pool price	2	2	4	4	10.79	9.99
Fixed daytime	2	1.6	4	1	14.10	14.01
SAM default	1.6	1.6	1	1	10.66	10.57

Dispatch optimization is set up to be used by the parabolic trough process heat model, but we are currently missing a price signal or financial incentive to dispatch against. NREL has a planned FY23 project to add a heat demand schedule and potentially a "price of heat" signal. Either or both of these signals will enable dispatch optimization in the process heat model. In the current process heat model developed in this project, block dispatch was added for specifying when the heat should be dispatched. Figure 22 shows block dispatch utilized with a peaking-plant schedule.

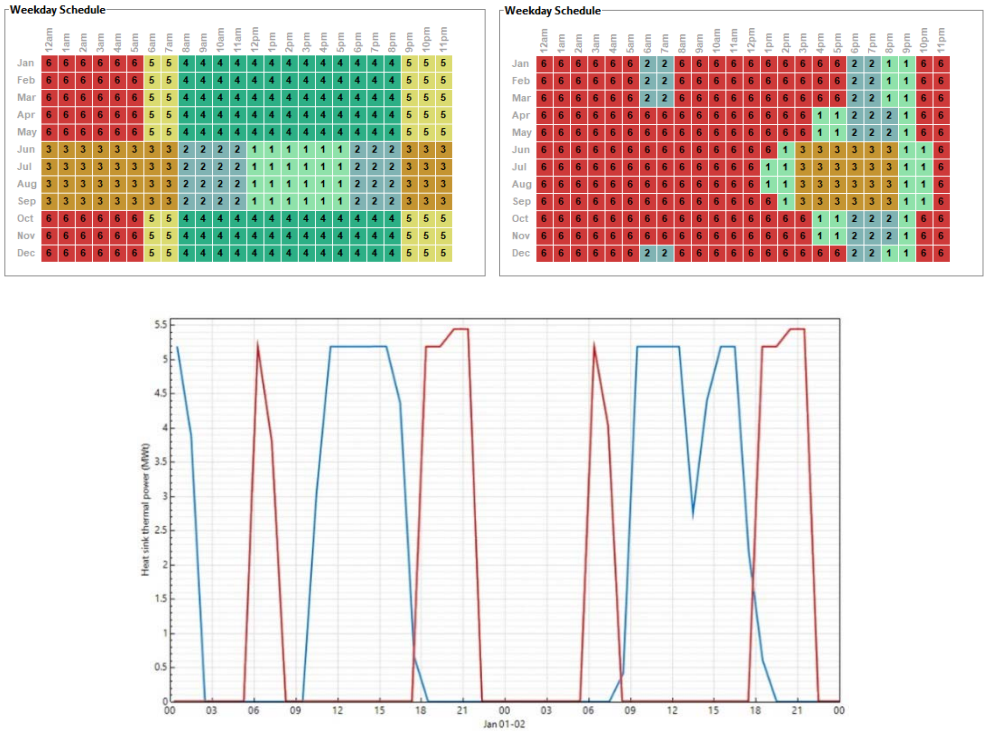

Figure 22. Two different dispatch schedules used with the new block dispatch option for the IPH trough model. The upper left schedule is the default SAM schedule, and the upper right schedule is characteristic of a peaker plant. The resultant heat sink thermal powers are shown in the bottom plot (blue for the default schedule and red for the peaker).

The parabolic trough code updates were fully integrated into SAM and were included in the SAM 2020.02.29 release. This included updated scripts for automatically converting older trough models in SAM to the new model, as well as new UIs for the trough power and process heat

models, with a sample shown in Figure 23. These new UIs, created earlier this year, are more consistent with the MSPT UI, and thus provide more familiarity and ease of use to the CSP community. They also include new inputs needed for the newly added dispatch optimization and block dispatch routines.

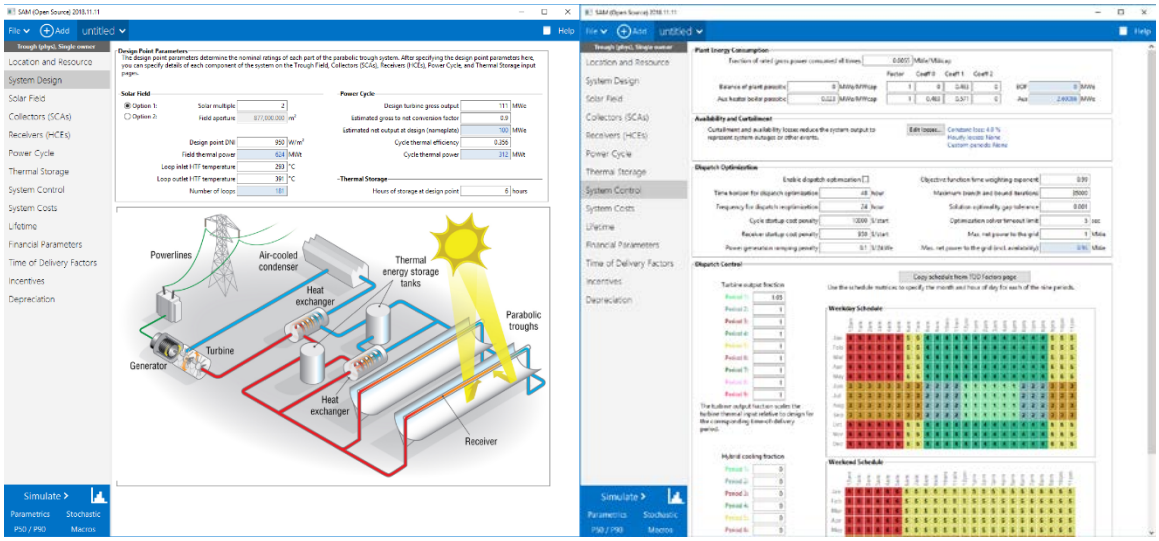

Figure 23. A sample of two new pages in the parabolic trough UI, created to be more consistent with the MSPT and IPH trough pages. These UI pages include new inputs needed for the new trough dispatch optimization and IPH block dispatch.

Task 3: International Engagement

NREL's Mark Mehos serves as the Task I operating agent in SolarPACES. This task addresses the design, testing, demonstration, evaluation, and application of CSP systems, and supports an international project database for commercial CSP systems as well as the development of guidelines for performance models, acceptance test procedures, and standards for CSP systems. The active international sector provides valuable markets for U.S. CSP developers and offers knowledge that can be applied to systems in the United States. Understanding international activity is essential to the health and relevance of the U.S. CSP industry as well as the viability of domestic CSP projects.

Mehos organized and attended SolarPACES Task I meetings annually and also participated in the kickoff and subsequent meetings of the SolarPACES Executive Committee Industry Advisory Board. He also organized and led plenary sessions at annual SolarPACES conferences. Additionally, in this role, Mehos led the merger of the CSP-guru international projects data set with the SolarPACES projects database to create the NREL/SolarPACES CSP database (https://solarpaces.nrel.gov/). This database lists CSP projects by country, project name, technology (power plant) type, and status. It includes an update completed by the Institute for Advanced Sustainability Studies (IASS) in Potsdam to their OpenCSP project located on the csp.guru platform. The update includes newly operating plants in Chile and China. The merger also included additional fields in the NREL/SolarPACES database, such as jobs (construction, operational) and financial data (normalized LCOE, specific plant costs, renumeration value, etc.).

Mehos organized and participated in the Task I meeting held in Casablanca, Morocco, commensurate with the 2018 SolarPACES symposium. The Task I meeting focused in part on introducing NREL's just awarded CSP Best Practices project and soliciting interest from the SolarPACES community to participate in this activity. The Task I meeting also discussed recent work on guidelines for CSP performance modeling. The guidelines have been condensed into a checklist to make the information more available, to allow specific models to be compared to the guidelines, and to provide quantitative measures of compliance. The checklist was tested on two CSP models within SAM and is now available on the SolarPACES website. A Task I meeting was subsequently held in Daegu, South Korea, the last face-to-face meeting to be held prior to the onset of the COVID pandemic. The meeting highlighted intermediate outcomes of the Best Practices study initiated the prior year and yielded additional comments and input prior to final production of the report in early 2020.

Task 4: Supercritical CO_2 Power Cycle Modeling

Task 4 consisted of two subtasks, each focused on improving the representation of sCO_2 power cycles in Gen3 CSP projects. The first subtask assessed the use of cascaded latent-heat TES for use with the sCO_2 recompression cycle to increase efficiency. The second subtask worked to improve design and off-design models for the sCO_2 cycle in SAM to capture more realistic operating conditions for the recompression and partial cooling sCO_2 cycle models.

Latent-Heat Thermal Energy Storage for Recompression sCO_2 Cycle

The sCO_2 recompression cycle is often proposed for CSP applications because of its combination of simplicity and efficiency. However, it is characterized by a relatively narrow HTF temperature difference, which increases the cost of sensible-heat storage for CSP systems. One solution for CSP applications to take advantage of the better cycle efficiencies offered by the recompression cycle is to replace sensible-heat storage with latent-heat storage. In this scenario, the temperature difference can be close to 100 K, and latent-heat storage units can be cascaded to supply heat over the temperature range. The use of latent-heat TES also opens the possibility of implementing cycle reheat, which can improve cycle efficiency without increasing turbine inlet temperature. This task analyzed the techno-economic feasibility of latent-heat storage integration with an MSPT and the sCO_2 cycle.

Latent-heat storage charges and discharges at constant temperature. If only one phase change material (PCM) is used for charging a sensible HTF, then either the HTF temperature difference would be very low (which increases the HTF mass flow rate and the receiver loss) or the PCM would need to be at a lower temperature (which decreases the power cycle efficiency during discharge). However, if cascaded PCM is used, an HTF temperature difference of greater than 100°C can easily be achieved.

In this study, NREL identified practical ranges for important latent-heat storage design parameters, like the receiver-side HTF approach temperature, the primary heat exchanger (PHX)-side HTF approach temperature, and the number of cascaded stages. Then, NREL configured SAM's MSPT model to approximate a system employing latent-heat storage based on the identified ranges for the design parameters. We simulated the latent-heat storage case and compared it to the baseline case employing two-tank sensible-heat storage. The latent-heat storage case had lower annual energy generation because it requires a greater temperature difference between the turbine inlet and the receiver outlet than a direct storage system. Thus, NREL calculated the latent-heat storage cost necessary to achieve a break-even LCOE with the baseline two-tank storage system LCOE. Finally, we identified the systems with the most potential for latent-heat storage and discussed the feasibility of achieving the break-even cost targets. Table 9 lists the various available economical PCMs in the temperature range of 650°–450°C. The PCM costs are taken from various internet sources and represent 2019 prices. It should be noted that costs will vary with market conditions and are more representative of relative differences between materials than actual prices.

Table 9. Phase Change Material Options Available for Thermal Energy Storage

PCM Name				Mass Fraction				Melting Point[1,2]	Latent Heat[1,2]	Density[1,2]	Cost	
1	2	3	4	1	2	3	4	°C	kJ/kg	m^3/kg	$/kg	$/kWh$_{th}$
$CeCl_2$				1.00				645	121	3990	0.40	11.9
$Sr(NO_3)_2$				1.00				645	231	299	1.00	15.6
NaCl	Na_2CO_3			0.40	0.60			632	165	2386	0.14	3.1
KCl	K_2CO_3			0.47	0.53			623	202	2256	0.48	8.6
NaCl	NaBr	Na_2MoO_4		0.39	0.23	0.39		612	168	3025	2.79	59.9
$Ba(NO_3)_2$				1.00				594	209	3240	0.60	10.3
NaCl	Na_2CO_3	KCl		0.34	0.31	0.35		573	165	2215	0.12	2.7
$Ca(NO_3)_2$				1.00				560	145	2500	0.20	5.0
KCl	$BaCl_2$	$CaCl_2$		0.24	0.47	0.29		551	219	2913	0.31	5.1
KCl	NaCl	$BaCl_2$		0.28	0.19	0.53		542	221	3011	0.31	5.0
$MgCl_2$	$SrCl_2$			0.37	0.63			535	239	2780	0.45	6.7
NaCl	NaBr	Na_2MoO_4		0.05	0.40	0.55		525	215	3471	4.10	68.7
KCl	NaCl	$CaCl_2$		0.05	0.29	0.66		504	279	2144	0.35	4.6
NaCl	$CaCl_2$			0.33	0.67			500	239	2153	0.35	5.3
$CaCl_2$	NaCl			0.69	0.31			495	233	2153	0.36	5.6
KCl	$CaCl_2$	$MgCl_2$		0.25	0.27	0.48		487	342	2189	0.21	2.2
$BaCl_2$	$CaCl_2$	KCl	NaCl	0.21	0.27	0.35	0.17	479	217	2456	0.20	3.3
$BaCl_2$	$CaCl_2$	$MgCl_2$	NaCl	0.17	0.55	0.16	0.11	475	248	2472	0.31	4.5
KCl	$MgCl_2$			0.31	0.69			470	388	2216	0.11	1.0
$CaCl_2$	KCl	NaCl		0.65	0.06	0.29		465	245	2142	0.35	5.1
$CaCl_2$	KCl	$MgCl_2$	NaCl	0.55	0.02	0.10	0.33	460	245	2167	0.31	4.5
NaCl	$MgCl_2$			0.48	0.52			450	430	2243	0.08	0.7
NaCl	$MgCl_2$			0.56	0.44			442	325	2230	0.08	0.9
KCl	$MgCl_2$			0.61	0.39			435	351	2113	0.11	1.2
KCl	$ZnCl_2$			0.54	0.46			432	218	2408	0.62	10.2
NaCl	$MgCl_2$			0.56	0.44			430	320	2230	0.08	0.87

[1](Kenisarin 2010), [2](Yaokawa, Oikawa, and Anzai 2007)

Figure 24 shows an example of cascaded PCM integrated with a sensible-heat CSP receiver and recompression cycle. A portion of hot HTF coming out from the receiver flows into the PHX and gets cooled from 650°C ($T_{HTF\ hot}$) to 500°C ($T_{HTF\ cold\ 1}$). The sCO_2 gets heated up to 630°C from 480°C in the PHX. The remaining hot HTF flows into the cascaded PCM and charges it. The HTF exits the cascaded PCM at around 540°C ($T_{HTF\ cold\ 2}$) and mixes with the HTF leaving the PHX before returning to the receiver. During the night, the cold HTF flows into the cascade PCM, gets heated up, and then flows back into the PHX. The HTF temperature rises from 450°C to 600°C, and the sCO_2 gets charged from 430°C to 580°C.

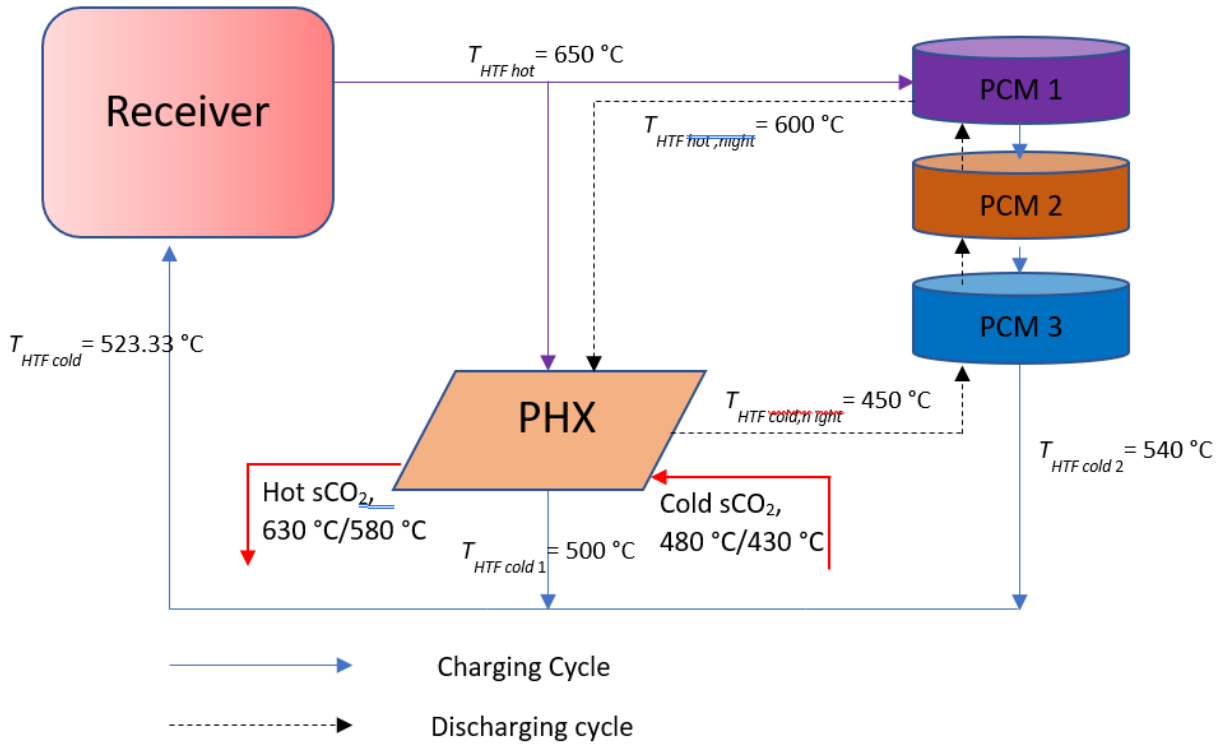

Figure 24. Schematic for phase change material storage integrated with CSP.

At the design point, let the solar multiple for the system be *SM*. The temperature of the HTF entering the receiver, used in SAM annual simulations, can be calculated as:

$$T_{HTF\ cold} = \frac{T_{HTF\ cold1} + (SM - 1)T_{HTF\ cold\ 2}}{SM} \quad (1)$$

Due to the reduction in the HTF operating temperature at night, the power cycle efficiency at night, η_{night}, will be lower than the power cycle efficiency during the day, η_{day}. The design-point efficiency, η_{design}, of the power cycle, used in SAM annual simulations, is defined as:

$$\eta_{design} = \frac{\eta_{day} + (SM - 1)\eta_{night}}{SM} \quad (2)$$

The aim of the present work is to calculate the break-even price for the cascaded PCM storage, which gives the same LCOE as two-tank sensible-heat storage. To calculate the break-even price for the cascaded PCM storage, we follow the following steps:

1. For a given cycle configuration, calculate the cycle efficiency and $\Delta T_{PHX,\ 2\text{-}tank}$ for the HTF.
2. Calculate the cost of two-tank TES. Run SAM for the two-tank baseline and calculate the baseline LCOE.
3. Decide number of cascading steps (number of PCM storage).
4. Assume $\Delta T_{HTF,\ PCM}$ temperature drop in the HTF flowing through the cascaded PCM.
5. Let the minimum temperature driving force between the HTF and the PCM be $\Delta T_{pinch,PCM}$.
6. Calculate the heat transfer taking place in each PCM while satisfying steps 3 and 4.
7. Calculate the temperature at which salt is produced during PCM discharging.
8. Calculate the reduction in cycle efficiency due to reduced salt temperature.
9. Using Eq (1) and Eq (2), calculate the $T_{HTF\ cold}$ and η_{design}.
10. Calculate the cost of storage for which the LCOE is same as the baseline LCOE calculated in step 2.
11. Repeat for a different value of $\Delta T_{HTF,\ PCM}$.

For a base case of a recuperative recompression cycle with a maximum operating HTF temperature of 650°C, $\Delta T_{PHX,\ 2\text{-}tank}$ = 156°C, η = 0.472, and storage cost = 39 \$/kWh$_{th}$ for two-tank sensible-heat storage for 10 hours, the LCOE for Daggett, California, comes out to be 10.9 ¢/kWh$_e$ with a 57.3% capacity factor. Note that these parameters are preliminary values used to show the PCM design process and break-even analysis. More detailed analysis later in this subsection provides updated values for some of these parameters.

Table 10. Input Parameters for Base Case Recuperative Recompression Cycle Using Cascaded PCM TES

Parameters	Values
Cycle design power	115 MW$_e$
Maximum HTF operating temperature	650°C
$\eta_{650°C}$	47.2 %
$\eta_{570°C}$	45.75 %
$\Delta T_{PHX,\ 2\text{-}tank}$	156°C
$\Delta T_{pinch,PCM}$	5°C
Number of PCM stages	3

Table 10 shows the input parameters for the cascaded PCM TES CSP power system, while Figure 25 shows a temperature and heat plot for three-stage PCM. The $\Delta T_{HTF,\,PCM}$ is assumed to be 110°C. PCM 1 is KCl (0.47)-K_2CO_3 (0.53) with a melting temperature of 623°C. PCM 2 is $Ba(NO_3)_2$ with 594°C melting temperature. PCM 3 is $MgCl_2$ (0.37)-$StCl_2$ (0.63) with 535°C melting temperature. The heat ratio for PCM1:PCM2:PCM3 is 0.2:0.26:0.54. The HTF flows back to the receiver at 540°C. During discharging, the HTF temperature increases from 446.3°C to 602.32°C. During the night, the system efficiency decreases to 46.3%. Using Eq (2), the design-point efficiency for the power cycle comes out to 46.7%, and using Eq (1), the cold HTF temperature comes out to 520.8°C. The storage cost to meet the baseline storage cost of 10.9 ¢/kWh_e is 29.4 \$/kWh_{th}. Using the PCM cost listed in Table 9, the PCM cost comes out to 9.3 \$/kWh_{th}, but it must be noted that the cost does not include the heat exchanger cost for PCM storage.

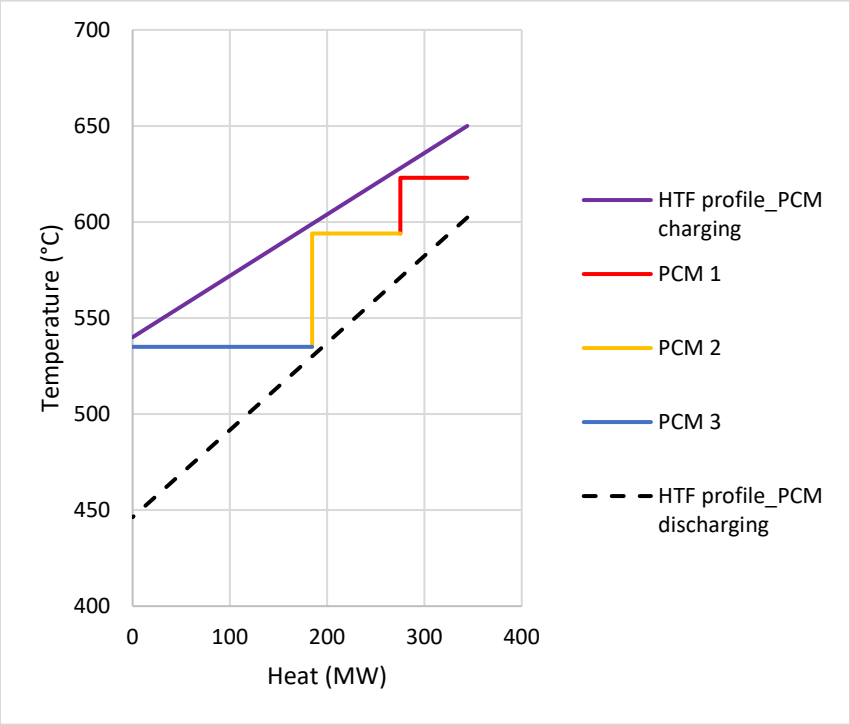

Figure 25. Temperature-heat diagram for three-stage PCM with $\Delta T_{HTF,\,PCM}$ = 110°C.

If the $\Delta T_{HTF,\,PCM}$ is increased to 123°C, the HTF can only be heated to 590.3°C during discharging (see Figure 26) and the cycle efficiency decreases slightly to 46.5%. Because of the increase in the $\Delta T_{HTF,\,PCM}$, the mass flow rate of HTF decreases. As such, the receiver performance improves and the pumping power deceases. The net result is a design more favorable to PCM than the 110°C, so the break-even price for the storage cost increases to **31 \$/kWh_{th}**. The PCMs used are KCl (0.47)-K_2CO_3 (0.53) at 623°C, NaCl (0.34)-Na_2CO_3 (0.31)-KCl (0.35) at 573°C, and KCl (0.05)-NaCl (0.29)-$CaCl_2$ (0.66) at 504°C. Using Table 9, the PCM cost comes out to be 3.7 \$/kWh_{th}, which is 60% cheaper than the set of PCMs mentioned above. Note that this cost does not include the heat exchanger cost for PCM storage.

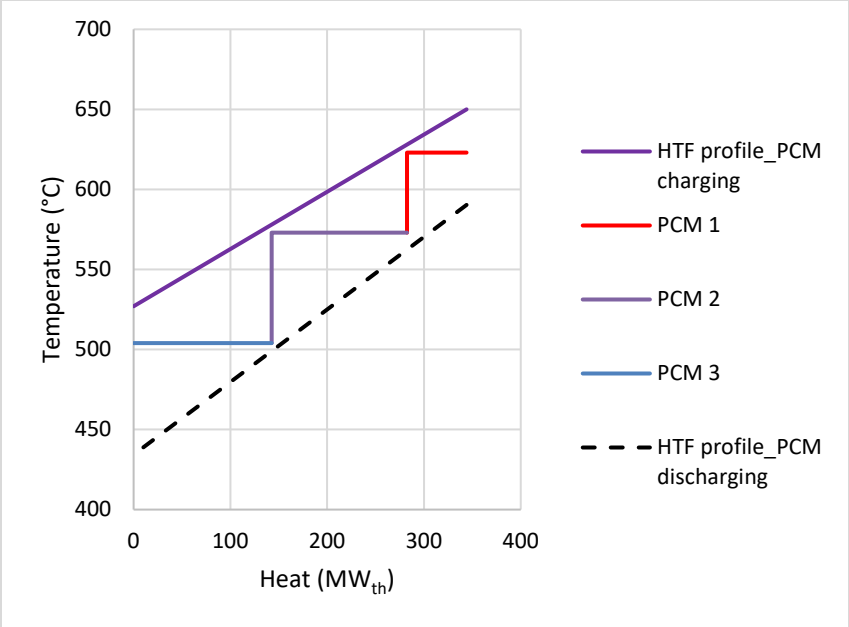

Figure 26. Temperature-heat diagram for three-stage PCM with $\Delta T_{HTF,\,PCM}$ = 123°C.

We generalized the approach to evaluating cascaded PCM TES for any number of PCM stages using the principle of process integration. Based on the number of PCM stages used, we calculated the technical optimal operating temperature (not considering cost) for each PCM. The PCM temperature calculated on this basis would be an ideal solution. For actual operating conditions, the PCM should be selected in such a way that its melting point is close to the actual operating temperature. For optimal system design, the total number of pinch points should be 2*N*, where *N* is the number of PCM stages. To pinch all the PCM stages, an iterative procedure needs to be carried out:

1. Specify the number of PCM stages (*N*), the temperature drop for the molten salt in the primary heat exchanger (ΔT_{PHX}), the HTF temperature from the receiver, and the minimum pinch temperature (ΔT_{pinch}).

2. Assume maximum HTF temperature during PCM discharge ($T_{HTF,\,D,\,out}$).

3. Assume the temperature drop in the PHX remains constant during charge and discharge (ΔT_{PHX}).

4. Calculate the temperature at which the molten salt enters the PCM during the discharge cycle as:

$$T_{HTF,D,in} = T_{HTF,D,out} - \Delta T_{PHX}$$

5. From steps 2 and 4, the PCM discharge cycle can be drawn as shown in Figure 27 below. For point 1 to be pinched, the melting point of PCM 1 should be:

$$T_{PCM1} = T_{HTF,D,in} + \Delta T_{pinch}$$

6. Guess the PCM operating temperature for other effects.

7. For an optimal solution, the PCM curve must be pinched at its edges (see Figure 27). If yes, stop; if no, update step 6 and repeat.

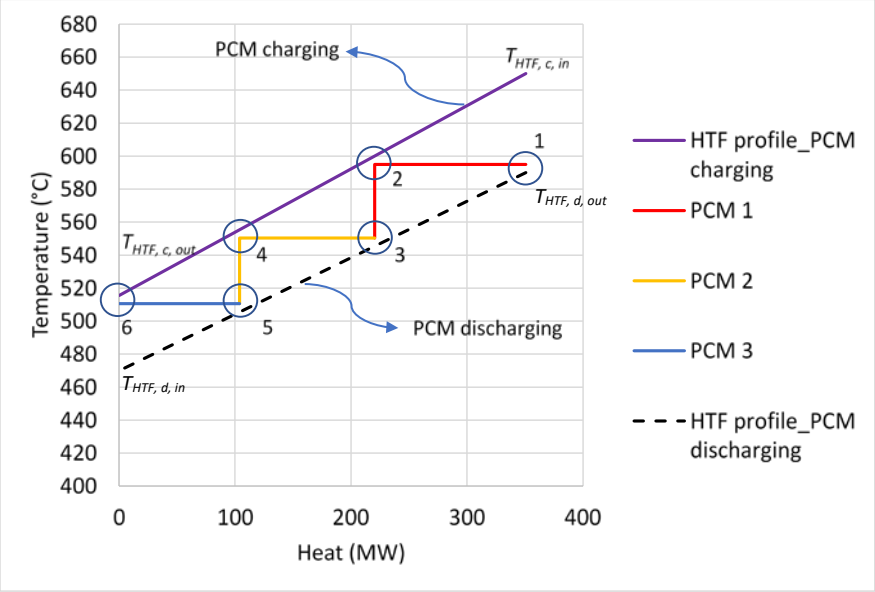

Figure 27. Optimal design of PCM during charging and discharging. PCM gets pinched at all its edges (2x3).

It is interesting to note that if the system is optimally designed for a given value of maximum HTF temperature during PCM discharge and temperature drop in the PHX, then the PCM will be pinched at all its edges. This optimal solution gives a maximum temperature drop for HTF during PCM charging, which will minimize the HTF flow rate from the receiver (i.e., reduce pumping power) and reduce the temperature of the HTF flowing back to the receiver (i.e., increase receiver efficiency).

2. Consideration of Different Power Cycles

Next, we performed the analysis using several power cycle options:

1. Recompression cycle
2. Recompression cycle with reheat cycle
3. Simple recuperative cycle
4. Partial cool cycle.

The design parameters for different power cycle options are shown in Table 11 with two-tank molten salt storage. The design parameters for the recompression cycle, simple cycle, and partial cool cycle are taken from (Neises and Turchi 2019). For the reheat cycle, it is assumed that the power cycle efficiency can be increased by 1%, and ΔT_{PHX} is assumed to be 120°C. The storage

cost is inversely proportional to the ΔT_{PHX}, so the two-tank storage cost for the reheat cycle comes out to 45 $/kWh$_{th}$.

Table 11. Design Parameters for Different Power Cycle Options Considered

Parameters	Recompression Cycle	Simple Cycle	Partial Cool Cycle	Reheat Cycle
Efficiency	46%	43%	46%	47%
$T_{HTF, in}$ (°C)	650	650	650	650
$T_{HTF, out}$ (°C)	490	454	431	530
ΔT_{PHX} (°C)	160	196	219	120
Power block cost ($/kWh$_e$)	1,415	1,281	1,410	1,415
Two-tank storage cost ($/kWh$_{th}$)	35	29	27	45

Recompression Cycle

HTF Temperature Drop

Figure 28(a) shows the variation in HTF temperature drop during PCM charging with maximum HTF temperature during discharge. For a maximum HTF temperature of 630°C during PCM discharge, the discharge cycle line moves closer to the charging cycle line (Figure 27). This means that the temperature drop during the charging cycle will be reduced, as the maximum (inlet) HTF temperature for PCM charging is fixed at 650°C. The HTF temperature drops are only 76°C, 98°C, and 113°C for three, four, and five PCMs, respectively, as compared to 160°C for the base case recuperative cycle. However, at 590°C, the HTF temperature drops increase to 155°C, 175°C, and 187°C for three, four, and five PCMs, respectively.

The net HTF charge-discharge temperature drop is a function of the temperature drop in the PCM and the temperature drop in the PHX. Because the PHX temperature drop remains constant, the net temperature drop follows a similar trajectory to the HTF temperature drop in the PCM (Figure 28(b)).

Receiver Efficiency

Figure 28(c) shows the variation in receiver average annual efficiency. As the HTF maximum discharge temperature is increased, the net HTF temperature drop decreases, leading to an increase in the HTF temperature flowing back to the receiver. This results in reduced receiver efficiency. The receiver efficiency varies from 85.3% to 84.95% with PCM. For the baseline case, the annual receiver efficiency is 85.1%.

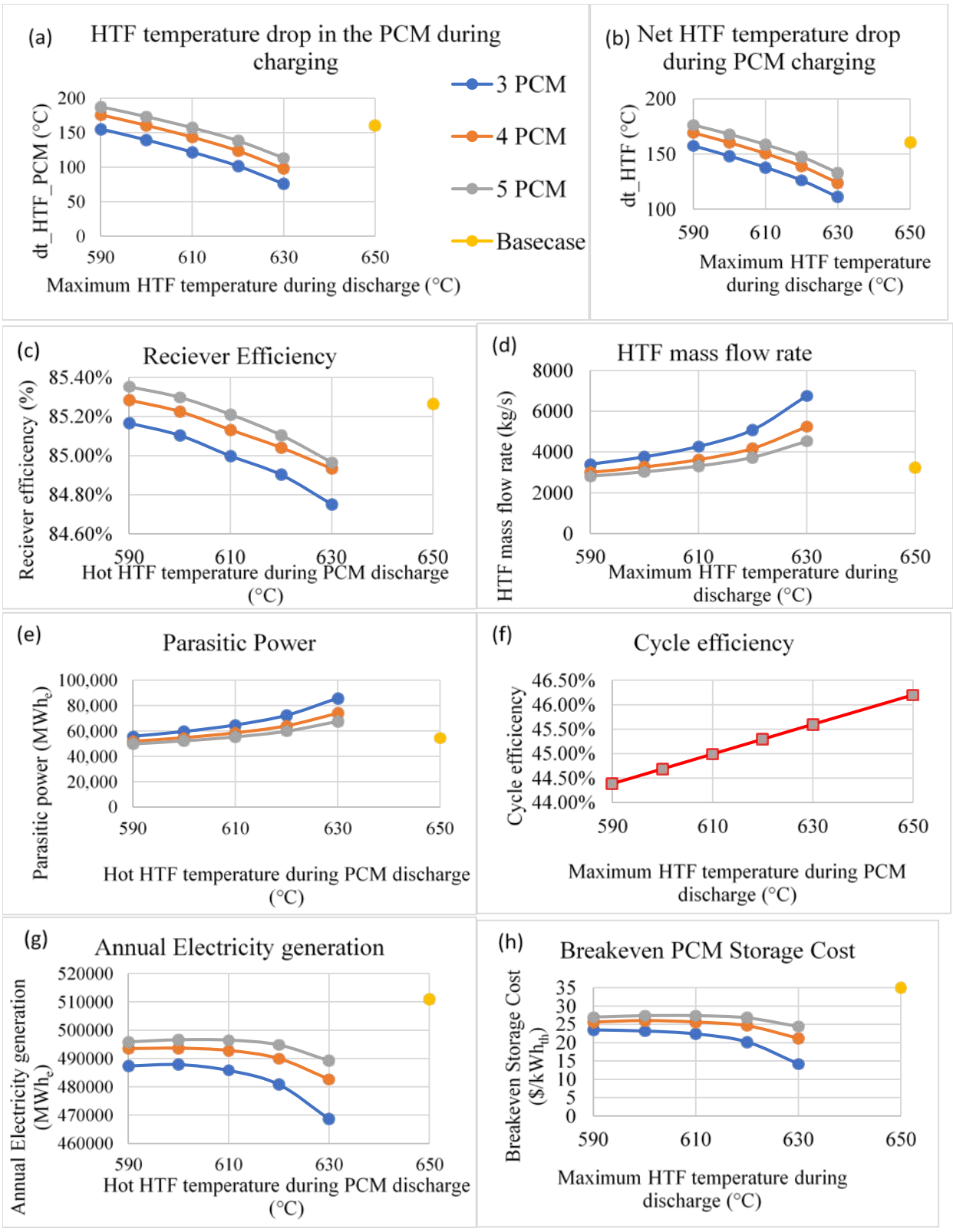

Figure 28. Variation in system performance parameters with maximum HTF temperature during discharge for the recompression cycle.

HTF Mass Flow Rate

The HTF mass flow rate is inversely proportional to the net HTF temperature drop (Figure 28(d)). For a maximum HTF temperature during discharge greater than 610°C, the HTF mass flow rate is significantly higher than the base case mass flow rate of 3,250 kg/sec. Higher mass flow rate will increase the receiver HTF parasitic pumping power.

Parasitic Power

Figure 28(e) shows the variation in annual parasitic power. For a maximum HTF temperature during discharge greater than 610°C, the HTF mass flow rate required increases, which increases the pumping parasitic. At 630°C, the parasitic load for the power plant is 57.1%, 35.4%, and 23.5% greater than the base case parasitic for three, four, and five PCMs, respectively. The parasitic power here includes TES HTF pumping, receiver HTF pumping, condenser pumping, etc. At 590°C for three PCMs, the TES parasitic is 10% higher, and for four and five PCMs, it is 5% or 9% lower than the base case parasitic, respectively.

Annual Electricity Generation

The annual electricity generation is a function of power cycle efficiency and parasitic load. With an increasein power cycle HTF operating temperature, the power cycle efficiency increases (second law of thermodynamics), as shown in Figure 28(f). However, Figure 28(e) shows that parasitic loads increase with temperature. While efficiency increases linearly, parasitic losses increase as the temperature rises. For temperatures greater than 610°C, the annual electricity generation reduces drastically. For four and five PCMs, the optimal HTF temperature during discharge is 610°C, and for three PCMs, it is 600°C (see Figure 28(g)).

Break-Even Storage Cost

Figure 28(h) shows the variation in the PCM break-even storage cost. For the base case recompression cycle, the storage cost is 35 \$/kWh$_e$, resulting in an LCOE of 11.91 ¢/kWh$_e$. For higher operating HTF temperatures (>610°C), the CSP performance reduces drastically, which means that the cost of PCM has to be significantly lower to reach an LCOE of 11.91 ¢/kWh$_e$. The maximum break-even storage cost for a three-stage PCM system is 23.5 \$/kWh$_{th}$ at 590°C. For a four-stage PCM system, it is 26 \$/kWh$_{th}$ at 600°C, and for a five-stage PCM system, it is 27.4 \$/kWh$_{th}$ at 610°C.

Recompression Reheat Cycle

We used a similar analysis for the reheat cycle. The design parameters for the reheat cycle are shown in Table 11. With the reheat cycle, the efficiency of the power plant increases to 47.2% and the net temperature of the heat addition from HTF to sCO_2 can be increased. This results in a net reduction in HTF temperature drop across the PHX to 120°C. The lower temperature difference for the PHX significantly increases the baseline two-tank storage cost to 45 \$/m^2. For the base case, the LCOE for the reheat cycle with two-tank energy storage is 12.68 ¢/kWh$_e$.

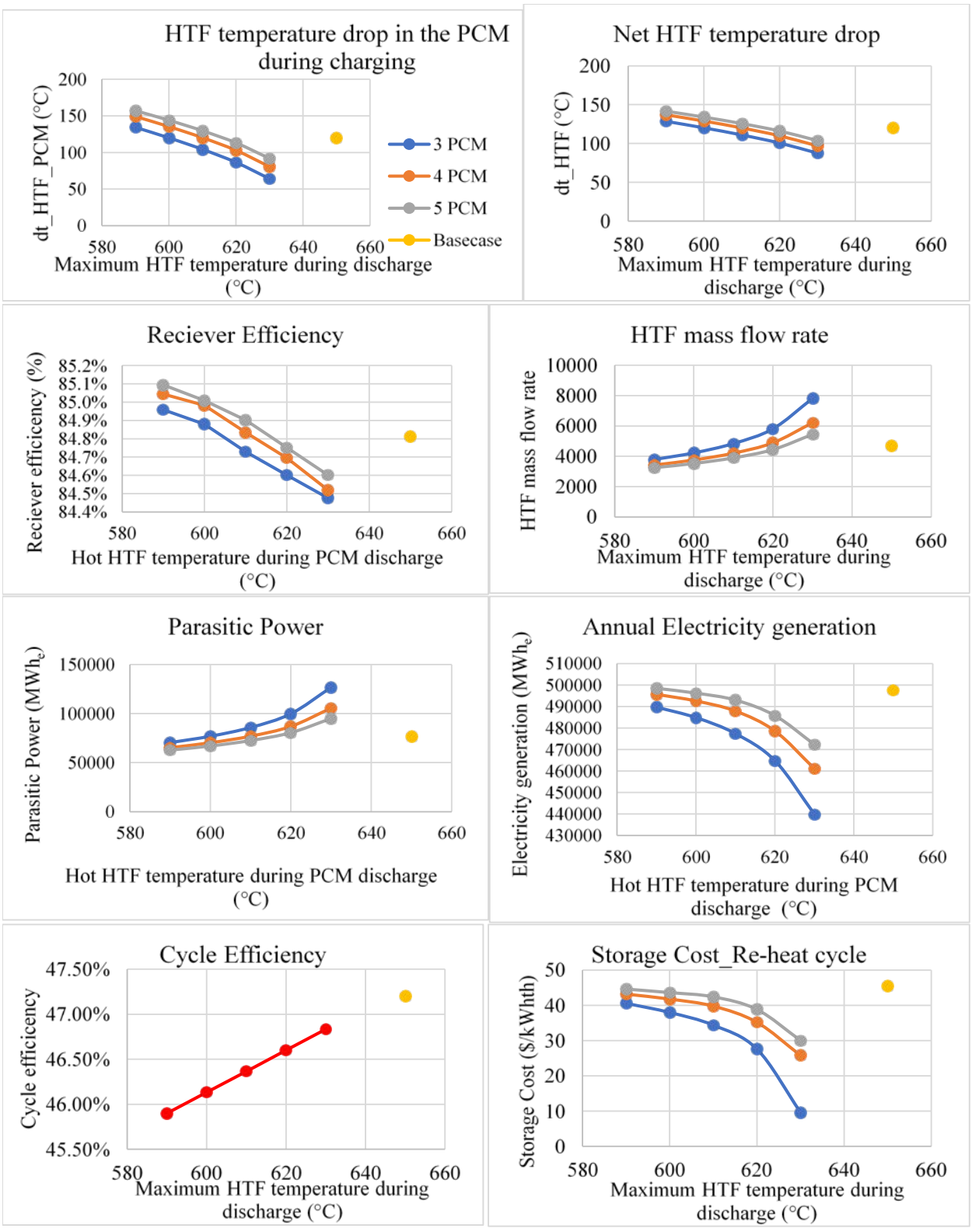

Figure 29. Variation in system performance parameters with maximum HTF temperature during discharge for the reheat cycle.

Figure 29 shows the variation in system performance when the reheat cycle is integrated with the PCM storage. As can be seen in Figure 29, the HTF temperature drop with PCM has much better performance compared to the recompression cycle. For a maximum HTF temperature of 620°C, a net HTF temperature of 120°C can be achieved, leading to higher receiver efficiency, lower mass flow rate, and ultimately, lower parasitic power and higher annual electricity generation. The annual electricity generation for four- and five-PCM systems is comparable to the base case generation of 500,000 MWh_e/y. This means that the breakeven storage cost for PCM is comparable to the base case storage cost of 45 $/kWh_e$. Hence, having PCM storage with a higher-efficiency reheat cycle gives much better performance compared to two-tank storage.

Break-Even Storage Cost for PCM With Different Power Cycles

The cost of TES using two-tank sensible-heat storage was calculated for the additional power cycles described above for comparison to PCM TES storage options. The two-tank storage cost is highly dependent on the HTF temperature difference between the hot and the cold side. For the base case recompression cycle with two-tank sensible-heat storage, the storage cost is 35 $/kWh_{th}$. For the simple cycle, it is 29 $/kWh_{th}$; for the partial cool cycle, it is 26 $/kWh_{th}$; and for the reheat cycle, it is 45 $/kWh_{th}$. The respective LCOEs for the system are 11.91 ¢/kWh_e, 12.17 ¢/kWh_e, 11.14 ¢/kWh_e, and 12.68 ¢/kWh_e. For the recompression, simple, and partial cool cycles, the break-even storage costs are significantly lower than their respective base case costs.

The maximum break-even costs for the three-, four-, and five-PCM cycles come out to 27.4 $/kWh_{th}$, 19.6 $/kWh_{th}$, and 20.6 $/kWh_{th}$, respectively (Figure 30). However, for the reheat cycle, the breakeven storage costs for PCM and two-tank storage are comparable. It should be noted that we are calculating the break-even storage cost based on the LCOE calculated for each power cycle, as shown in Table 11. Below, we discuss the break-even PCM storage costs needed for the different power cycles to be competitive with the recompression cycle.

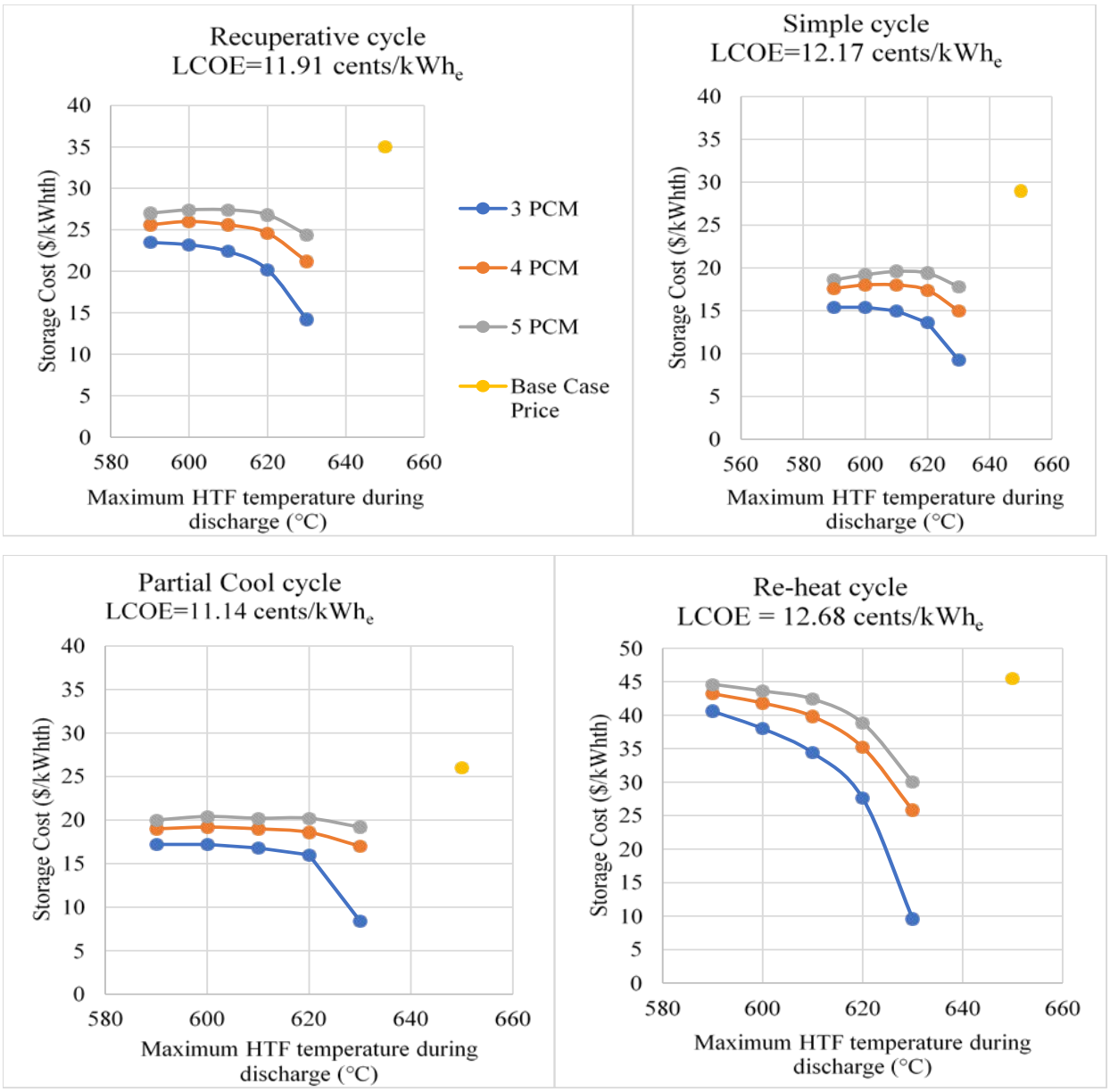

Figure 30. Break-even storage cost for PCM with different power cycles.

Break-Even PCM Storage Cost Compared to Two-Tank Storage Molten Salt Recompression Cycle

The break-even storage cost for PCM that achieves the same LCOE as using two-tank latent-heat TES was calculated for different power cycles. The recompression cycle is one of the most commonly studied cycles. We compared the performance of PCM storage integrated into the recompression cycle with molten salt to the reheat cycle with molten salt. The break-even PCM storage cost was calculated to match the LCOE of the recompression cycle with two-tank storage (11.91 ¢/kWh$_e$). The results are shown in Table 12.

Table 12. Break-Even PCM Storage Costs Required to Achieve the LCOE of Base Case Recompression Cycle with Two-Tank Storage (11.91 ¢/kWh$_e$).

			Recompression Cycle Molten Salt	Reheat Cycle Molten Salt
	LCOE	¢/kWh$_e$	11.91	11.91
Break-Even Storage Cost	3 PCM	$/kWh$_{th}$	14.2,[a] 20.2,[b] 22.2,[c] 23.2,[d] 23.5[e]	-,[a] 12.2,[b] 19,[c] 22.6,[d] 25.2[e]
	4 PCM		21.2,[a] 24.6,[b] 25.6,[c] 26,[d] 25.6[e]	10.4,[a] 20.2,[b] 24.4,[c] 26.4,[d] 27.8[e]
	5 PCM		21.2,[a] 24.6,[b] 25.6,[c] 26,[d] 25.6[e]	14.6,[a] 23.4,[b] 27,[c] 28.1,[d] 29.2[e]

Note that a, b, c, d, and e correspond to HTF discharge temperatures of 630°C, 620°C, 610°C, 600°C, and 590°C, respectively

Thermal Analysis of the PCM System and the Cost Calculation for Thermal Energy Storage

To develop the cost model of PCM storage, we used the PCM model developed by (Sharan, Turchi, and Kurup 2019). A shell and tube heat exchanger will be made from nickel alloy to tackle such a high temperature. The analytical formulation for calculating the discharging temperature profile over time (t) for radial geometry is:

$$t_d[i+1]-t_d[i]=\frac{M_{pcm,\Delta l}\lambda_{pcm}}{2\pi\Delta l\left(LMTD_{PCM-oil}\right)}\left(\left(\frac{2}{h_i d_{i,t}}+\frac{\ln\left(\frac{d_{o,t}}{d_{i,t}}\right)}{k_t}-\frac{1}{2k_{pcm}}\right)\left(X_{so,pcm}[i+1]-X_{so,pcm}[i]\right)+\left(\frac{\left(1+RX_{so,pcm}[i+1]\right)\ln\left(1+RX_{so,pcm}[i+1]\right)-\left(1+RX_{so,pcm}[i]\right)\ln\left(1+RX_{so,pcm}[i]\right)}{2Rk_{pcm}}\right)\right) \quad (3)$$

where M, T, λ , k, X_{so}, and X_l are mass, temperature, latent heat, thermal conductivity, solid fraction, and liquid fraction of the PCM, respectively; h_i and k_t are the convective heat transfer and thermal conductivity of the steel tube, respectively; and d is the diameter. The log mean temperature difference(LMTD) is the logarithmic temperature difference between the PCM and oil. Here, R is defined as:

$$R=\frac{p^2}{d_{o,t}^2}-1 \quad (4)$$

where p is the tube pitch or diameter of PCM surrounding the tube. Using Eq (3) and Eq (4), we can calculate the diameter of PCM surrounding the tube. The PCM heat transfer characteristic decreases with charge state; hence, we selected the PCM thickness based on its worst performance.

In the following example, we calculate the storage cost assuming a recompression cycle using a four-PCM system for TES. For a four-PCM system with maximum HTF temperature of 590°C,

the ideal PCM melting points should be 595°C, 550°C, 509.1°C, and 472.3°C. The net power cycle efficiency is 43.8%, and the net storage capacity is 2,625 MWh_{th}. For thermal enhancement, graphite foam is used. Graphite foam can enhance the thermal conductivity of PCMs to 21 W/mK (Singh et al. 2018). Table 13 summarizes the design and cost parameters used for the PCM storage cost calculations in this section.

Table 13. Design and Cost Parameters for PCM Storage Cost Calculations

Parameter	Value	Unit
Stored energy	2,625	MW_{th}-hr
Thermal conductivity enhancement	Graphite foam	
Equivalent thermal conductivity of PCM	21.4	W/mK
Mass fraction of graphite in the PCM	12.5	%
Volume fraction of graphite	10	%
Nickel alloy heat exchanger cost correlation	$905.6A + 98686$	$
Graphite foam cost	10	$/kg
Insulation cost	$0.000283T^2 + 0.4087T + 54.47$	$/m^2
Heat loss flux	300	W/m^2

Table 9 shows the possible PCMs available in the temperature range of 430°–645°C. Selecting PCM melting temperatures close to the ideal PCM melting temperature results in PCM 1 = 594°C ($Ba(NO_3)_2$), PCM 2 = 551°C (KCl-$BaCl_2$-$CaCl_2$), PCM 3 = 504°C (KCl-NaCl-$CaCl_2$), and PCM 4 = 475°C ($BaCl_2$-$CaCl_2$-$MgCl_2$-NaCl). Ideally, the storage should discharge by 10% every hour if it is fully charged. However, because the PCM heat transfer performance deteriorates with charge state, it takes a significantly longer time to discharge from 90% to 100%. For the present case, the maximum discharge time from 90% to 100% is assumed to be 1.5 hours. The diameter of PCM surrounding the tube is selected in such a way that the time taken for the PCM to discharge from 90% to 100% is 1.5 hours.

Figure 31 shows the heat profile for the PCM charging and discharging. The net heat capacities for PCMs 1, 2, 3, and 4 are 914 MWh_{th}, 701 MWh_{th}, 748 MWh_{th}, and 327 MWh_{th}, respectively, and the optimal PCM thickness for each comes out to 9.4 cm, 10.8 cm, 9.9 cm, and 11.9 cm, respectively. The storage cost for the system comes out to 43.2 $/$kWh_{th}$. The reason for the higher cost of storage is the relatively high PCM 1 cost and the lower LMTD of 20°C, leading to lower PCM thickness and higher heat exchanger area. The total PCM 1 storage module cost, including the costs in Table 13, is 55 $/$kWh_{th}$. The break-even storage cost for PCM storage is 25.6 $/$kWh_{th}$.

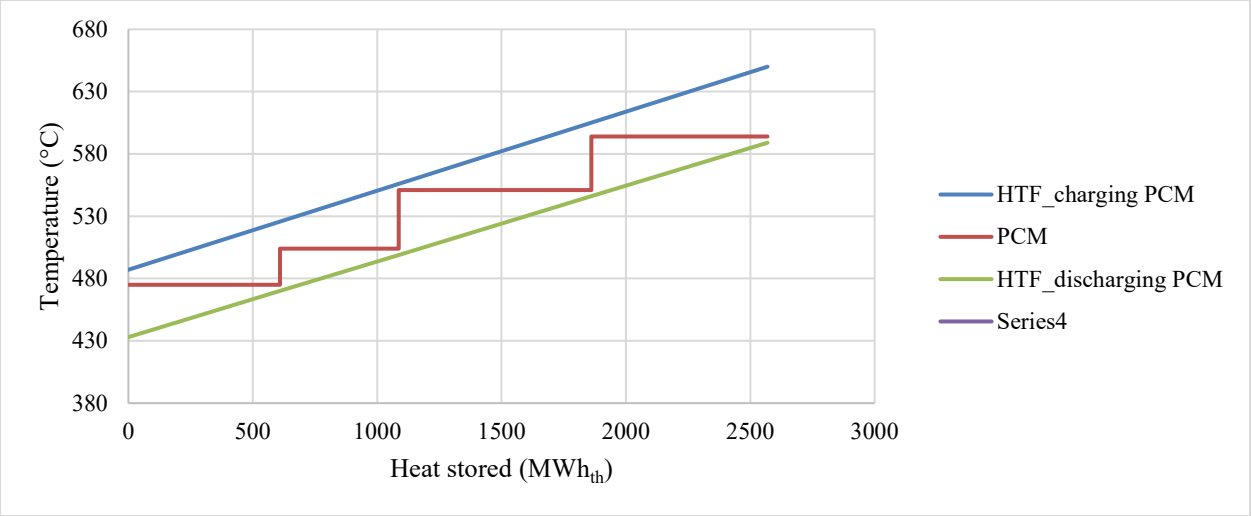

Figure 31. Heat profile for PCM during charging and discharging.

Selecting different PCMs with melting temperatures of 623°C, 573°C, 535°C, and 487°C gives a storage cost of 20.2 \$/kWh$_{th}$. Optimal selection of PCMs can help in significantly reducing the cost of storage. By increasing the maximum HTF temperature during discharge to 600°C, the PCM storage cost achieved is 20.7 \$/kWh$_{th}$.

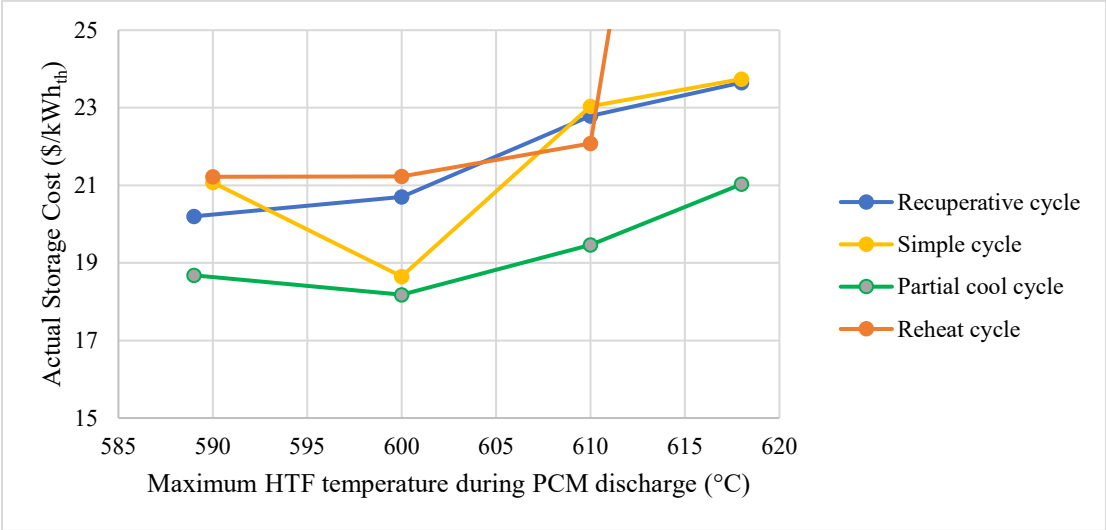

Figure 32. Actual storage for PCM with maximum HTF temperature during PCM discharge.

The actual storage costs for different power cycles are plotted against different HTF temperatures during PCM discharge in Figure 32. The cost of PCM storage can be brought down to less than 20 \$/kWh$_{th}$, and the minimum cost of PCM storage achieved is 18.2 \$/kWh$_{th}$ for the partial cool cycle. The cost of storage is lower than the break-even cost of PCM storage calculated in Table 12, and cascaded PCM shows potential to replace two-tank energy storage. Given the uncertainties in PCM costs and operation, recommended future work should (i) develop detailed cost models to verify potential cost savings and (ii) investigate the impact of system off-design caused by the difference in cycle inlet temperature between heating the cycle directly from the receiver and heating the cycle directly from the PCM. For the reheat cycle, the

storage cost is slightly greater than that of the other power cycle (21 $/kWh$_{th}$) but still lower than the break-even storage cost of 25 $/kWh$_{th}$. In addition, the reheat cycle storage cost can be more economical than that of the recompression cycle. The reason for the higher storage cost for the reheat cycle is the lower temperature difference for the HTF, which ultimately leads to lower LMTD between the PCM and HTF.

Decoupling Field and Cycle HTF Flows in the CSP Plant Controller Model

We modified the CSP plant controller to allow for the decoupling of field operation and TES charging from TES discharging and power cycle operation. This operation scheme is recommended by industry and better insulates the power cycle from receiver thermal transients. This framework is also important for other research projects. For example, a clear-sky DNI controller and warming the receiver with cold TES both require the new plant configuration.

In the existing "coupled" plant configuration, the cycle always used HTF from the field as it was available. Likewise, the field inlet always used HTF from the cycle outlet as it was available. Consequently, the TES operation at any one time only required a single mass flow rate—either charging at a known temperature or discharging at the mixed tank temperature. First, we confirmed that our analytical tank energy and mass balance model accurately captured simultaneous inlet and outlet mass flows.

Because the "decoupled" configuration requires all mass to pass through the TES, it requires different strategies than the coupled configuration to converge the system mass and energy. The current version of the code contains unique solvers for most plant operating modes. From the existing solvers and new requirements, we developed a generalized version that applies four nested iteration loops to solve for defocus, timestep, field cold HTF inlet temperature, and cycle HTF mass flow rate, as necessary (Figure 33). By defining for each operating mode the field and cycle state and expectations for the TES and cycle, this framework solves all system operating modes. In addition to enabling the decoupled configuration, the new framework reduces the amount of solver code and the number of calls to component classes.

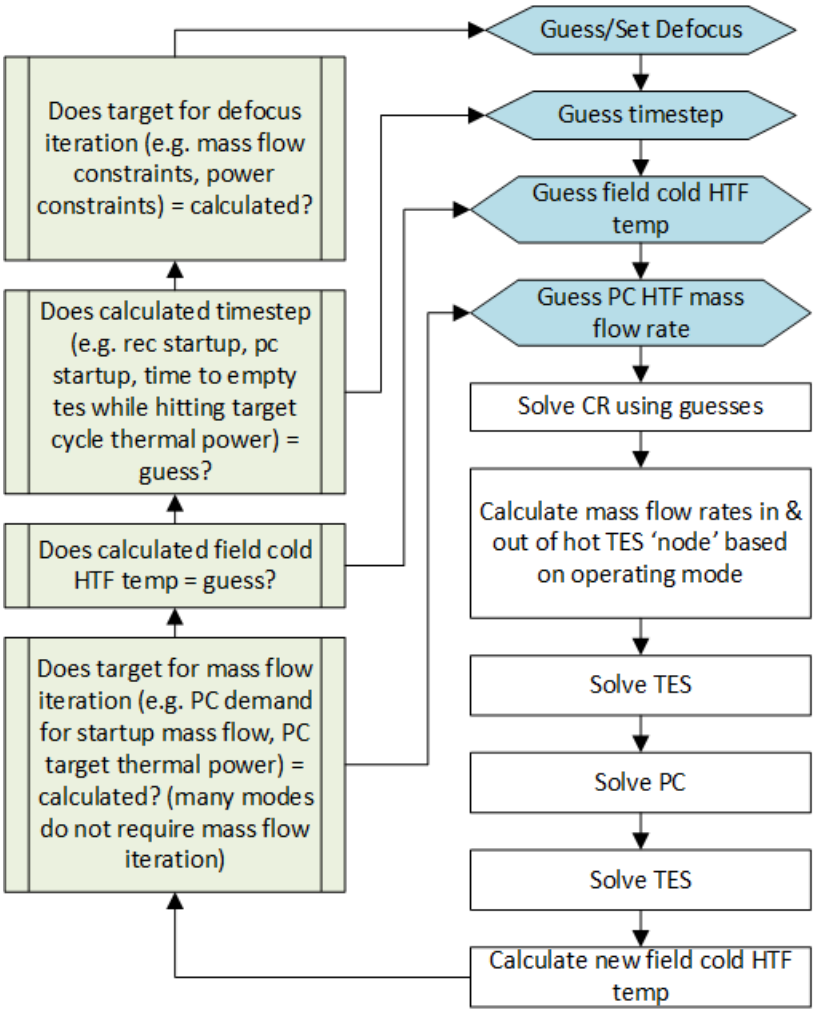

Figure 33. CSP plant controller algorithm for decoupled field configuration, which allows TES charging from field operation and TES discharging from power cycle operation simultaneously (PC = power cycle).

Table 14 shows the annual energy for different technologies and configurations for the 20.02.29 SAM release, the new code in "parallel" mode, and the new code in "serial" mode for a range of plant configurations. (The plant operation is always parallel in the 20.02.29 version of the controller.) The configurations in the table span conventional cases to extreme cases not normally deployed commercially. The point of these cases is to get the plant controller to test operating modes that usually don't occur during "typical" CSP simulations, usually involving some combination of defocus, emptying or filling TES during a timestep, and cycle standby. Results between the three codes are reasonably close, and a small bug fix related to simultaneous startup of the field and TES led to the small differences between the 20.02.29 release and the updated parallel framework. The difference between the parallel and serial options is 1% or less of total generation.

Table 14. Comparison of 20.02.29 SAM Release Annual Energy Generation to Updated Code in Parallel and Serial Modes Using SAM CSP Power Tower Module

	20.02.29 Release	Branch Parallel	Branch Serial
Trough	372,982,592	370,649,760	-
Direct trough	380,691,424	378,173,504	376,988,608
IPH trough	24,480,118	24,318,440	24,414,434
IPH steam	10,935,303	10,846,580	10,846,580
MSPT	550,333,056	550,236,864	550,428,672
MSPT (No generation in AM hours)	391,018,144	390,736,224	390,520,032
MSPT with oversized power cycle (Solar multiple = 0.5 and TES = 0.5 hours)	49,026,312	49,432,456	49,816,980
MSPT with no TES	294,607,776	294,599,968	294,599,968

SAM results for a parabolic trough plant using the parallel and serial operation modes of the decoupled TES-power cycle configuration are shown in Figure 34 and Figure 35. The Parabolic Trough – Physical SAM model was used with VP-1 selected as the HTF. The results demonstrate how flow from the solar field to TES and/or the power cycle differ for each operation mode.

Decoupled Configuration – Parallel Mode

Parallel operation supplies the cycle first with mass flow from the field, and then from the storage if necessary and available (Figure 34). This control makes the cycle inlet temperature vulnerable to variability in the receiver outlet temperature. The trough model turns down the mass flow rate when the receiver outlet temperature falls such that the effect on turbine inlet temperature is fairly small. However, receiver operating schemes that could result in near-design mass flow rates at sub-design outlet temperatures (e.g., clear sky DNI receiver mass flow rate control) could significantly decrease the turbine inlet temperature in parallel operation.

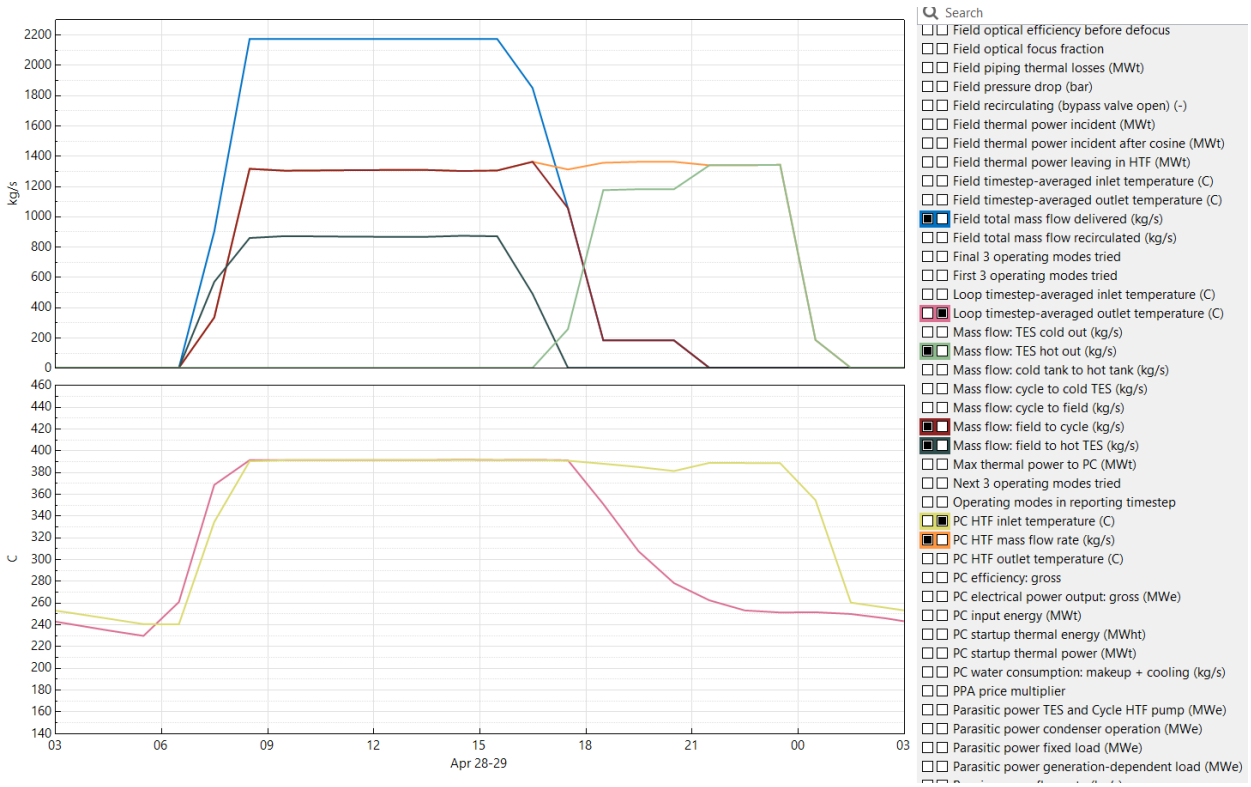

Figure 34. Temperature and flow rate of streams between field, TES, and power cycle for parallel operation of the Parabolic Trough – Physical model using the decoupled configuration code.

Decoupled Configuration – Serial Mode

Serial operation avoids variation in turbine inlet temperature by only sending HTF from hot TES to the power cycle (Figure 35). Note that in this plant configuration, the TES hot tank inlet mass flow rate is equal to the field mass flow rate, and the TES hot tank outlet mass flow rate is equal to the power cycle mass flow rate.

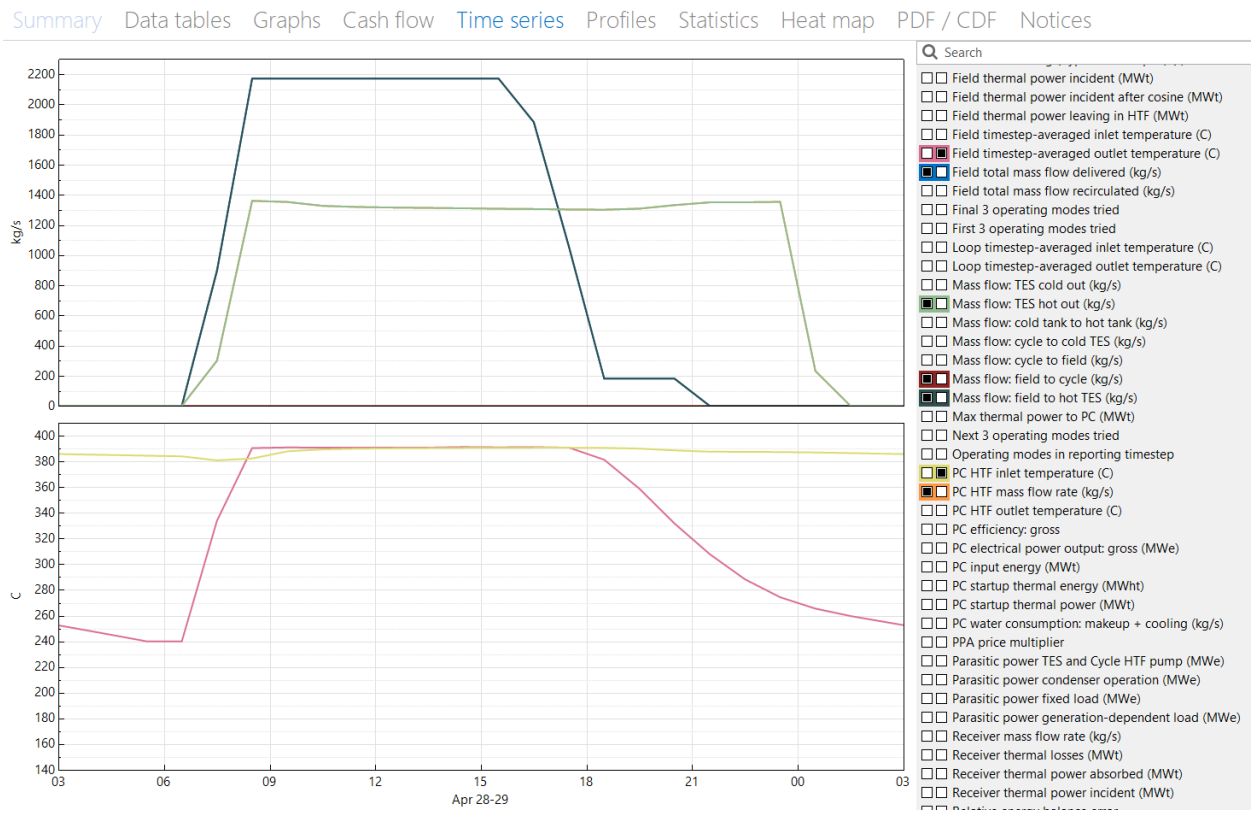

Figure 35. Temperature and flow rate of streams between field, TES, and power cycle for serial operation of the Parabolic Trough – Physical model using the decoupled configuration code.

Serial/Parallel Checkbox on Thermal Storage Page

We have added the decoupled configuration option to the SAM UI in the MSPT, physical trough electricity, and physical trough heat models (Figure 36). We have tested this code with different plant designs and time of day schedules that force drastic defocusing, long periods of cycle standby, or many startup and shutdown cycles, and the results have been consistent. This feature was included in the SAM 2020.11.29 release.

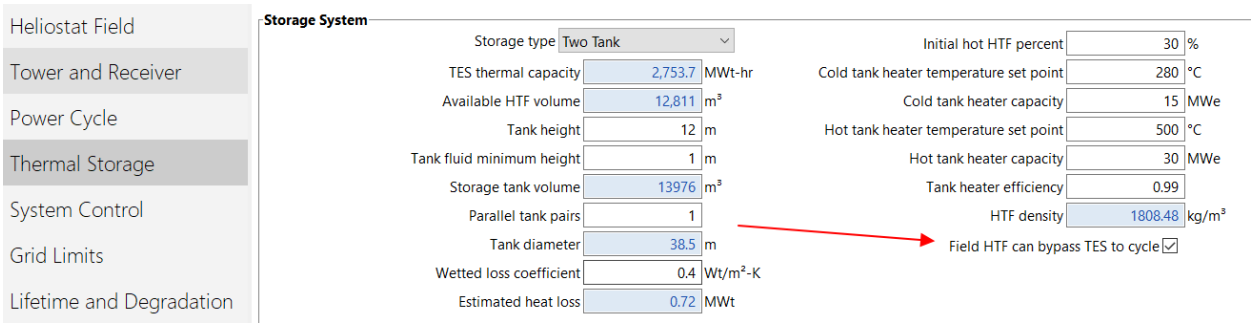

Figure 36. Screenshot of UI from SAM 2020.11.29 release showing the decoupled configuration option for CSP plants with TES.

Improvements to sCO_2 Design-Point and Off-Design Models

CSP Gen3 pathways were tasked with designing their receiver and storage technologies to integrate with the sCO_2 cycle. As such, it is important to offer representative design and off-design assumptions. This task focused on (i) improving the off-design capabilities of NREL's open-source sCO_2 cycle modeling code, (ii) publishing the off-design modeling methodology and modeled off-design behavior, (iii) comparing cycle performance between two compressor models, (iv) releasing updated open-source sCO_2 code with documentation, and (v) and integrating the cycle model with SAM's MSPT model.

Off-Design Model Improvements

At the beginning of this project, we identified several areas for improvement in our off-design model in conjunction with DOE and industry partners:

1) The cycle control model set the main compressor off-design inlet temperature to a fixed approach temperature relative to the ambient temperature. This simplification led to some off-design cases, typically at ambient temperatures colder than design, requiring air-cooler fan power greater than the design power. Although the model calculated and reported this fan power, it is unlikely that the air-cooler design would allow for significant over-design operation.

2) The cycle control model constrained the off-design model to achieve a normalized net power output equal to the normalized inlet HTF mass flow rate. That is, at 50% of the design-point mass flow rate, the controller sought off-design solutions that achieved 50% of the design-point net power output. This constraint is a decent first approximation, but it had the negative consequence of allowing the HTF outlet temperature to float.

3) The cycle model did not have a robust framework for modifying and especially optimizing the compressor shaft speeds. Consequently, the model was not able to approximate the upper bound of cycle performance possible from a compressor with internal guide vane control or turbocompressors.

4) The off-design heat exchanger model used incompressible fluid assumptions to estimate off-design conductance.

To address the first three areas for improvement, we developed a new cycle off-design convergence and control strategy. The cycle convergence routine solves for the numerical solution when all free parameters are specified. The convergence routine neither applies component or cycle constraints nor optimizes the value of free parameters. Instead, the goal of the convergence routine is to return to the control method reliable metrics about the solution. Then, the cycle control method is responsible for choosing free parameters that maximize objectives while satisfying component and system constraints. The innermost loop of the control varies the main compressor inlet pressure to achieve the design-point HTF outlet temperature while limiting the compressor outlet pressure to its design-point value and operating the compressors in feasible ranges of inlet flow coefficient. If necessary, the control will relax the HTF outlet temperature objective until the constraints are met. The loop above the main compressor inlet pressure loop varies the main compressor inlet temperature to maximize cycle net power output (heat input is fixed by the HTF outlet temperature constraint, so this is

equivalent to maximizing efficiency) while limiting the air-cooler fan power to its design value. Finally, optional outer loops optimize compressor shaft speeds to maximize power output. To address the fourth area for improvement, we added the conductance ratio method (Crespi et al. 2017; Hoopes, Sánchez, and Crespi 2016) to our model to estimate the off-design conductance of a compressible fluid.

Journal Publication

We published a journal article (Neises 2020) that describes in detail the methodology and results of the new off-design model. The article defines component performance models and cites background literature. Then, it presents schematics of the numerical convergence and cycle control methods. Next, the paper plots cycle response versus inlet pressure and discusses conditions that lead to constraint violations. After this, the article presents the cycle response to the main compressor inlet temperature while applying inlet pressure control. This section also demonstrates how the inlet pressure control method satisfies constraints and shows that the cycle cannot achieve the design-point HTF outlet temperature at ambient temperatures hotter than design HTF inlet conditions because the outlet pressure is constrained. Then, the paper presents cycle performance with both inlet pressure and inlet temperature control. These results demonstrate that the air-cooler fan power constraint is met and show how power and efficiency vary with ambient temperature and HTF mass flow rate. Next, the paper shows that at ambient temperatures hotter than design, decreasing the HTF mass flow rate to the cycle has minimal negative influence on power and efficiency but allows the HTF outlet temperature to reach the design value. Then, the paper shows how shaft speed control improves cycle performance by both allowing the cycle to operate at a more favorable thermodynamic condition and allowing the compressors to operate closer to their design flow coefficient. Finally, we show that shaft speed control can decrease the difference in efficiency between cold-day and hot-day designs.

In summary, the journal paper contributes the following:

- Detailed description of our modeling methodology, including background and references
- Presentation of a cycle convergence and control method with full definition of constraints, objectives, and assumptions
- Explanation of cycle response to free parameters
- Explanation of cycle capacity limitations on hot days under reasonable assumptions
- Comparison and explanation of fixed and optimized shaft speed control.

Compressor Comparison

Our compressor model uses a modeled performance map developed by Barber-Nichols Inc. for a roughly 50-kW_e radial compressor. Results from this map were validated by experimental data measured by Sandia National Laboratories. Dyreby (Dyreby et al. 2014) presented this compressor data using the dimensionless parameters shown below. Then, Dyreby used the data from the Barber-Nichols performance maps to fit polynomials that represent the ideal head coefficient and normalized isentropic efficiency as a function of the flow coefficient. The design-point flow coefficient is the value that results in the maximum isentropic efficiency.

$$\text{Ideal Head Coefficient: } \psi = \frac{\Delta h_{ideal}}{U^2}$$

$$\text{Flow Coefficient: } \phi = \frac{\dot{m}}{\rho U D^2} = \frac{\dot{V}}{U D^2}$$

$$\text{where the tip speed } U = \frac{D_{rotor}}{2} N$$

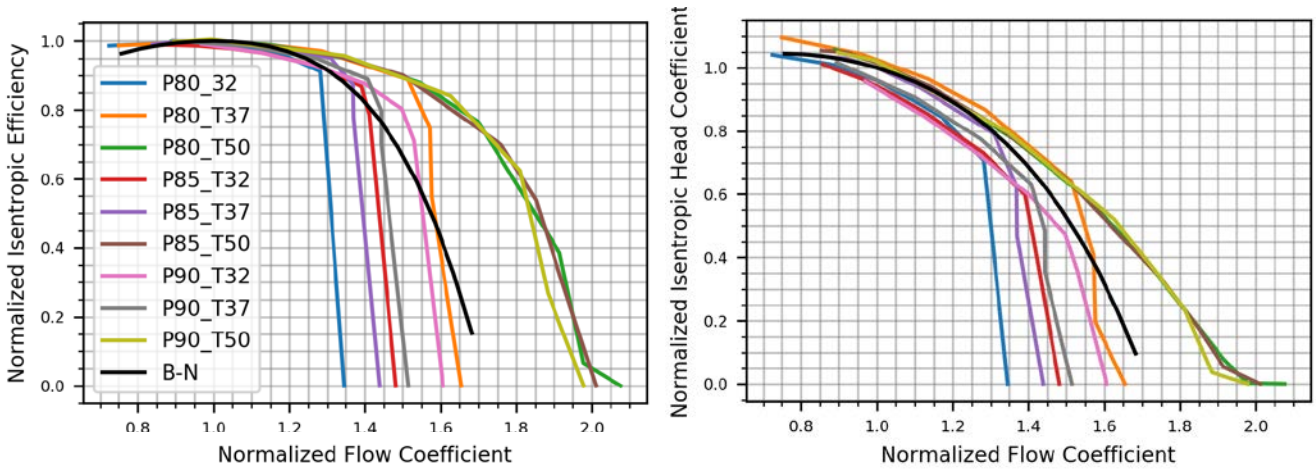

Figure 37. Normalized isentropic efficiency and ideal head coefficient versus normalized flow coefficient for the Barber-Nichols compressor (black) and the Hanwha compressor at various inlet pressures.

The cycle design model selects the state points and mass flow rates that result in the best thermal efficiency given design parameters and constraints. Isentropic efficiency is the only compressor input parameter to the cycle *design* model. After the cycle selects the design point, the compressor model designs the compressor by calculating the compressor shaft speed to satisfy the design-point ideal head coefficient and calculating the compressor diameter to satisfy the design-point flow coefficient.

The *designed* compressor must operate at every off-design case at a flow coefficient that balances mass flow and pressures with the rest of the system. The shaft speed and rotor diameter of the designed compressor are fixed and become constants in the dimensionless equations. Therefore, when calculating the performance of the designed compressor, the relative change in ideal head rise (Δh_{ideal}) is a function of the relative change in ideal head coefficient, and the relative change in volumetric flow rate ($\dot{V}$) is a function of the relative change in the flow coefficient. It follows that we can compare two different compressor performance maps by normalizing the values by their respective design points.

Hanwha Power Systems Americas provided us with modeled data[5] for one of their radial compressor designs. They note (Pelton and Jung 2019) that varying compressor inlet conditions can result in different relationships between the ideal head coefficient, isentropic efficiency, and the flow coefficient. Consequently, they provided (somewhat sparse) data tables of the dimensionless parameters for different combinations of compressor inlet temperatures and

[5] Hanwha data is business sensitive and not available for public distribution.

pressures. We added this data to our cycle model as a compressor model type that interpolates the data tables at different compressor inlet conditions to find the dimensionless parameters as a function of flow coefficient.

Figure 37 compares the normalized ideal head coefficient and normalized isentropic efficiency to the normalized flow coefficient of the Barber-Nichols compressor, which is only available for one compressor inlet condition, and the Hanwha compressor data, which is available for multiple compressor inlet conditions. We used the design-point inlet conditions from Hanwha's paper. The top subplot shows that the normalized efficiencies are within a few points and the ideal head coefficients vary up to 10% when the normalized flow coefficient is between about 0.85 and 1.3. However, when the flow coefficient is greater than 1.3, the different curves fall off at different flow coefficients. Hanwha's paper attributes this to the relationship of the speed of sound and specific heat to the CO_2 state, which can change the flow coefficient at which the compressor experiences choked flow. The curves also show different minimum normalized flow coefficients, which represent the surge points for each curve.

We configured the recompression cycle model to run with the main compressor model using the Hanwha compressor data. Then, we ran the cycle model with two different cycle designs. One design used the Hanwha compressor design inlet (8.5 MPa, 37°C) and outlet (16.36 MPa) conditions. The other design used a recompression cycle designed with Gen3 compressor parameters (9.25 MPa, 41°C, 25 MPa). Then, we compared the performance of the cycle model using the two compressor models. Off-design cycle performance for the Hanwha cycle design over a range of ambient temperatures shows that, relative to the Barber-Nichols compressor, at colder ambient temperatures, the Hanwha compressor experiences around a one point reduction in isentropic efficiency, a 5% decrease in specific compressor work, and a slight decrease in inlet pressure and temperature. The combined effect of these differences is that the difference in cycle thermal efficiency between the two compressor cases is insignificant.

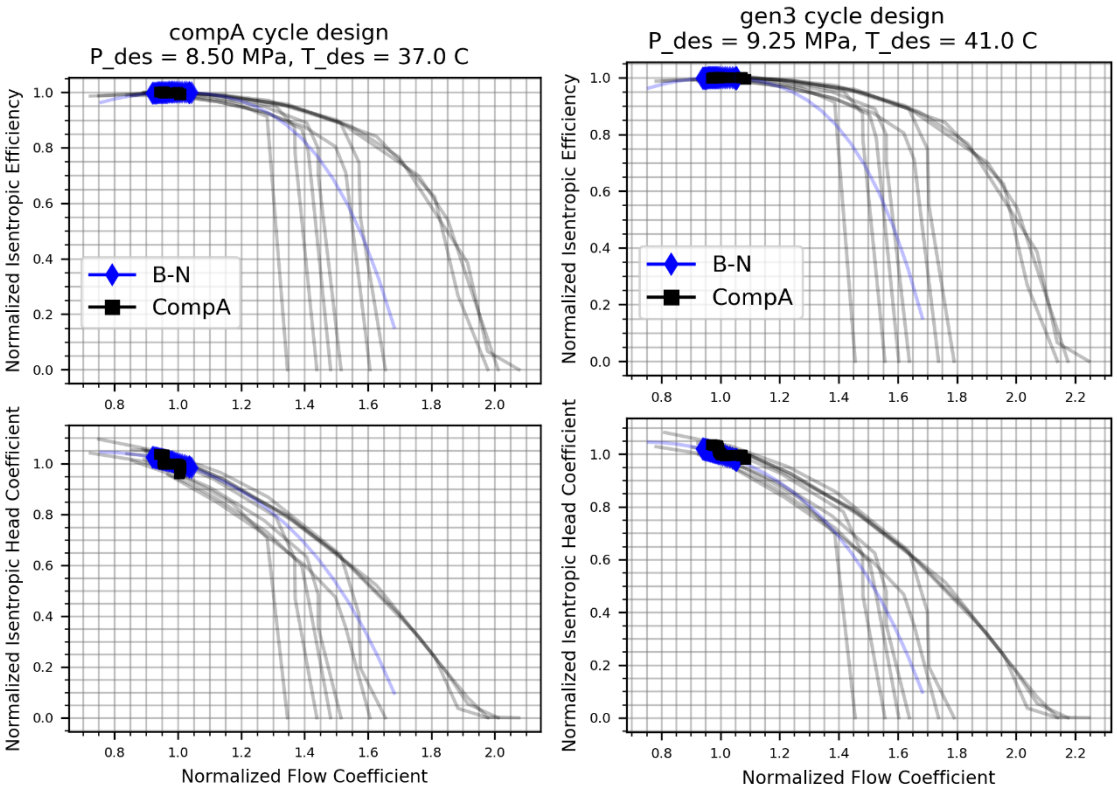

Figure 38. Normalized dimensionless compressor off-design performance for the Hanwha cycle design ("CompA," left) and the Gen3 cycle design (right) over a range of ambient temperatures.

This similarity might be unexpected given the difference in the normalized dimensionless curves in Figure 37. However, Figure 38 (left) shows that over the range of off-design ambient temperatures in this analysis, the compressor normalized flow coefficient remains in a very narrow range, bracketing the design flow coefficient (i.e., 1) from about 0.9 to 1.05. In this range, the normalized isentropic efficiencies of both compressors remain close to unity, and the normalized ideal head coefficients remain within 10%. In the case of the Gen3 cycle design, the comparison between the Hanwha compressor and the Barber-Nichols compressor shows opposite differences but the same net effect: the difference in cycle thermal efficiency between the two compressor cases is insignificant. It is important to note that our model assumes inventory control can adjust the compressor inlet pressure to achieve the target cycle power. Without this assumption, there would likely be more variation. However, inventory control is a common assumption for most sCO_2 applications, and the cycle in general would perform much worse without it, regardless of the compressor model.

This comparison gives us confidence, *for the purposes of steady-state off-design cycle modeling*, that the Barber-Nichols compressor map gives reasonable results. The comparison showed that, for our modeling assumptions, the main compressor typically operates within ±10% of its normalized design flow coefficient. Consequently, we expect that for our modeling assumptions, the cycle model results will remain similar if the main compressor model has a similar normalized ideal head coefficient and normalized isentropic efficiency responses over a ±10% range of normalized flow coefficient. It is important to note that the comparison assumed that each compressor had the same design-point isentropic efficiency. So, although the Barber-

Nichols map may provide reasonable off-design characteristics, the cycle and compressor model still require the user to choose a reasonable isentropic efficiency. Furthermore, compressor curves that operate over a wider range of normalized flow coefficients may have other advantages during startup or transients that aren't captured by our steady-state modeling approach.

Open-Source Cycle Model

The sCO_2 cycle model described in this report is accessible via a Python scripting interface, for which instructions, documentation, and examples are available on GitHub. The Python code contains methods to optimize and plot cycle designs, solve one-off cycle off-design performance using the control method described above or by inputting custom control parameters, and solve and write a file of off-design performance combinations required for SAM's user-defined power cycle model.

Integration With SAM

We removed from SAM (2020.11.29) the option that directly called the sCO_2 off-design model from the interface and replaced it with a macro that reads in output from the Python code and automatically configures the tower system with a user-defined power cycle (Figure 39). The macro gives the user more control over the sCO_2 model by providing the full menu of design parameters and control options. The macro also decouples the relatively slow cycle model from the SAM simulation and allows users to store files of different design/off-design combinations from Python. The macro also interfaces with the Python output to adjust other design parameters in SAM, like cold HTF temperature and cycle efficiency, to ensure the Python and SAM parameters are consistent.

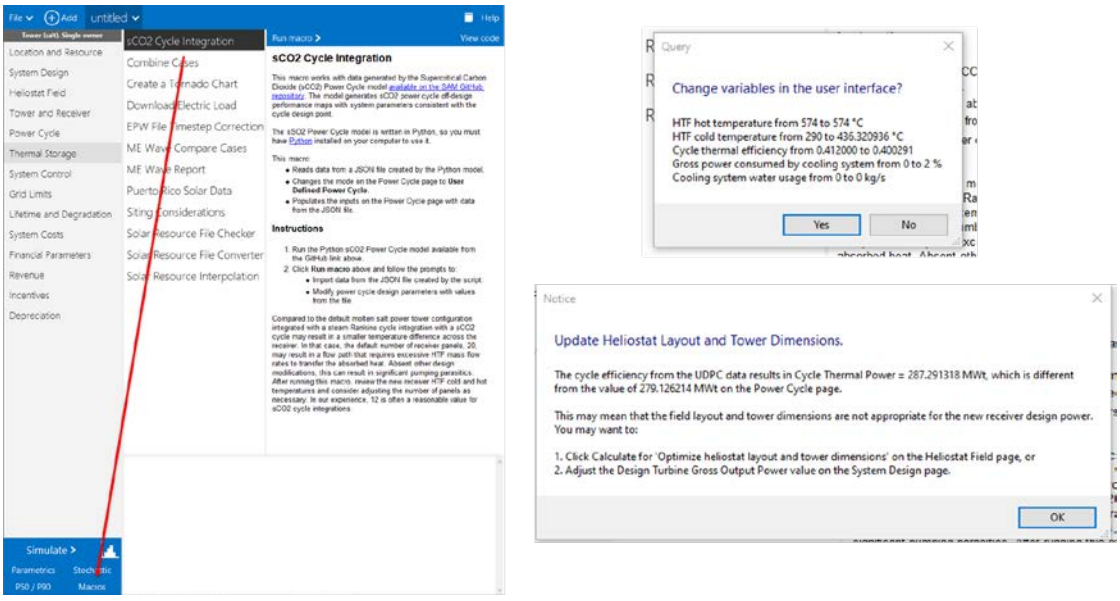

Figure 39. Screenshots of SAM showing the sCO_2 cycle integration macro and its user-input windows.

References

Akar, Sertaç, Chad R. Augustine, Parthiv Kurup, and Margaret K. Mann. 2018. "Global Value Chain and Manufacturing Analysis on Geothermal Power Plant Turbines." NREL/TP-6A20-71128. Golden, CO: National Renewable Energy Lab (NREL). https://www.nrel.gov/docs/fy18osti/71128.pdf.

Boothroyd Dewhurst Inc. 2019. "Design for Manufacture and Assembly (DFMA) Product Costing and Simplification." 2019. https://www.dfma.com/software/dfma.asp.

Coventry, Joe, and John Pye. 2014. "Heliostat Cost Reduction – Where to Now?" *Energy Procedia*, Proceedings of the SolarPACES 2013 International Conference, 49 (January): 60–70. https://doi.org/10.1016/j.egypro.2014.03.007.

Crespi, Francesco, David Sánchez, Kevin Hoopes, Brian Choi, and Nicole Kuek. 2017. "The Conductance Ratio Method for Off-Design Heat Exchanger Modeling and Its Impact on an SCO2 Recompression Cycle." In *Volume 9: Oil and Gas Applications; Supercritical CO2 Power Cycles; Wind Energy*, V009T38A025. Charlotte, North Carolina, USA: American Society of Mechanical Engineers. https://doi.org/10.1115/GT2017-64908.

Dersch, Jürgen, Simon Dieckmann, Klaus Hennecke, Robert Pitz-Paal, Dirk Krüger, and Pablo Ralon. 2019. "LCOE Reduction Potential of Parabolic Trough and Solar Tower Technology in G20 Countries until 2030." In . https://www.researchgate.net/publication/337438974_LCOE_Reduction_Potential_of_Parabolic_Trough_and_Solar_Tower_Technology_in_G20_Countries_until_2030.

Dersch, Jürgen, Simon Dieckmann, Klaus Hennecke, Robert Pitz-Paal, Michael Taylor, and Pablo Ralon. 2020. "LCOE Reduction Potential of Parabolic Trough and Solar Tower Technology in G20 Countries until 2030." In , 120002. Daegu, South Korea. https://doi.org/10.1063/5.0028883.

Dieckmann, S, Jürgen Dersch, Stefano Giuliano, M Puppe, E Lupert, Klaus Hennecke, R Pitz-Paal, M Taylor, and P Ralon. 2017. "LCOE Reduction Potential of Parabolic Trough and Solar Tower CSP Technology until 2025." In . Abu Dhabi: AIP Publishing.

DOE. 2014. "PROJECT PROFILE: Abengoa Solar, LLC – ATLAS." Energy.Gov. 2014. https://www.energy.gov/eere/solar/project-profile-abengoa-solar-llc-atlas.

DOE EERE. 2021. "Guide to the Federal Investment Tax Credit for Commercial Solar Photovoltaics." https://www.energy.gov/sites/default/files/2021/02/f82/Guide%20to%20the%20Federal%20Investment%20Tax%20Credit%20for%20Commercial%20Solar%20PV%20-%202021.pdf.

DOE SETO. 2021. "2030 Solar Cost Targets." Energy.Gov. August 13, 2021. https://www.energy.gov/eere/solar/articles/2030-solar-cost-targets.

Dyreby, John, Sanford Klein, Gregory Nellis, and Douglas Reindl. 2014. "Design Considerations for Supercritical Carbon Dioxide Brayton Cycles With Recompression." *Journal of Engineering for Gas Turbines and Power* 136 (10): 101701. https://doi.org/10.1115/1.4027936.

Guédez, Rafael, Monika Topel, Inés Conde Buezas, Francisco Ferragut, Irene Callaba, James Spelling, Zhor Hassar, Carlos David Pérez-Segarra, and Björn Laumert. 2015. "A Methodology for Determining Optimum Solar Tower Plant Configurations and Operating Strategies to Maximize Profits Based on Hourly Electricity Market Prices and Tariffs." In . American Society of Mechanical Engineers Digital Collection. https://doi.org/10.1115/ES2015-49237.

Hoopes, Kevin, David Sánchez, and Francesco Crespi. 2016. “A New Method for Modelling Off-Design Performance of SCO2 Heat Exchangers Without Specifying Detailed Geometry.” In . San Antonio, Texas. https://sco2symposium.com/papers2016/HeatExchanger/013paper.pdf.

Kattke, Kyle. 2019. “The Drop-In, Ring-of-Power Heliostat.” SETO CSP Program Summit 2019, March 19. https://www.energy.gov/sites/default/files/2019/04/f62/CSP%20Summit2019%20Solar%20Dynamics%20Kattke%20DropC.pdf.

Keck, Thomas, Markus Balz, Verena Göcke, Finn von Reeken, Fabian Gross, Willem Landman, Javier Collado, Joaquín Salas, Joaquín Gracia, and Jesus Iriondo. 2019. “Hami–The First Stellio Solar Field.” In *AIP Conference Proceedings*, 2126:030029. AIP Publishing LLC. https://doi.org/10.1063/1.5117541.

Kenisarin, Murat M. 2010. “High-Temperature Phase Change Materials for Thermal Energy Storage.” *Renewable and Sustainable Energy Reviews* 14: 955–70. https://doi.org/10.1016/j.rser.2009.11.011.

Kerkhoff, Jacob A., and Michael J. Wagner. 2021. “A Flexible Thermal Model for Solar Cavity Receivers Using Analytical View Factors.” In . American Society of Mechanical Engineers Digital Collection. https://doi.org/10.1115/ES2021-63810.

Kolb, Gregory J., Scott A. Jones, Matthew W. Donnelly, David Gorman, Robert Thomas, Roger Davenport, and Ron Lumia. 2007. “Heliostat Cost Reduction Study.” SAND2007-3293. Albuquerque, New Mexico: Sandia National Laboratories. https://prod-ng.sandia.gov/techlib-noauth/access-control.cgi/2007/073293.pdf.

Kraemer, Susan. 2019. “A Novel CSP Heliostat Goes from Lab to Market in Just 5 Years.” December 3, 2019. https://www.solarpaces.org/a-novel-csp-heliostat-goes-from-lab-to-market-in-just-5-years/.

Kurup, Parthiv, Sertaç Akar, and Chad Augustine. 2022. “Heliostat Initital Supply Chain Analysis.” TBD. Golden, CO: National Renewable Energy Laboratory. TBD.

Kurup, Parthiv, Sertac Akar, Stephen Glynn, Chad Augustine, and Patrick Davenport. 2022. “Cost Update: Commercial and Advanced Heliostat Collectors.” NREL/TP-7A40-80482. National Renewable Energy Lab. (NREL), Golden, CO (United States). https://doi.org/10.2172/1847876.

Kurup, Parthiv, Stephen Glynn, and Sertaç Akar. 2020. “Manufacturing Cost Analysis of Advanced Parabolic Trough Collector.” In *AIP Conference Proceedings*. Albuquerque, New Mexico: AIP Publishing. TBD.

Kurup, Parthiv, Stephen Glynn, and Sertac Akar. 2021a. “Manufacturing Cost Analysis of Advanced Parabolic Trough Collector: Preprint.” In *AIP Conference Proceedings*. Online Event: National Renewable Energy Laboratory. https://www.nrel.gov/docs/fy21osti/77829.pdf.

Kurup, Parthiv, Stephen Glynn, and Sertaç Akar. 2021b. “Manufacturing Cost Analysis of Advanced Parabolic Trough Collector: Preprint.” In *AIP Conference Proceedings*. Albuquerque, New Mexico: NREL. https://www.nrel.gov/docs/fy21osti/77829.pdf.

Kurup, Parthiv, Timothy Remo, Dale Scott Jenne, Jason Cotrell, and Patrick O’Connor. 2018. “Analysis of Supply Chains and Advanced Manufacturing of Small Hydropower.” NREL/TP-6A20-71511. Golden, CO: National Renewable Energy Laboratory (NREL). https://www.nrel.gov/docs/fy18osti/71511.pdf.

Kurup, Parthiv, and Craig Turchi. 2015a. "Parabolic Trough Collector Cost Update for the System Advisor Model (SAM)." Technical Report NREL/TP-6A20-65228. Golden, CO: NREL. http://www.nrel.gov/docs/fy16osti/65228.pdf.
Kurup, Parthiv, and Craig S Turchi. 2015b. "Parabolic Trough Collector Cost Update for the System Advisor Model (SAM)." *Renewable Energy*, 40.
List Solar. 2021. "DLR Testing Using Molten Salt in a Solar Energy Plant in Portugal." October 26, 2021. https://list.solar/news/dlr-testing-using/.
Marcotte, P., and K. Manning. 2014. "Development of an Advanced Large-Aperture Parabolic Trough Collector."
Mayyas, Ahmad, and Margaret Mann. 2019. "Manufacturing Competitiveness Analysis for Hydrogen Refueling Stations." *International Journal of Hydrogen Energy* 44 (18): 9121–42. https://doi.org/10.1016/j.ijhydene.2019.02.135.
Narayanaswamy, Arvind. 2015. "An Analytic Expression for Radiation View Factor between Two Arbitrarily Oriented Planar Polygons." *International Journal of Heat and Mass Transfer* 91 (December): 841–47. https://doi.org/10.1016/j.ijheatmasstransfer.2015.07.131.
Neises, Ty. 2020. "Steady-State off-Design Modeling of the Supercritical Carbon Dioxide Recompression Cycle for Concentrating Solar Power Applications with Two-Tank Sensible-Heat Storage." *Solar Energy* 212 (December): 19–33. https://doi.org/10.1016/j.solener.2020.10.041.
Neises, Ty, and Craig Turchi. 2019. "Supercritical Carbon Dioxide Power Cycle Design and Configuration Optimization to Minimize Levelized Cost of Energy of Molten Salt Power Towers Operating at 650°C." *Solar Energy* 181: 27–36. https://doi.org/10.1016/j.solener.2019.01.078.
NREL. 2022. "2022 Annual Technology Baseline." 2022. https://atb.nrel.gov/.
O'Rourke, Deven, and Adrian Farr. 2015. "Improved Large Aperture Collector Manufacturing." Abengoa Solar LLC. https://www.energy.gov/sites/prod/files/2016/04/f30/Improved%20Large%20Aperture%20Collector%20Manufacturing%20-%20Abengoa%20Solar%206357.pdf.
Pelton, Robert, and Sewoong Jung. 2019. "Real Gas Effects on the Off-Design Performance of a SCO2 Compressor." In *Proceedings of the Global Power Society Technical Conference*. https://gpps.global/wp-content/uploads/2021/02/GPPS-TC-2019_paper_87.pdf.
Riffelmann, K.-J., A. Schweitzer, G. Weinrebe, and M. Balz. 2019. "Planning and Building the First Ultimate Trough Collector Field in the Kingdom of Saudi Arabia." In *AIP Conference Proceedings*, 2126:040002. AIP Publishing LLC. https://doi.org/10.1063/1.5117582.
Riffelmann, Klaus-Jürgen, Daniela Graf, and Paul Nava. 2011. "Ultimate Trough: The New Parabolic Trough Collector Generation for Large Scale Solar Thermal Power Plants," January, 789–94. https://doi.org/10.1115/ES2011-54657.
Ruegamer, T., H. Kamp, T. Kuckelkorn, W. Schiel, G. Weinrebe, P. Nava, K. Riffelmann, and T. Richert. 2014. "Molten Salt for Parabolic Trough Applications: System Simulation and Scale Effects." *Energy Procedia* 49: 1523–32. https://doi.org/10.1016/j.egypro.2014.03.161.
sbp. 2017. "Ultimate Trough DUBA." 2017. https://www.sbp.de/en/project/ultimate-trough-duba/.
SEIA. 2021. "Solar Investment Tax Credit (ITC)." Solar Energy Industries Association. 2021. https://www.seia.org/initiatives/solar-investment-tax-credit-itc.

Sharan, Prashant, Craig Turchi, and Parthiv Kurup. 2019. “Optimal Design of Phase Change Material Storage for Steam Production Using Annual Simulation.” *Solar Energy* 185 (April): 494–507. https://doi.org/10.1016/j.solener.2019.04.077.

Siebers, D. L., and J. S. Kraabel. 1984. “Estimating Convective Energy Losses from Solar Central Receivers.” SAND-84-8717. Sandia National Labs., Livermore, CA (USA). https://doi.org/10.2172/6906848.

Singh, Dileep, Wenhua Yu, Weihuan Zhao, Taeil Kim, David M France, and Roger K Smith. 2018. “Development and Prototype Testing of MgCl 2 / Graphite Foam Latent Heat Thermal Energy Storage System.” *Solar Energy* 159 (August 2017): 270–82. https://doi.org/10.1016/j.solener.2017.10.084.

Turchi, Craig S, and Matthew Boyd. 2019. “CSP Systems Analysis - Final Project Report.” NREL/TP-5500-72856. Golden, CO: National Renewable Energy Laboratory. https://www.nrel.gov/docs/fy19osti/72856.pdf.

Van Geet, Otto, Ran Fu, Kelsey Horowitz, Parthiv Kurup, Sara MacAlpine, and Timothy J. Silverman. 2018. “Analyzing the Energy Performance, Wind Loading, and Costs of Photovoltaic Slat Modules on Commercial Rooftops.” NREL/TP--7A40-70681. Golden, CO: NREL. https://doi.org/10.2172/1421779.

Wagner, Michael J., Alexandra M. Newman, William T. Hamilton, and Robert J. Braun. 2017. “Optimized Dispatch in a First-Principles Concentrating Solar Power Production Model.” *Applied Energy* 203 (October): 959–71. https://doi.org/10.1016/j.apenergy.2017.06.072.

Yaokawa, Jun, Katsunari Oikawa, and Koichi Anzai. 2007. “Thermodynamic Assessment of the KCl – K2CO3 – NaCl – Na2CO3 System.” *Computer Coupling of Phase Diagrams and Thermochemistry* 31: 155–63. https://doi.org/10.1016/j.calphad.2007.01.004.